Applied Computational Electromagnetics Society Journal

Editor-in-Chief
Atef Z. Elsherbeni

February 2009
Vol. 24 No. 1
ISSN 1054-4887

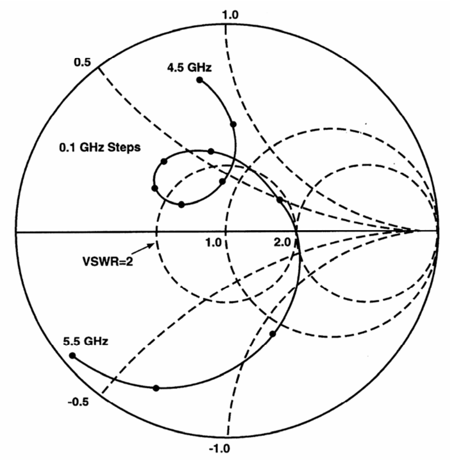

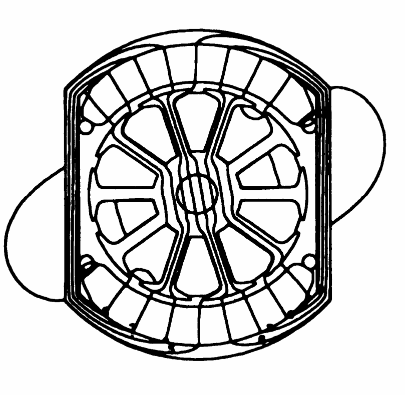

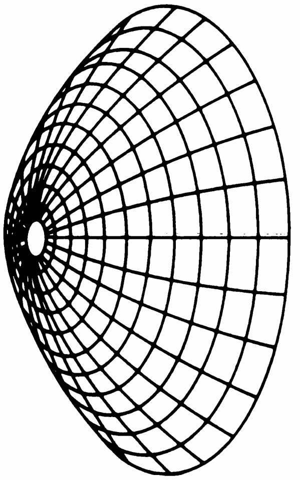

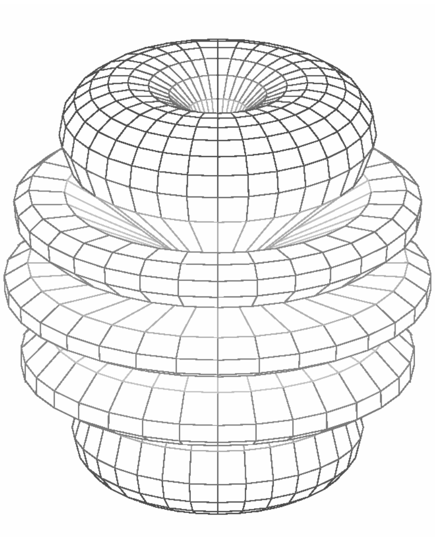

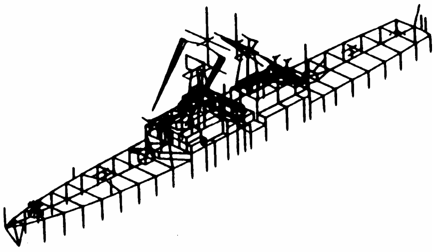

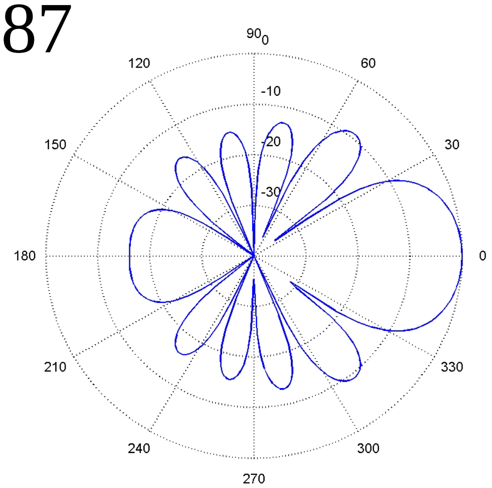

GENERAL PURPOSE AND SCOPE: The Applied Computational Electromagnetics Society ***(ACES)*** Journal hereinafter known as the ***ACES Journal*** is devoted to the exchange of information in computational electromagnetics, to the advancement of the state-of-the art, and the promotion of related technical activities. A primary objective of the information exchange is the elimination of the need to "re-invent the wheel" to solve a previously-solved computational problem in electrical engineering, physics, or related fields of study. The technical activities promoted by this publication include code validation, performance analysis, and input/output standardization; code or technique optimization and error minimization; innovations in solution technique or in data input/output; identification of new applications for electromagnetics modeling codes and techniques; integration of computational electromagnetics techniques with new computer architectures; and correlation of computational parameters with physical mechanisms.

SUBMISSIONS: The ***ACES Journal*** welcomes original, previously unpublished papers, relating to applied computational electromagnetics. Typical papers will represent the computational electromagnetics aspects of research in electrical engineering, physics, or related disciplines. However, papers which represent research in applied computational electromagnetics itself are equally acceptable.

Manuscripts are to be submitted through the upload system of ***ACES*** web site http://aces.ee.olemiss.edu See "Information for Authors" on inside of back cover and at ***ACES*** web site. For additional information contact the Editor-in-Chief:

Dr. Atef Elsherbeni
Department of Electrical Engineering
The University of Mississippi
University, MS 386377 USA
Phone: 662-915-5382 Fax: 662-915-7231
Email: atef@olemis.edu

SUBSCRIPTIONS: All members of the Applied Computational Electromagnetics Society who have paid their subscription fees are entitled to receive the ***ACES Journal*** with a minimum of three issues per calendar year and are entitled to download any published journal article available at http://aces.ee.olemiss.edu.

Back issues, when available, are $15 each. Subscriptions to ***ACES*** is through the web site. Orders for back issues of the ***ACES Journal*** and changes of addresses should be sent directly to ***ACES***:

Dr. Allen W. Glisson
302 Anderson Hall
Dept. of Electrical Engineering
Fax: 662-915-7231
Email: aglisson@olemiss.edu

Allow four week's advance notice for change of address. Claims for missing issues will not be honored because of insufficient notice or address change or loss in mail unless the Executive Officer is notified within 60 days for USA and Canadian subscribers or 90 days for subscribers in other countries, from the last day of the month of publication. For information regarding reprints of individual papers or other materials, see "Information for Authors".

LIABILITY. Neither ***ACES***, nor the ***ACES Journal*** editors, are responsible for any consequence of misinformation or claims, express or implied, in any published material in an ***ACES Journal*** issue. This also applies to advertising, for which only camera-ready copies are accepted. Authors are responsible for information contained in their papers. If any material submitted for publication includes material which has already been published elsewhere, it is the author's responsibility to obtain written permission to reproduce such material.

APPLIED COMPUTATIONAL ELECTROMAGNETICS SOCIETY JOURNAL

Editor-in-Chief
Atef Z. Elsherbeni

February 2009
Vol. 24 No. 1
ISSN 1054-4887

The ACES Journal is abstracted in INSPEC, in Engineering Index, DTIC, Science Citation Index Expanded, the Research Alert, and to Current Contents/Engineering, Computing & Technology.

The first, fourth, and sixth illustrations on the front cover have been obtained from the Department of Electrical Engineering at the University of Mississippi.

The third and fifth illustrations on the front cover have been obtained from Lawrence Livermore National Laboratory.

The second illustration on the front cover has been obtained from FLUX2D software, CEDRAT S.S. France, MAGSOFT Corporation, New York.

THE APPLIED COMPUTATIONAL ELECTROMAGNETICS SOCIETY
http//:aces.ee.olemiss.edu

ACES JOURNAL EDITOR-IN-CHIEF

ACES JOURNAL ASSOCIATE EDITORS-IN-CHIEF

ACES JOURNAL EDITORIAL ASSISTANTS

ACES JOURNAL EMERITUS EDITORS-IN-CHIEF

ACES JOURNAL EMERITUS ASSOCIATE EDITORS-IN-CHIEF

DECEMBER 2008 REVIEWERS

THE APPLIED COMPUTATIONAL ELECTROMAGNETICS SOCIETY

JOURNAL

Vol. 24 No. 1 February 2009

TABLE OF CONTENTS

A Review and Application of the Finite-Difference Time-Domain Algorithm Applied to the Schrödinger Equation

J. R. Nagel

University of Utah
Department of Electrical and Computer Engineering
Salt Lake City, Utah, USA
james.nagel@utah.edu

Abstract – This paper contains a review of the FDTD algorithm as applied to the time-dependent Schrödinger equation, and the basic update equations are derived in their standard form. A simple absorbing boundary condition is formulated and shown to be effective with narrowband wave functions. The stability criterion is derived from a simple, novel perspective and found to give better efficiency than earlier attempts. Finally, the idea of probability current is introduced for the first time and shown how it can be used to radiate new probability into a simulation domain. This removes the need to define an initial-valued wave function, and the concept is demonstrated by measuring the transmission coefficient through a potential barrier.

I. INTRODUCTION

Most electrical engineers are already familiar with the Finite-Difference Time-Domain (FDTD) algorithm as a popular tool for simulating the progression of time-dependent Maxwell equations. However, as the push for miniaturization brings us closer to the realm of nanoscale devices, Maxwell's equations can no longer be relied upon to provide useful insight. Nanoscale integrated circuits, quantum computers, and solid-state devices are just a few of the emerging electronic technologies that cannot be understood using classical electromagnetic theory. Instead, we must delve into the realm of quantum mechanics, where the laws of physics are more correctly governed by the Schrödinger equation. It will therefore be useful for electrical engineers to gain a deeper understanding of the Schrödinger equation, as well as develop a rigorous set of software tools for simulating the time-development of complex quantum systems. In particular, FDTD is a well-suited tool for this task, and can be easily modified for quantum simulation.

The first attempt to create a working FDTD algorithm for the Schrödinger equation was published by Goldberg et. al. in 1967 [1], but remained relatively obscure for many years. After 1990, the topic began to receive greater attention in the literature [2–4], most of which has been based on the Crank-Nicholson scheme. In 2004, Soriano et. al. rigorously formulated a more efficient FDTD algorithm and dubbed it ”FDTD-Q” in order to distinguish its application for quantum systems [5]. Meanwhile, quantum FDTD has already been used for many practical applications such as numerical simulation of quantum dots [6] and the time-progression of quantum logic gates [7].

Despite the recent activities surrounding FDTD-Q, the number of publications on the topic are a tiny fraction of what has been devoted to Maxwell's equations. Furthermore, many subtle nuances inherent to the Schrödinger equation tend to emerge when an FDTD-Q is applied. Thus, the goal of this paper is to review the basic FDTD-Q algorithm and to introduce new topics for future research. It is assumed that the reader is reasonably familiar with the Maxwellian FDTD, and so little time needs to be spent on the minor details and terminology. It is further assumed that the reader is at least familiar with basic quantum theory, though the more important expressions are reviewed in section II. For a more complete study of quantum mechanics, the reader is referred to [8] and [9].

The basic update equations of the FDTD-Q algorithm are derived in section III, and the information here is similar to what can be found in [5]. The issue of numerical stability is discussed in section IV, and the critical time step is derived from a unique, and hopefully more intuitive, perspective from that given by [10]. A Mur absorbing boundary condition is studied in section V, after which a simple example of quantum tunneling is simulated in section VI. Finally, we will introduce the novel concept of probability currents in section VII and show how they can be used to inject plane waves into a quantum simulation domain.

II. BACKGROUND

Just as Maxwell's equations are fundamental to all of electromagnetics, the Schrödinger equation is fundamental to all of quantum mechanics. The three-dimensional, time-dependent Schrödinger equation is therefore given as [8],

$$j\hbar\frac{\partial\psi(\mathbf{r},t)}{\partial t}=-\frac{\hbar^2}{2m}\nabla^2\psi(\mathbf{r},t)+V(\mathbf{r})\psi(\mathbf{r},t) \qquad (1)$$

where $\psi(\mathbf{r},t)$ is the wave function at position $\mathbf{r}$ and time t, $V(\mathbf{r})$ is the potential function, m is the particle mass, and $\hbar$ is the reduced Planck's constant. Although $\psi(\mathbf{r},t)$ is not a physically measurable quantity, it is necessary in order to compute the function $\rho(\mathbf{r},t)$ defined by,

$$\rho(\mathbf{r},t)=\psi^*(\mathbf{r},t)\psi(\mathbf{r},t)=|\psi(\mathbf{r},t)|^2\ . \qquad (2)$$

The interpretation of ρ is that of a time-varying probability density function (pdf) for the position of the particle. Thus, the total probability P of finding the particle in some volume V is found by integrating ρ over all points within that volume, [8]

$$P=\int_V \rho(\mathbf{r},t)d\mathbf{r}\ . \qquad (3)$$

Due to this probabilistic interpretation, the wave function must be normalized so that integration of ρ over all space produces a value of 1. It also serves to emphasize how the wave-particle duality of nature is really only an expression of how the positional pdf of a particle is governed by a wave-like equation.

The wavenumber amplitude $\phi(\mathbf{k})$ is defined by the Fourier transform of ψ at $t=0$. In three dimensions, this is given by, [8]

$$\phi(\mathbf{k})=\frac{1}{(2\pi)^{3/2}}\int_{-\infty}^{+\infty}\psi(\mathbf{r},0)e^{-j\mathbf{k}\cdot\mathbf{r}}d\mathbf{r} \qquad (4)$$

where $\mathbf{k}$ is the wave-vector. In particular, $\mathbf{k}$ is important because it tells us the particle's momentum, which is given by $\mathbf{p}=\hbar\mathbf{k}$. The function ϕ, like ψ, is not directly observable, but is only used to compute the pdf defined by $|\phi(\mathbf{k})|^2$. This quantity represents the probability density of detecting the wave-vector $\mathbf{k}$ after a given experiment. Thus, like before, the total probability P_k of detecting some wave-vector (or equivalently, some momentum) within the volume V_k (in k-space) is found by, [8]

$$P_k=\int_{V_k}|\phi(\mathbf{k})|^2\,d\mathbf{k}\ . \qquad (5)$$

From this interpretation, it is clear that the Heisenberg uncertainty principle is merely a result of the Fourier relationship between probabilities in position-space and momentum-space. In other words, any restriction of variance within one domain will inevitably increase variance within the other.

III. UPDATE EQUATIONS

This next section parallels the derivations found in [4, 5], but with more explicit detail and clarification. We begin by noting that complex-valued arithmetic can be numerically costly, so it is helpful to first break up the wave function into real and imaginary components such that,

$$\psi(\mathbf{r},t)=\psi_R(\mathbf{r},t)+j\ \psi_I(\mathbf{r},t)\ . \qquad (6)$$

This step allows us to treat each component separately and perform only real-valued computations with each function. Plugging the real and imaginary components back into the Schrödinger equation thus produces two coupled partial differential equations of the form,

$$\begin{aligned}\hbar\frac{\partial\psi_R(\mathbf{r},t)}{\partial t} &= -\frac{\hbar^2}{2m}\nabla^2\psi_I(\mathbf{r},t)+V(\mathbf{r})\psi_I(\mathbf{r},t) &(7)\\ \hbar\frac{\partial\psi_I(\mathbf{r},t)}{\partial t} &= +\frac{\hbar^2}{2m}\nabla^2\psi_R(\mathbf{r},t)-V(\mathbf{r})\psi_R(\mathbf{r},t) &(8)\end{aligned}$$

The next step is to define a mesh that discretely samples grid points in space and time. Using the standard FDTD notation for grid spacings of Δx, Δy, Δz, and time spacings of Δt, this gives,

$$\begin{aligned}x_i &= i\Delta x &(9)\\ y_j &= j\Delta y\ , &(10)\\ z_k &= k\Delta z\ , &(11)\\ t_n &= n\Delta t\ . &(12)\end{aligned}$$

Note that in this context, j is not to be confused with the imaginary unit $\sqrt{-1}$ as implied by equation (1), nor is k to be confused with the particle wavenumber. We next define a short-hand notation for the wave function evaluated at the mesh points. This is given by,

$$\begin{aligned}\psi_R(x_i,y_j,z_k,t_n) &= \psi_R^n(i,j,k) &(13)\\ \psi_I(x_i,y_j,z_k,t_n) &= \psi_I^n(i,j,k)\ . &(14)\end{aligned}$$

With the wave function sampled on a discrete grid, the derivatives will now be approximated by using finite-differences. For convenience, it helps to define the imaginary part of the wave function to exist at half-step time intervals from the real part. This is analogous to the way E-fields and H-fields are placed at half-step intervals in conventional FDTD because it facilitates the use of the central-difference method for the time derivatives. Thus, the time derivatives on the real- and imaginary-valued wave functions are approximated by,

$$\frac{\partial}{\partial t}\psi_R^{n+1/2}(i,j,k)\approx\frac{\psi_R^{n+1}(i,j,k)-\psi_R^n(i,j,k)}{\Delta t} \qquad (15)$$

$$\frac{\partial}{\partial t}\psi_I^{n}(i,j,k)\approx\frac{\psi_I^{n+1/2}(i,j,k)-\psi_I^{n-1/2}(i,j,k)}{\Delta t}\ . \qquad (16)$$

Similarly, we apply a central-difference on the spatial derivative to obtain the well-known approximation to the second-partial, given by,

$$\frac{\partial^2}{\partial x^2}\psi_R^n(i,j,k)\approx \frac{\psi_R^n(i+1,j,k)-2\psi_R^n(i,j,k)+\psi_R^n(i-1,j,k)}{\Delta x^2} \qquad (17)$$

with a similar expression for all other spatial derivatives. Plugging these approximations back into equations (7) and (8) and solving for the update equations then gives the formulation as given by [5], which is,

$$\begin{aligned}\psi_R^{n+1}(i,j,k) \;&=\; \psi_R^{n}(i,j,k)\\ &-\, c_x\Big[\psi_I^{n+1/2}(i+1,j,k) - 2\,\psi_I^{n+1/2}(i,j,k)\\ &\qquad +\; \psi_I^{n+1/2}(i-1,j,k)\Big]\\ &-\, c_y\Big[\psi_I^{n+1/2}(i,j+1,k) - 2\,\psi_I^{n+1/2}(i,j,k)\\ &\qquad +\; \psi_I^{n+1/2}(i,j-1,k)\Big]\\ &-\, c_z\Big[\psi_I^{n+1/2}(i,j,k+1) - 2\,\psi_I^{n+1/2}(i,j,k)\\ &\qquad +\; \psi_I^{n+1/2}(i,j,k-1)\Big]\\ &+\, c_v V(i,j,k)\psi_I^{n+1/2}(i,j,k)\end{aligned} \tag{18}$$

for the real part, and

$$\begin{aligned}\psi_I^{n+1/2}(i,j,k) &= \psi_I^{n-1/2}(i,j,k)\\ &+\; c_x\left[\psi_R^{n}(i+1,j,k) - 2\psi_R^{n}(i,j,k) + \psi_R^{n}(i-1,j,k)\right]\\ &+\; c_y\left[\psi_R^{n}(i,j+1,k) - 2\psi_R^{n}(i,j,k) + \psi_R^{n}(i,j-1,k)\right]\\ &+\; c_z\left[\psi_R^{n}(i,j,k+1) - 2\psi_R^{n}(i,j,k) + \psi_R^{n}(i,j,k-1)\right]\\ &-\; c_v\; V(i,j,k)\psi_R^{n}(i,j,k)\;,\end{aligned} \tag{19}$$

for the imaginary part. The constant coefficients are given by,

$$c_x \;=\; \frac{\hbar\Delta t}{2m\Delta x^2} \tag{20}$$

$$c_y \;=\; \frac{\hbar\Delta t}{2m\Delta y^2}\;, \tag{21}$$

$$c_z \;=\; \frac{\hbar\Delta t}{2m\Delta z^2}\;, \tag{22}$$

$$c_v \;=\; \frac{\Delta t}{\hbar}\;. \tag{23}$$

From this point on, FDTD-Q is performed exactly the same as the Maxwellian FDTD. That is, an iterative loop solves for the state of the system at incremental time steps and "leap-frogs" between the real and imaginary components. Between each increment, the appropriate boundary conditions are applied.

It is interesting to compare the similarities between the Schrödinger and Maxwellian FDTD algorithms. For example, the real and imaginary wave functions are somewhat analogous to the electric and magnetic fields in the way they couple together in space and time. However, because of the second-order spatial derivatives, the real and imaginary wave functions can both exist at the same spatial grid point. Compare this with the Maxwellian FDTD, where the first-order derivatives require the electric and magnetic field stencils to be defined at half-step increments from each other in both space and time.

IV. STABILITY

The critical time step for stable FDTD-Q simulation was first derived by Soriano et. al. in 2004 by using an argument based on the "growth factor" of the wave function eigenvalues [5]. In 2005, Dai et. al. re-derived the stability criterion from the perspective of accumulated numerical error, and arrived at a similar, but more correct, solution [10]. This next section offers a third derivation that simply preserves the natural bounds of the wave function, and provides a more complete result than either [5] or [10]. For simplicity, the derivation is limited to one dimension and then briefly extended to three.

Suppose the potential function is a constant value such that $V(x) = V_0$. Solutions to the Schrödinger equation then take on the form of free particles with wave functions given by,

$$\psi(x,t) = \alpha_1 e^{j(kx-\omega t)} + \alpha_2 e^{j(kx+\omega t)} \tag{24}$$

where k is the particle wavenumber and ω is the angular frequency. Without any loss of generality, consider the simple case of a free particle traveling to the right where $\alpha_1 = 1$ and $\alpha_2 = 0$. The real and imaginary components are then simply,

$$\psi_R(x,t) \;=\; \cos(kx-\omega t) \tag{25}$$

$$\psi_I(x,t) \;=\; \sin(kx-\omega t)\;. \tag{26}$$

In terms of the FDTD stencil, these can be written as,

$$\psi_R^n(i) \;=\; \cos(ki\Delta x - \omega n\Delta t)\;, \tag{27}$$

$$\psi_I^n(i) \;=\; \sin(ki\Delta x - \omega n\Delta t)\;. \tag{28}$$

For convenience, let us now define $A = ki\Delta x - \omega n\Delta t$ so that,

$$\psi_R^n(i) \;=\; \cos(A) \tag{29}$$

$$\psi_I^n(i) \;=\; \sin(A)\;. \tag{30}$$

Furthermore, define the constants $B = k\Delta x$ and $C = \omega\Delta t$ so that,

$$\psi_R^{n+1}(i) \;=\; \cos(A-C) \tag{31}$$

$$\psi_I^{n+1/2}(i) \;=\; \sin(A-C/2)\;, \tag{32}$$

$$\psi_I^{n+1/2}(i+1) \;=\; \sin(A+B-C/2)\;, \tag{33}$$

$$\psi_I^{n+1/2}(i-1) \;=\; \sin(A-B-C/2)\;. \tag{34}$$

Next, substitute equations (29) to (34) back into equation (18) to find,

$$\begin{aligned}\cos(A-C) = -\,c_x\,[\,&\sin(A+B-C/2)\\ &-2\sin(A-C/2)\\ &+\sin(A-B-C/2)]\\ &+c_v V_0\sin(A-C/2)+\cos(A)\;.\end{aligned} \tag{35}$$

The importance of equation (35) is that it places constraints on the available choices for c_x and c_v. If these constants are not properly defined, then equation (35) can not be satisfied with real values for A, B, or C. As a result, numerical error quickly accumulates and the wave function increases without bound.

In order to maintain a stable simulation, it is necessary to choose the constants c_x and c_v such that equation (35) is satisfied by only real values of A, B, and C. The simplest way to do this is by choosing a time step Δt that prevents the right-hand side from ever exceeding the natural bounds of the left-hand side. In other words, we must enforce the condition that,

$$-1 \leq \cos(A - C) \leq 1 \; . \tag{36}$$

After applying this restriction to the right-hand side of equation (35), we find that c_x and c_v are limited by the extreme values of their multiplicative factors. For the positive bound of equation (36), this leads us to the expression,

$$4c_x + c_v V_0 \leq 2 \tag{37}$$

or equivalently

$$\frac{2\hbar\Delta t}{m\Delta x^2} + \frac{\Delta t V_0}{\hbar} \leq 2 \; . \tag{38}$$

Finally, solve for Δt to find,

$$\Delta t \leq \frac{\hbar}{\frac{\hbar^2}{m\Delta x^2} + \frac{V_0}{2}} \; . \tag{39}$$

The upper bound on Δt is called the *critical time step*, Δt_c, and represents the maximum allowable time increment that will maintain a stable simulation [5]. It is also the same result that is found by exploring the lower bound of equation (36) instead of the upper.

In the event that $V(x)$ is not a constant value, then equation (39) is still true for sectionally constant potentials, even if those potentials are only one grid point in size. As a result, every point in the domain essentially has its own limit for Δt, and a stable simulation is guaranteed only by ensuring that equation (39) is satisfied over all points within the simulation. Thus, the maximum allowable time step over a varying potential region $V(x)$ is found by,

$$\Delta t_c = \arg\min_x \left[\frac{\hbar}{\frac{\hbar^2}{m\Delta x^2} + \frac{V(x)}{2}} \right] \; . \tag{40}$$

If one follows the above derivation in three dimensions, it is straightforward to show that equation (37) will be rewritten into,

$$4(c_x + c_y + c_z) + c_v V(\mathbf{r}) \leq 2 \tag{41}$$

solving for the critical time step therefore yields,

$$\Delta t = \arg\min_{\mathbf{r}} \left[\frac{\hbar}{\frac{\hbar^2}{m}\left(\frac{1}{\Delta x^2} + \frac{1}{\Delta y^2} + \frac{1}{\Delta z^2}\right) + \frac{V(\mathbf{r})}{2}} \right] \; . \tag{42}$$

For comparison, the expression in equation (42) is nearly identical to that given by [5], except there is now a factor of $1/2$ which divides V in the denominator. This can make a significant difference for simulations where V is large in comparison to $\hbar^2/m\Delta x^2$.

The result in equation (42) is also similar to that given by Dai et. al. in [10], except for two key differences. First is the argument that the inequality of equation (42) should be limited to a less-than relation ($<$), and that inclusion of the upper bound does not necessarily guarantee stability. Fortunately, numerical truncation within a computer's memory will always set Δt to some value slightly smaller than its exact mathematical assignment. As a result, there is little practical difference in distinguishing between the ($<$) and ($\leq$) relations.

The second key difference in [10] is a replacement of $V(\mathbf{r})$ with $|V(\mathbf{r})|$, that is, all potentials are treated as positive values. For the case of a positive-definite V, this makes no difference and the two formulations are equivalent. However, for the case of negative potentials, Δt_c actually gets larger, and therefore does not influence the minimum time step over a simulation domain. So even though the formulation in [10] is certainly guaranteed to be stable, it does not necessarily provide one with the maximum stable value.

Interestingly, the critical time step seems to approach infinity as $V/2 \to -\hbar^2/m\Delta x^2$ and stable simulation is easily demonstrated for relatively large values of Δt_c. Indeed, it may even be possible to exploit this effect for faster quantum simulations. It remains unclear, however, what sort of trade-offs one incurs by pushing the limits of very large time steps in a domain of all-negative potentials. Experiments also demonstrate that for $V < -\hbar^2/m\Delta x^2$, the expression in equation (42) no longer provides stability, while the formulation in [10] still remains valid. Such behavior has yet to be fully analyzed, and a general expression for the maximum stable time step over all possible V remains unknown.

V. ABSORBING BOUNDARY CONDITIONS (ABCS)

Because of the nonlinear dispersion relation that arises from the Schrödinger equation, absorbing boundary conditions (ABCs) can be difficult to implement. The problem was first addressed by Shibata in 1991 [2], and then expanded upon by Kuska in 1992 [3]. Both solutions worked by devising a linear approximation to the dispersion relation and then formulating a corresponding partial differential equation to enforce at the boundaries. The problem was further addressed and formalized by Arnold et. al. [11], and has even been expanded by others to include the nonlinear Schrödinger equation [12]. To date, however, all of these formulations have been based on the Crank-Nicholson discritization, and none have been demonstrated in the FDTD-Q formulation of equations

(18) and (19). Therefore, this next section will introduce a simple ABC that is compatible with FDTD-Q.

The simplest ABC is the first-order Mur condition, which enforces a one-way wave equation at the boundaries. For a plane-wave traveling to the right in one dimension, this is given by, [13]

$$\frac{\partial}{\partial x}\psi(x,t) = -\frac{1}{v_p}\frac{\partial}{\partial t}\psi(x,t) \tag{43}$$

where v_p is the phase velocity of the wave impinging at the boundary. As an example, we will consider the right-most boundary where $i = L$, though the end result is perfectly analogous at all other boundaries.

Solving for the update equations at the far-right grid point gives the familiar formulation, [13]

$$\psi_R^{n+1}(L) = \psi_R^n(L-1) + r\left[\psi_R^{n+1}(L-1) - \psi_R^n(L)\right] \tag{44}$$

for the real part, and,

$$\begin{aligned}\psi_I^{n+1/2}(L) = \psi_I^{n-1/2}&(L-1)\\ &+ r\left[\psi_I^{n+1/2}(L-1) - \psi_I^{n-1/2}(L)\right]\end{aligned} \tag{45}$$

for the imaginary part, with the constant r given by,

$$r = \frac{v_p\Delta t - \Delta x}{v_p\Delta t + \Delta x}\ . \tag{46}$$

By definition, the phase velocity is $v_p = \omega/k$, where ω is the angular frequency of the wave. The dispersion relation between ω and k is given by [2]

$$\hbar k = \sqrt{2m(\hbar\omega - V)}\ . \tag{47}$$

Next, we note that the expression $\hbar\omega$ represents the total energy $E = K + V$ of the particle. Back substitution therefore yields,

$$v_p = \frac{\hbar\omega}{\sqrt{2m(\hbar\omega - V)}} = \frac{K+V}{\sqrt{2mK}}\ . \tag{48}$$

It is worthwhile to note how equations (44) and (45) are very similar to the classical Mur boundary of Maxwell's equations. The main difference, however, is that both ψ_R and ψ_I exist at the same grid point, while E and H typically are defined at half-step increments. As a result, the classical Mur ABC is only applied to the field that exists at the boundary, which is either E or H, but never both. Since both ψ_R and ψ_I exist at the boundary, the ABC must be applied to both quantities after each iteration of FDTD-Q.

Although the Mur ABC is relatively simple to implement, it suffers from several major trade-offs. The first is that performance diminishes with steep angles of incidence, which is a well-known limitation from classical FDTD. For simple simulations in one-dimension, this is generally not a concern since all waves impinge perpendicularly to the boundaries. In two or three dimensions, however, the problem is much more significant.

A second problem arises from the fact that phase velocity v_p of a quantum wave packet varies with ω. As a result, equations (44) and (45) exhibit a band-limited response. This requires the user to manually "tune" the Mur boundary around some given center frequency. It also means that wideband wave packets will exhibit significantly greater reflection than narrowband packets. For the case where $V > 0$, a local minimum actually appears in v_p at $K = V$, and the Mur ABC performs best around this value. However, for regions where the slope of v_p is very large, the ABC performance diminishes accordingly.

Despite its complex behavior, the simple Mur ABC can still perform reasonably well under practical conditions. To demonstrate, we generated a Gaussian wave packet with a mean kinetic energy of $K_0 = 500$ eV and a standard deviation of 2.0 Å. The packet was placed in a domain of $V = 0$ potential and directed against a tunable boundary centered at the variable energy K. Figure 1 shows a demonstration of this. If we neglect the slight spectral variance that comes from using a Gaussian envelope, the total remaining probability after the packet collides with the boundary is a fair measure of the reflection coefficient. As demonstrated in Fig. 2, a properly tuned boundary still provides as much as 35 dB of return loss on a Gaussian wave packet.

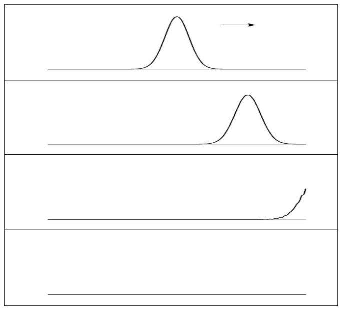

Fig. 1. Four snapshots of a Gaussian wave packet as it is absorbed by the simple Mur boundary. The mean particle energy is 500 eV and the boundary is "tuned" to the same value.

Finally, a word of warning must be noted for boundaries where $V < 0$. Under the condition $K < |V|$, ω takes on a negative value, thereby forcing v_p to be negative as well. This means the Mur ABC actually requires waves to *enter* the simulation from the boundaries instead of *leave*. As a result, numerical error quickly accumulates and destabilizes the simulation.

VI. EXAMPLE: QUANTUM TUNNELING

One of the more interesting predictions of quantum mechanics is that a particle can penetrate through a potential barrier of greater height than the particle's kinetic energy. This phenomenon, called *tunneling*, is easily

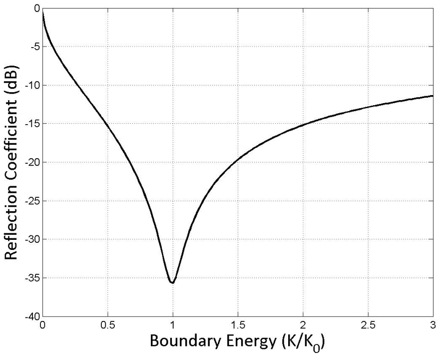

Fig. 2. Reflection coefficient of a one-dimensional Gaussian wave packet with mean kinetic energy K_0 as it reflects from a Mur absorbing boundary tuned for K.

demonstrated by FDTD-Q. It is not difficult to imagine how this could become a serious issue in the realm of modern micro-electronics. For example, the potential barrier separating the gate and source of a transistor is just such a system. If the leakage current were significantly affected by tunneling electrons, then quantum mechanics would be the only means of understanding the problem.

To begin, we define an initial value for the wave packet to represent a free particle traveling to the right, and then localize it in space by multiplying with a Gaussian envelope. For a potential barrier of thickness $2a$, the potential function is simply defined as $V(x) = V_0$, where $-a \leq x \leq a$ and V_0 is some potential energy greater than K.

Figure 3 shows a simulated demonstration of just such a system. A particle with kinetic energy of $K = 500$ eV is sent towards a potential barrier with $V_0 = 600$ eV. The grid step size is fixed at $dx = 0.005$ Å, and the barrier thickness is set to $2a = 0.25$ Å, or 50 grid points. The simulation domain consists of 3000 grid points. The figure shows four snapshots of the simulation as it progresses in time. As the particle collides with the potential barrier, some of the wave function is able to penetrate through while the rest is reflected. In the end, there is a finite probability for the particle to be found on the right side of the barrier, even though the barrier is greater than the kinetic energy of the particle.

A useful metric for characterizing a system such as this is the transmission coefficient T, which is defined as the probability that an incident particle will tunnel through the barrier. This is calculated by integrating ρ along all points to the right of the boundary and then dividing by the total probability of the system,

$$T = \frac{\int_a^\infty \rho(x)dx}{\int_{-\infty}^\infty \rho(x)dx} \ . \tag{49}$$

Note that if the wave packet is properly normalized, the denominator is identically 1. The result of this computation is a value of $T = 0.1701$, which is only 1.5% of error from its theoretical value of 0.1676 (see equation (6.14) in [8]).

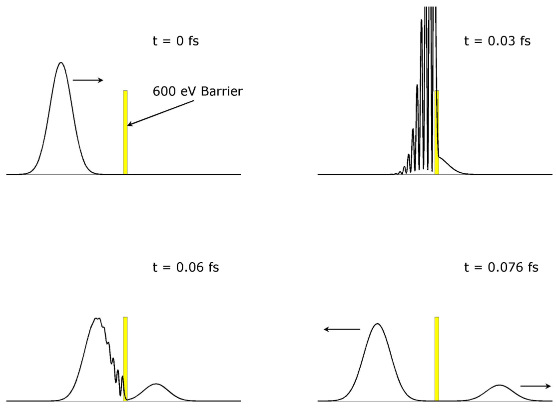

Fig. 3. Snapshots of a wave packet ρ as it collides with a potential barrier. The particle has a kinetic energy of 500 eV and the potential barrier is 600 eV. The thickness of the barrier is only 0.25 Å (50 grid points), so some of the probability penetrates to the other side.

VII. PROBABILITY CURRENT SOURCES

A useful area of research that has yet to be explored is the idea of probability sources. To date, simulations involving FDTD-Q have always required an initial-valued wave function to be pre-inserted into the domain at $t = 0$. If one is willing to forgo conservation and normalization of probability, then it is possible to inject probability into a simulation domain via probability "currents." Physically, the situation is analogous to the way electric currents radiate new electric fields. The benefit of such currents would be the potential to generate a true plane wave of probability, and would greatly facilitate the measurement of scattering parameters with complex potentials.

Mathematically, the injection of probability into a simulation domain can be achieved by simply introducing a source term into the Schrödinger equation. This is analogous to the use of "soft" current sources in the classical Maxwellian FDTD. Thus, if we define the complex-valued injection current $J(\mathbf{r}, t) = J_R(\mathbf{r}, t) + jJ_I(\mathbf{r}, t)$ to represent a source of new probability, then equation (1) can be modified as,

$$j\hbar \frac{\partial \psi(\mathbf{r}, t)}{\partial t} = -\frac{\hbar^2}{2m}\nabla^2\psi(\mathbf{r}, t) + V(\mathbf{r})\psi(\mathbf{r}, t) + J(\mathbf{r}, t) \ . \tag{50}$$

After following the derivation through to the update equations, the only difference will be the addition of source terms onto the ends of equations (18) and (19), or more specifically,

$$\psi_R^{n+1}(i,j,k) = \ ... \ + \ c_v J_I^{n+1/2}(i,j,k) \tag{51}$$

$$\psi_I^{n+1/2}(i,j,k) = \ ... \ - \ c_v J_R^{n}(i,j,k) \ . \tag{52}$$

Figure 4 demonstrates the injection principle by simulating a real-valued, sinusoidal current at the center of an empty domain. As can be seen, what begins as an empty region of space quickly fills with probability as the wave function propagates away from the source. Because of the high-frequency content that is inherent to any transient function, ρ exhibits some natural amount of ringing after the current is suddenly introduced, and significant ripples tend to remain even long after the transients have settled down. To lessen this effect, the current source was padded with an exponential rise time, which also reduces the amount reflection at the band-limited ABCs.

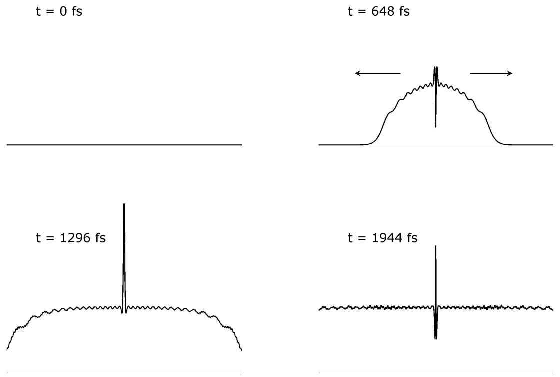

Fig. 4. Snapshots of ρ as it propagates away from the current source located in the center.

A very useful application of probability currents can be seen in Fig. 5, which demonstrates the same 600 eV barrier as that in Fig. 3. This time, instead of pre-inserting a Gaussian wave packet, a current source of the same wavenumber was inserted next to the barrier. The result is a genuine plane-wave of probability that impinges on the boundary and tunnels through. Also note the fringe pattern between the current source and the barrier. This is simply the result of interference between the forward wave and the reflected wave, and is analogous to the standing wave that develops on a transmission line with a mismatched load. The reflected wave then passes harmlessly through the current source and gets absorbed by the left boundary. The transmitted wave is likewise absorbed by the right boundary, and the steady-state result is a relatively smooth, constant amplitude to the right of the barrier.

The transmission coefficient of this system is found by first computing the average probability amplitude to the right of the boundary, and then dividing by the average amplitude that occurs in the absence of the barrier,

$$T = \frac{\int_a^\infty \rho(x)dx\ |_{barrier}}{\int_a^\infty \rho(x)dx\ |_{space}} . \tag{53}$$

Using this method, the computed value is $T = 0.160$, which is still only 4.8% error. The main benefit to this method, however, is that the full Gaussian packet does not need to be initialized into the grid, thereby reducing the necessary size of the simulation domain. Even when calculated on a domain of one-fifth the size (600 points), the result does not change by more than 0.1 %. Figure 6 shows the relative performance of this method against the analytical values for a varying barrier width. For a domain size of only 600 points, the mean error over the entire test range is only 3.43 %.

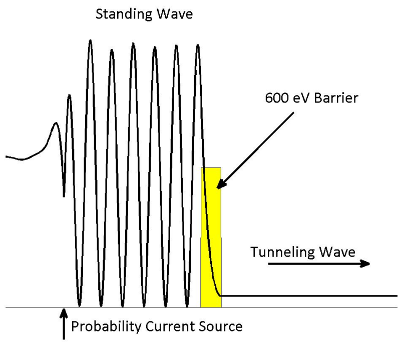

Fig. 5. A plane wave radiates away from the probability source at the left of the barrier. The wave collides with the potential barrier and partially transmits through. The rest of the wave reflects back towards the source and interferes with the forward-traveling wave, causing the fringes.

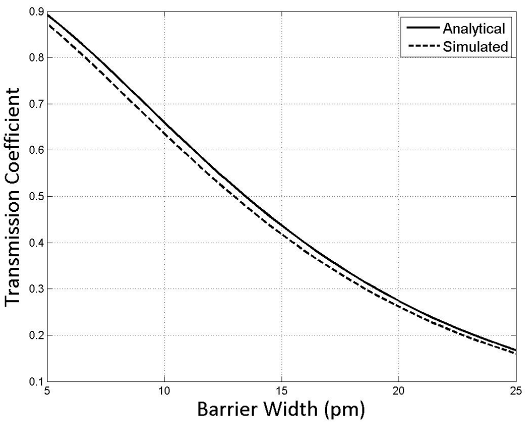

Fig. 6. Comparison of transmission coefficients for a potential barrier of varying size. Using the probability current source method, the mean error is 3.43 %.

VIII. CONCLUSIONS

This paper contains a review of FDTD-Q as applied to the time-dependent Schrödinger equation. The basic update equations have been derived in their standard form as presented in [5]. The stability criterion was rederived from a novel perspective and found to give larger stable time steps than that given by [10]. A simple absorbing boundary condition was also formulated and shown to be effective with narrowband wave functions. Finally, the idea of probability currents was introduced for the first time and shown how it can be used to inject probability into a simulation domain.

Most of the topic of FDTD-Q is still relatively unexplored, and many interesting avenues have yet to be researched. For example, broadband absorbing boundaries have certainly been rigorously applied to various quantum simulations [2, 3, 12, 14], but none have yet to be tailored specifically to FDTD-Q in its above formulation. The idea of probability currents is also an entirely new concept, and there is still a great deal of exploration left to be done. In particular, probability currents can be used to create genuine plane waves of probability, thereby removing the need for pre-initialized wave packets in the simulation. One can also imagine other uses for current sources, such as quantum beamforming or bistatic scattering, but these topics have yet to be researched.

ACKNOWLEDGMENTS

Special thanks to Dr. Cynthia Furse for her assistance with this research and with writing this paper.

REFERENCES

[1] A. Goldberg, H. M. Schey, and J. L. Schwartz, "Computer-generated motion pictures of one-dimensional quantum mechanical transmission and reflection phenomena," *American Journal of Physics*, vol. 35, no. 3, pp. 177–186, March 1967.

[2] T. Shibata, "Absorbing boundary conditions for the finite-difference time-domain calculation of the one-dimensional Schrödinger equation," *Physical Review B*, vol. 42, no. 8, pp. 6760–6763, March 1991.

[3] J. P. Kuska, "Absorbing boundary conditions for the Schrödinger equation on finite intervals," *Physical Review B*, vol. 46, no. 8, pp. 5000 – 5003, August 1992.

[4] D. M. Sullivan, *Electromagnetic Simulation Using the FDTD Method*. New York, NY: IEEE Press, 2000.

[5] A. Soriano, E. A. Navarro, J. A. Porti, and V. Such, "Analysis of the finite difference time domain technique to solve the Schrödinger equation for quantum devices," *Journal of Applied Physics*, vol. 95, no. 12, pp. 8011 – 8018, June 2004.

[6] D. M. Sullivan and D. S. Citrin, "Determination of the eigenfunctions of arbitrary nanostructures using time-domain simulation," *Journal of Applied Physics*, vol. 91, no. 5, pp. 3219–3226, March 2002.

[7] ——, "Time-domain simulation of a universal quantum gate," *Journal of Applied Physics*, vol. 96, no. 3, pp. 1540–1546, August 2004.

[8] E. Merzbacher, *Quantum Mechanics*, 3rd ed. New York, NY: John Wiley & Sons, 1998.

[9] P. A. Tipler and R. A. Llewellyn, *Modern Physics*, 3rd ed. New York, NY: W. H. Freeman and Company, 1999.

[10] W. Dai, G. Li, R. Nassar, and S. Su, "On the stability of the FDTD method for solving a time-dependent Schrödinger equation," *Numerical Methods in Partial Differential Equations*, vol. 21, no. 6, pp. 1140–1154, April 2005.

[11] A. Arnold, M. Ehrhardt, and I. Sofronov, "Discrete transparent boundary conditions for the Schrödinger equation: Fast calculation, approximation, and stability," *Communications in Mathematical Science*, vol. 1, no. 3, pp. 501–556, 2003.

[12] Z. Xu and H. Han, "Absorbing boundary conditions for nonlinear Schrödinger equations," *Physical Review E*, vol. 74, no. 3, pp. 037 704–(1–4), March 2006.

[13] G. Mur, "Absorbing boundary conditions for the finite-difference approximation of the time-domain electromagnetic-field equations," *IEEE Transactions on Electromagnetic Compatibility*, vol. 23, no. 4, pp. 337–382, November 1981.

[14] C. Farrell and U. Leonhardt, "The perfectly matched layer in numerical simulations of nonlinear and matter waves," *Journal of Optics B: Quantum and Semiclassical Optics*, vol. 7, no. 1, pp. 1–4, January 2005.

James Nagel reveived his B.S. (04) and M.S. (06) degrees in electrical engineering from Brigham Young University in Provo, Utah. He is currently working towards a Ph.D. in electrical engineering from the University of Utah in Salt Lake City, Utah. His specialties include electromagnetics, signal processing, array theory, and FDTD simulation. He is currently conducting research in MIMO communication systems, and teaches Applied Electromagnetics.

Wide-Angle Absorbing Boundary Conditions for Low and High-Order FDTD Algorithms

Mohammed F. Hadi

Electrical Engineering Dept., Kuwait University, P. O. Box 5969, Safat 13060, Kuwait

Abstract – Wide-angle performance of the perfectly-matched-layer absorbing boundary conditions for the finite-difference time-domain (FDTD) method is investigated for efficient modeling of electrically large structures. The original split-field, uniaxial and convolutional perfectly-matched-layer formulations are all optimized to produce near-flat absorption for incidence angles up to 87 degrees. Optimized wide-angle parameters are derived for both the standard FDTD method and a high-order finite-volumes-based variant. The investigated high-order algorithm in particular is shown to produce improved wide-angle performance over standard FDTD for all three perfectly-matched-layer variants even when they are optimized for normal wave incidence. In all cases, optimization is managed through appropriate choices of modeling parameters which can be directly and unobtrusively applied to existing FDTD codes.

Keywords: FDTD methods, PML absorbing boundary conditions, high-order methods, electrically large structures.

I. INTRODUCTION

With the recently mounting interest in Giga-Hertz and Tera-Hertz communications systems and devices, modeling electrically large structures is fast becoming a pressing need for designers and installers of those systems. The finite-difference time-domain (FDTD) method, especially in its high-order forms [1–11], is capable of accurately and efficiently modeling such large structures provided that the various FDTD modeling tools are updated to match their high accuracy [12–14]. One of those tools is the ability to truncate unbounded spaces with efficient absorbing boundary conditions. The current state of the art in this area is Bérenger's perfectly-matched-layer (PML) which comes in several different implementations [15–20]. Modeling electrically large problems presents a real challenge in this regard due to the large interface areas between the modeled structure and its surrounding absorbing layers. Such extended interfaces cause appreciably large outgoing energies to impinge on absorbing layers at steep angles where PML absorbing abilities quickly diminish [21]. This problem is exacerbated with the relatively coarse FDTD grids allowed by the high-order algorithms and demanded by computational efficiency requirements when modeling electrically large structures.

Several works investigated approaches to optimize PML parameters for maximum wide-angle absorption [22–26]. Most of these works were concerned with achieving maximum absorption for the incidence angles range of $0 \le \theta \le 75^\circ$ (with $\theta = 0$ representing normal incidence). While this operating range is reasonably unrestrictive when designing PML for electrically small FDTD models, it is not sufficient for electrically large modeling purposes. The moderately large two-dimensional building model investigated in [2], for example, had to be increased in size three-fold to insure adherence to a 75° incidence angle limit on all outgoing waves impinging on the surrounding PML region. Clearly, extending the PML operating range to near grazing incidence angles is critical for efficient electrically large FDTD models. One effort that pushed PML wide-angle functionality beyond $\theta = 75^\circ$ is the work of Kantartzis, Yioultsis, Kosmanis and Tsiboukis [26] which introduced a non-diagonally anisotropic PML where all nine dielectric tensor's elements are nonzero. This approach demonstrated good wide-angle PML performance at the expense of some mathematical complexity and added computational overhead.

It will be demonstrated in this work that the three major PML variants– the original split-field PML [15], the uniaxial PML [17, 18] and the convolutional PML [19, 20]– are all capable of near-flat absorption response for the incidence angles range of $0 \le \theta \le 87^\circ$. This very useful extended range will be realized through optimization routines that utilize complete FDTD/PML codes as functional arguments and PML parameters as optimization variables. Furthermore, this wide-angle capability will be demonstrated for both the standard FDTD method and a recently-developed finite-volumes-based algorithm [11] as a representative of high-order FDTD methods. Most critically, this wide-angle functionality does not require changes to existing FDTD/PML codes or result in added computational overhead.

II. FDTD AND PML FORMULATIONS

The various simulations and optimization analysis in this work will be based on the following FDTD and PML implementations, with the E_x field update equations as representative samples.

A. *Split-Field PML Formulation*

For this original PML formulation, the $E_x = E_{xy} + E_{xz}$ update equation is given by [15],

$$\begin{aligned} E_{xy}|^{n+\frac{1}{2}} &= e^{-\sigma_y \Delta t/\epsilon}\, E_{xy}|^{n-\frac{1}{2}} + \\ & \quad \frac{1-e^{-\sigma_y \Delta t/\epsilon}}{\sigma_y}\, D_y H_z \qquad (1) \\ E_{xz}|^{n+\frac{1}{2}} &= e^{-\sigma_z \Delta t/\epsilon}\, E_{xz}|^{n-\frac{1}{2}} - \\ & \quad \frac{1-e^{-\sigma_z \Delta t/\epsilon}}{\sigma_z}\, D_z H_y, \qquad (2) \end{aligned}$$

where the PML loss profile is coded by Holland's exponential time-stepping formula [27]. For the standard FDTD method, the $D_y H_z$ and $D_z H_y$ difference operators refer to,

$$\begin{aligned} D_y H_z &= \frac{1}{h}\left[H_z|_{j+\frac{1}{2}} - H_z|_{j-\frac{1}{2}}\right] \qquad (3) \\ D_z H_y &= \frac{1}{h}\left[H_y|_{k+\frac{1}{2}} - H_y|_{k-\frac{1}{2}}\right], \qquad (4) \end{aligned}$$

where the non-staggered i, j, k and n spatial and temporal indices are omitted for cleaner notation. The spatial difference operators for the high-order algorithm are represented by [11],

$$\begin{aligned} D_y H_z = {} & \frac{K_a}{h}\left[H_z|_{j+\frac{1}{2}} - H_z|_{j-\frac{1}{2}}\right] + \qquad (5) \\ & \frac{K_b}{3h}\left[H_z|_{j+\frac{3}{2}} - H_z|_{j-\frac{3}{2}}\right] + \\ & \frac{K_c}{12h}\left[\begin{array}{r} H_z|_{i+1,j+\frac{3}{2}} + H_z|_{i-1,j+\frac{3}{2}} \\ +H_z|_{j+\frac{3}{2},k+1} + H_z|_{j+\frac{3}{2},k-1} \\ -H_z|_{i+1,j-\frac{3}{2}} - H_z|_{i-1,j-\frac{3}{2}} \\ -H_z|_{j-\frac{3}{2},k+1} - H_z|_{j-\frac{3}{2},k-1} \end{array}\right] + \\ & \frac{K_d}{12h}\left[\begin{array}{r} H_z|_{i+1,j+\frac{3}{2},k+1} + H_z|_{i-1,j+\frac{3}{2},k+1} \\ +H_z|_{i+1,j+\frac{3}{2},k-1} + H_z|_{i-1,j+\frac{3}{2},k-1} \\ -H_z|_{i+1,j-\frac{3}{2},k+1} - H_z|_{i-1,j-\frac{3}{2},k+1} \\ -H_z|_{i+1,j-\frac{3}{2},k-1} - H_z|_{i-1,j-\frac{3}{2},k-1} \end{array}\right] \end{aligned}$$

and

$$\begin{aligned} D_z H_y = {} & \frac{K_a}{h}\left[H_y|_{k+\frac{1}{2}} - H_y|_{k-\frac{1}{2}}\right] + \qquad (6) \\ & \frac{K_b}{3h}\left[H_y|_{k+\frac{3}{2}} - H_y|_{k-\frac{3}{2}}\right] + \\ & \frac{K_c}{12h}\left[\begin{array}{r} H_y|_{i+1,k+\frac{3}{2}} + H_y|_{i-1,k+\frac{3}{2}} \\ +H_y|_{j+1,k+\frac{3}{2}} + H_y|_{j-1,k+\frac{3}{2}} \\ -H_y|_{i+1,k-\frac{3}{2}} - H_y|_{i-1,k-\frac{3}{2}} \\ -H_y|_{j+1,k-\frac{3}{2}} - H_y|_{j-1,k-\frac{3}{2}} \end{array}\right] + \\ & \frac{K_d}{12h}\left[\begin{array}{r} H_y|_{i+1,j+1,k+\frac{3}{2}} + H_y|_{i-1,j+1,k+\frac{3}{2}} \\ +H_y|_{i+1,j-1,k+\frac{3}{2}} + H_y|_{i-1,j-1,k+\frac{3}{2}} \\ -H_y|_{i+1,j+1,k-\frac{3}{2}} - H_y|_{i-1,j+1,k-\frac{3}{2}} \\ -H_y|_{i+1,j-1,k-\frac{3}{2}} - H_y|_{i-1,j-1,k-\frac{3}{2}} \end{array}\right]. \end{aligned}$$

An explanation and derivation procedure for the K tuning parameters in the above equations, which play a key role in minimizing numerical dispersion errors, can be found in [11].

Due to the extended reach of the high-order update equations (up to $\pm 3h/2$ from the updated field node), special difference operators are required for the FDTD layers bordering the PML's perfect-electric-conductor backplanes [13]. For example, when the E_x node is adjacent to a planar conducting boundary normal to the x-axis, the difference operators (5) and (6) reduce to,

$$\begin{aligned} D_y H_z = {} & \frac{K_a^b}{h}\left[H_z|_{j+\frac{1}{2}} - H_z|_{j-\frac{1}{2}}\right] + \qquad (7) \\ & \frac{K_b^b}{3h}\left[H_z|_{j+\frac{3}{2}} - H_z|_{j-\frac{3}{2}}\right] + \\ & \frac{K_c^b}{6h}\left[\begin{array}{r} H_z|_{j+\frac{3}{2},k+1} + H_z|_{j+\frac{3}{2},k-1} \\ -H_z|_{j-\frac{3}{2},k+1} - H_z|_{j-\frac{3}{2},k-1} \end{array}\right] \end{aligned}$$

$$\begin{aligned} D_z H_y = {} & \frac{K_a^b}{h}\left[H_y|_{k+\frac{1}{2}} - H_y|_{k-\frac{1}{2}}\right] + \qquad (8) \\ & \frac{K_b^b}{3h}\left[H_y|_{k+\frac{3}{2}} - H_y|_{k-\frac{3}{2}}\right] + \\ & \frac{K_c^b}{6h}\left[\begin{array}{r} H_y|_{j+1,k+\frac{3}{2}} + H_y|_{j-1,k+\frac{3}{2}} \\ -H_y|_{j+1,k-\frac{3}{2}} - H_y|_{j-1,k-\frac{3}{2}} \end{array}\right]. \end{aligned}$$

Readers are referred to [13] for more difference operators adjustments that deal with other conductor proximity situations as well as explanation of the above K-parameters and their relations to those in equations (5) and (6). Interested readers in the two-dimensional version of this high-order algorithm [2] can find similar treatments in [12].

B. *Uniaxial and Convolutional PML Formulations*

For these PML variants, Roden and Gedney's update equations will be used [20],

$$E_x|^{n+\frac{1}{2}} = E_x|^{n-\frac{1}{2}} + \frac{\Delta t}{\epsilon}\left[\begin{array}{r} D_y H_z/\kappa_y + \psi_y \\ -D_z H_y/\kappa_z - \psi_z \end{array}\right] \qquad (9)$$

where the difference operators for both FDTD algorithms are the same ones given in equations (3) and (6), and,

$$\begin{aligned} \psi_y &= b_y \psi_y|^{n-1} + c_y D_y H_z \qquad (10) \\ \psi_z &= b_z \psi_z|^{n-1} + c_z D_z H_y, \qquad (11) \end{aligned}$$

with

$$\begin{aligned} b_y &= \exp\left[-\left(\frac{\sigma_y}{\epsilon \kappa_y} + \frac{a_y}{\epsilon}\right)\right] \qquad (12) \\ b_z &= \exp\left[-\left(\frac{\sigma_z}{\epsilon \kappa_z} + \frac{a_z}{\epsilon}\right)\right], \qquad (13) \\ c_y &= \frac{(b_y - 1)\sigma_y/\kappa_y}{\sigma_y + \kappa_y a_y}, \qquad (14) \\ c_z &= \frac{(b_z - 1)\sigma_z/\kappa_z}{\sigma_z + \kappa_z a_z}. \qquad (15) \end{aligned}$$

The above equations fully describe the convolutional PML formulation, whereas the special case uniaxial PML formulation is realized by setting $\kappa_{y,z} = 1$ and $a_{y,z} = 0$ [18].

C. *PML Loss Profiles*

The three PML parameters, σ, κ and a, will be coded with the polynomial profiles,

$$\begin{aligned} \sigma(\rho) &= \sigma_{\text{max}} \left(\frac{\rho}{d}\right)^{n_\sigma} && (16)\\ \kappa(\rho) &= 1 + (\kappa_{\text{max}} - 1)\left(\frac{\rho}{d}\right)^{n_\kappa}, && (17)\\ a(\rho) &= a_{\text{max}} \left(\frac{d-\rho}{d}\right)^{n_a}, && (18) \end{aligned}$$

where ρ is the incremental PML depth measured from its interface with the scatterer region and d is the PML thickness. PML optimization and performance will now be decided based on proper choices of three parameters (σ_{max}, n_σ and d) for the split-field and uniaxial PML and seven parameters (σ_{max}, n_σ, κ_{max}, n_κ, a_{max}, n_a and d) for the convolutional PML. For the following analysis, one deviation from the literature should be mentioned here. The $\kappa \geq 1$ constraint [20, 28] will be relaxed to $\kappa \geq 0$. This step will prove to be crucial for realizing optimum wide-angle convolutional PML profiles as will become obvious in Section IV.

III. PML OPTIMIZATION PROCEDURE

For each of the three PML variants, optimum profiles were determined using MATLAB's FMINSEARCH optimization routine. This routine was set up to minimize an error quantity (Ψ) which is the maximum difference of two E_z surface plots from two FDTD simulations; one incorporating the PML formulation under study while the other is a large reference three dimensional space with matching FDTD parameters. The test domain is a $50 \times 50 \times 51$-cell vacuum terminated by a 10-layer PML (see Fig. 1). An E_z hard point-source [15] is introduced at the center of the vacuum that is non-zero only for the duration $0 \leq \omega t \leq 2\pi$,

$$E_z = \frac{1}{32}\left[10 - 15\cos(\omega t) + 6\cos(2\omega t) - \cos(3\omega t)\right]. \tag{19}$$

The chosen first harmonic of this signal is 1 GHz and the uniform FDTD grid size in all three dimensions is set as $h = \lambda/20$ at this frequency. The time step is set as the maximum allowed by each algorithm's stability criterion. The simulation time is chosen to be long enough to allow appropriate interaction of the outgoing wave with the PML interface, inner layers and backplanes; 100 and 110 times steps for standard and high-order FDTD, respectively. For the standard FDTD simulations, for instance, Fig. 2 shows that the lead propagating peak reaches the PML interface at time step $n = 53$. It also reaches the backplane of the 10-layer PML at $n = 74$ and what is left of it re-enters the test domain at $n = 95$. Once each simulation is completed, E_z data are collected from the central xy-plane (observation plane in Fig. 1) and introduced to the optimization routine.

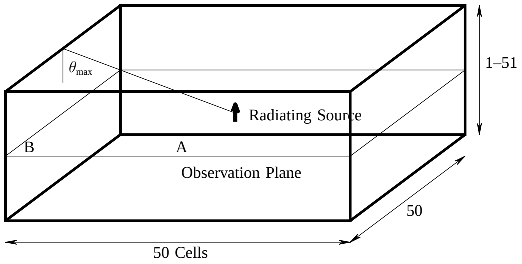

Fig. 1. PML test domain with the PML regions removed for clarity. Observed reflections are mainly due to side walls, except when the z-dimension approaches one cell where steep reflections off the top and bottom walls dominate. Radiating source and observation points A and B are located at (25,25), (25,0) and (0,0), respectively, within the observation plane.

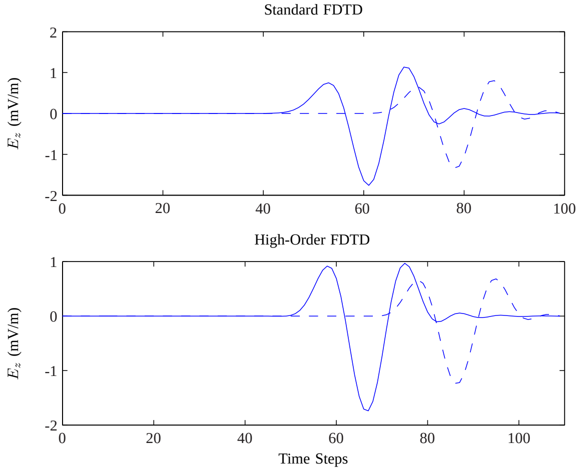

Fig. 2. Observed field values at locations A (solid) and B (dashed) which verify sufficient wave interaction with the PML layer for parameter optimization purposes.

Most PML reflection errors observed from the above experimental setup will be due to reflections corresponding to incidence angles $\theta \leq \theta_{\text{max}} = \pi/2$ within the observation plane. This θ_{max} value also holds for the normal plane as all six PML interfaces are equidistant from the centrally located point source. When the z-dimension of the test vacuum is collapsed, however, θ_{max} that corresponds to the top and bottom PML interfaces will start to increase beyond $\pi/4$, reaching 86.6° when the test vacuum is collapsed to $50 \times 50 \times 1$ FDTD cells. For the rest of this work, θ_{max} will refer to this increasing maximum incidence angle as the vaccuum's z-dimension is collapsed as illustrated in Fig. 1. This relatively rough experimental setup is deliberately chosen as it closely mimics real-world simulation challenges, especially when modeling electrically large structures.

In the following section, two sets of optimized PML parameters will be derived for each combination of FDTD algorithms and PML formulations; one set from a $50 \times 50 \times 51$-cell setup an another from a $50 \times 50 \times 1$-cell setup that highlights the near-grazing angle wave incidence challenge. To test each set of optimized PML parameters, it will be inserted back in the test setup and the error function defined earlier will be collected from a series of simulations where the z-dimension is collapsed incrementally, sweeping in the process the range $\pi/4 \leq \theta_{\text{max}} \leq 87°$.

IV. OPTIMIZATION RESULTS AND COMPARATIVE ANALYSIS

Table 1 summarizes the derived PML parameters from the optimization process detailed in the previous section for the standard and high-order FDTD algorithms. Listing the PML parameters in the table to 4–5 significant digits is necessary for optimum performance. For example, the -175 dB reflection error increased by 5 dB when the corresponding parameters were implemented with only two significant digits. Furthermore, experimenting with several sets of initial guesses was necessary to achieve minimal reflection error levels, especially with convolutional PML optimization runs.

Table 1. Optimized Split-field, Uniaxial and Convolutional PML profiles for conventional and wide - angle wave incidence on a 10-layer PML. (Units: S/m for σ and dB for error function Ψ)

		Standard FDTD		High-Order FDTD	
	θ_{max}	45°	87°	45°	87°
S	σ_{max}	0.6108	0.8051	0.8466	0.6469
	n_σ	3.9849	5.5968	3.6958	5.4837
	Ψ	-158	-116	-157	-119
U	σ_{max}	0.3532	0.4413	0.4526	0.4836
	n_σ	3.1769	3.9540	3.2428	4.1050
	Ψ	-152	-128	-151	-127
C	σ_{max}	0.3338	0.3226	0.5132	0.4288
	n_σ	4.1322	3.2352	3.3551	2.9732
	κ_{max}	0.3414	0.3207	0.4196	0.4699
	n_κ	3.8151	4.7704	2.8402	3.6169
	a_{max}	0	0.0980	0	0.0822
	n_a		1.0145		1.1934
	Ψ	-175	-148	-157	-147

A. Optimized PML Parameters at $\theta_{max} = \pi/4$

These parameters are most suitable for electrically small problems where the bulk of outgoing energy can be made to impinge on the surrounding PML regions within the limits of $\theta_{\text{max}} = \pi/4$ without incurring significant computational burden. We can deduce from tabel 1 that for standard FDTD, split-field PML performs slightly better than uniaxial PML (6 dB lower reflection) due to its more favorable σ_{max} and n_σ combination. Both however are vastly outperformed by convolutional PML with a 17 dB margin over split-field PML. The performance of the optimized parameters for the high-order FDTD algorithm mimicked those of standard FDTD for both split-field and uniaxial PML formulations. Convolutional PML, on the other hand, failed to match its excellent performance with standard FDTD and managed only to match split-field PML permanence which was the same for both FDTD algorithms. It should be noted here that for all cases in Table 1, the optimization process maintained $0.3 < \kappa_{\text{max}} < 0.5$ which justifies the slight deviation from previous convolutional PML implementations mentioned at the end of Section II.

Figure 3 charts the performance of the optimized PML parameters at $\theta_{\text{max}} = \pi/4$ when the test domain's z-dimension is gradually collapsed, sweeping θ_{max} from $\pi/4$ to $87°$. Standard FDTD curves show that as the incidence angle increases, the clear convolutional PML advantage quickly diminishes and it slightly underperfoms both split-field and uniaxial PML for the range $65° < \theta_{\text{max}} < 85°$. The high-order FDTD curves of Fig. 3 demonstrate that the three PML variants achieve better wide-angle performances as they stay below, say, -140 dB up to $\theta_{\text{max}} \approx 80°$, compared to standard FDTD's $\theta_{\text{max}} \approx 75°$.

B. Optimized PML Parameters at $\theta_{max} = 87°$

When the PML parameters were optimized at the extreme incidence angle $\theta_{\text{max}} = 87°$ to best accommodate electrically large models, both standard and high-order FDTD algorithms produced comparable performances across each of the three PML variants as shown in Table 1. On the other hand, there were clear differences among the PML formulations, as uniaxial and convolutional PML afforded roughly 10 dB and 30 dB lower reflection errors, respectively, than split-field PML. As the incidence angle is swept though $\pi/4 < \theta_{\text{max}} < 87°$ (see Fig. 4), all three PML variants more or less maintained flat response. The convolutional PML formulation in particular shows superior extreme angle composure as well as lower overall levels than the other two formulations for both FDTD algorithms. While the reflection error levels in this figure do not match those of Fig. 3, they do represent reliable wide-angle PML performances. Depending on the problem under study, these error levels could be controlled by varying the PML depth d and re-running the optimization routine.

C. Frequency Response of Optimized PML Parameters

To verify that the optimized PML parameters are insensitive to small frequency variations, the detailed

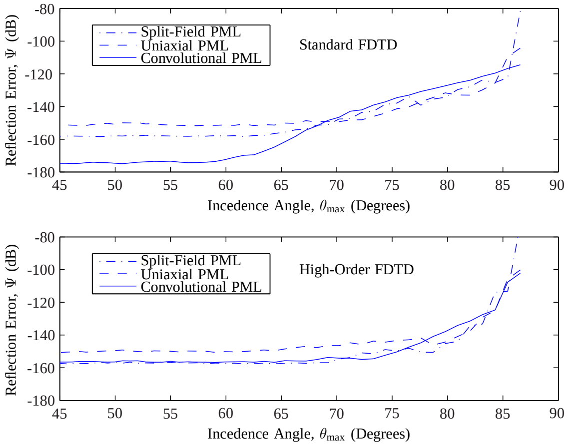

Fig. 3. Comparative wide-angle performance of the three PML formulations when optimized at $\theta_{\max} = \pi/4$.

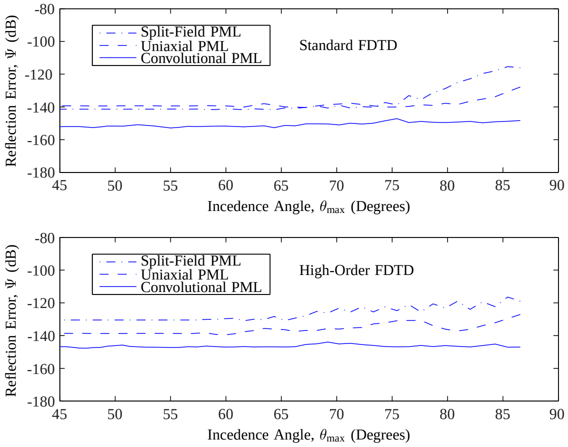

Fig. 4. Comparative wide-angle performance of the three PML formulations when optimized at $\theta_{\max} = 87°$.

experiment in Section III was repeated for convolutional PML and standard FDTD with a unit impulse source replacing equation (19) within a test domain sized $50 \times 50 \times 1$. Two sets of optimized PML parameters, at $\theta_{\max} = \pi/4,\ 87°$, were tested and compared in the power spectral density plots of Fig. 5. (The 100-step time series data were collected at points A and B, marked in Fig. 1.) This comparison illustrates maintained minimal reflection errors except at the frequency range where the spatial grid becomes too coarse to support accurate FDTD simulations. (It should be remembered here that the FDTD grid was designed around 20 cells per wavelength at 1 GHz.)

In gerneral, however, PML parameters are frequency dependent. For example, when the 3-harmonics source of equation(19) was driven with a 60 GHz fundamental, the optimization routine produced $\sigma_{\max} = 38.6781$ S/m and $n_\sigma = 3.7181$ at $\theta_{\max} = \pi/4$ for the split-field PML and standard FDTD, with the same -158 dB error level as in Table 1.

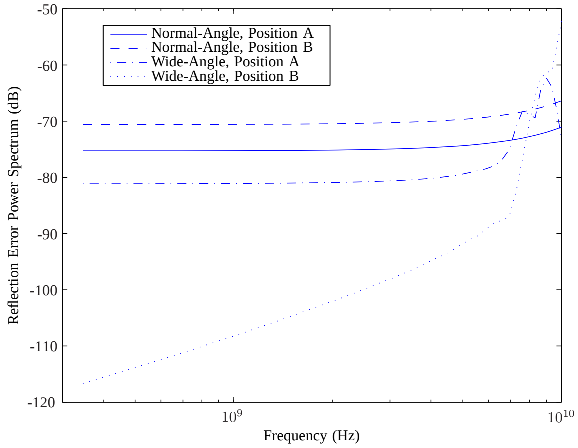

Fig. 5. Reflection errors' frequency response of convolutional PML with standard FDTD using normal-angle and wide-angle PML parameters optimized at $\theta_{\max} = \pi/4$ and $87°$, respectively.

V. CONCLUSION

This work demonstrated that the three main PML variants, Bérenger's original split-field PML, the uniaxial PML and the convolutional PML, are all capable of good outgoing wave absorbing capabilities at near grazing angles. This capability was tested in three-dimensional simulations up to $87°$ incidence angles. The developed optimization process provided different sets of PML parameters depending on how wide an incidence angle is anticipated. This wide-angle performance comes at the expense of reduced absorption capabilities at near normal wave incidence. However, the far more critical advantage of this extreme wide-angle capability is the elimination of the need for prohibitively large scatterer/PML buffer zones when modeling electrically large structures.

Both low-order (standard) FDTD and a high-order FDTD algorithm were tested and optimized for near-normal and near-grazing PML performances. When both were optimized for near-normal incidence angles, the high-order FDTD algorithm demonstrated wider-angle capabilities than standard FDTD, providing flat absorption response across $0 \le \theta \le 80°$ compared to standard FDTD's $0 \le \theta \le 75°$. Of the three PML variants, the convolutional PML formulation demonstrated best wide-angle capabilities. The optimized PML parameters in this work, though frequency dependent in general, were shown to be insensitive to small frequency variations. Optimized PML parameters could be easily implemented in existing FDTD codes with no code changes or added computational burden.

ACKNOWLEDGMENT

This work was supported by Kuwait University, Research Grant No. EE 01/07. The author would also like to thank Prof. Q. H. Liu for hosting him at Duke University, North Carolina for part of this project's duration.

REFERENCES

[1] J. Fang, "Time domain finite difference computation for Maxwell's equations," Ph.D. dissertation, University of California at Berkeley, Berkeley, CA, 1989.

[2] M. F. Hadi and M. Piket-May, "A modified FDTD (2,4) scheme for modeling electrically large structures with high-phase accuracy," *IEEE Trans. Antennas Propagat.*, vol. 45, no. 2, pp. 254–264, Feb. 1997.

[3] E. Turkel and A. Yefet, "Fourth order method for Maxwell's equations on a staggered mesh," vol. 4, pp. 2156–2159, Jul. 1997.

[4] J. B. Cole, "A high-accuracy realization of the Yee algorithm using non-standard finite differences," *IEEE Trans. Microwave Theory Tech.*, vol. 45, no. 6, pp. 991–996, Jun. 1997.

[5] J. L. Young, D. Gaitonde, and J. S. Shang, "Toward the construction of a fourth-order difference scheme for transient EM wave simulation: Staggered grid approach," *IEEE Trans. Antennas Propagat.*, vol. 45, no. 11, pp. 1573–1580, Nov. 1997.

[6] G. J. Haussmann, "A dispersion optimized three-dimensional finite-difference time-domain method for electromagnetic analysis," Ph.D. dissertation, University of Colorado at Boulder, Boulder, CO, 1998.

[7] N. V. Kantartzis and T. D. Tsiboukis, "A higher-order FDTD technique for the implementation of enhanced dispersionless perfectly matched layers combined with efficient absorbing boundary conditions," *IEEE Trans. Magn.*, vol. 34, no. 5, pp. 2736–2739, Sep. 1998.

[8] Y. W. Cheong, Y. M. Lee, K. H. Ra, J. G. Kang, and C. C. Shin, "Wavelet-Galerkin scheme of time-dependent inhomogeneous electromagnetic problems," *IEEE Microwave Guided Wave Lett.*, vol. 9, no. 8, pp. 297–299, Aug. 1999.

[9] E. A. Forgy and W. C. Chew, "A time-domain method with isotropic dispersion and increased stability on an overlapped lattice," *IEEE Trans. Antennas Propagat.*, vol. 50, no. 7, pp. 983–996, Jul. 2002.

[10] H. E. Abd El-Raouf, E. A. El-Diwani, A. Ammar, and F. El-Hefnawi, "A low-dispersion 3-D second-order in time fourth-order in space FDTD scheme ($m3d_{24}$)," *IEEE Trans. Antennas Propagat.*, vol. 52, no. 7, pp. 1638–1646, Jul. 2004.

[11] M. F. Hadi, "A finite volumes-based 3-D low dispersion FDTD algorithm," *IEEE Trans. Antennas Propagat.*, vol. 55, no. 8, Aug. 2007.

[12] M. F. Hadi and R. K. Dib, "Eliminating interface reflections in hybrid low-dispersion FDTD algorithms," *Appl. Computat. Electromag. Soc. J.*, vol. 22, no. 3, pp. 306–314, Nov. 2007.

[13] ——, "Phase-matching the hybrid FV24/S22 FDTD algorithm," *Progress in Electromagnetics Research*, vol. 72, pp. 307–323, 2007.

[14] A. M. Shreim and M. F. Hadi, "Integral PML absorbing boundary conditions for the high-order M24 FDTD algorithm," *Progress in Electromagnetics Research*, vol. 76, pp. 141–152, 2007.

[15] J.-P. Bérenger, "A perfectly matched layer for the absorption of electromagnetic waves," *Journal of Computational Physics*, vol. 114, no. 2, pp. 185–200, 1994.

[16] W. C. Chew and W. H. Weedon, "A 3D perfectly matched medium from modified Maxwell's equations with stretched coordinates," *Microwave Opt. Technol. Lett.*, vol. 7, no. 13, pp. 599–604, Sep. 1994.

[17] Z. S. Sacks, D. M. Kingsland, R. Lee, and J.-F. Lee, "A perfectly anisotropic absorber for use as an absorbing boundary condition," *IEEE Trans. Antennas Propagat.*, vol. 43, no. 12, pp. 1460–1463, Dec. 1995.

[18] S. D. Gedney, "An anisotropic perfectly matched layer-absorbing medium for the truncation of FDTD lattices," *IEEE Trans. Antennas Propagat.*, vol. 44, no. 12, pp. 1630–1639, Dec. 1996.

[19] M. Kuzuoglu and R. Mittra, "Frequency dependence of the constitutive parameters of causal perfectly matched anisotropic absorbers," *IEEE Microwave Guided Wave Lett.*, vol. 6, no. 12, pp. 447–449, Dec. 1996.

[20] J. A. Roden and S. D. Gedney, "Convolution PML (CPML): An efficient FDTD implementation of the CFS-PML for arbitrary media," *Microwave Opt. Technol. Lett.*, vol. 27, no. 5, pp. 334–339, Dec. 2000.

[21] J.-P. Bérenger, "Numerical reflection from FDTD-PMLs: A comparison of the split PML with the unsplit and CFS PML," *IEEE Trans. Antennas Propagat.*, vol. 50, no. 3, pp. 258–265, Mar. 2002.

[22] S. C. Winton and C. M. Rappaport, "Specifying PML conductivities by considering numerical reflection dependencies," *IEEE Trans. Antennas Propagat.*, vol. 48, no. 7, pp. 1055–1063, Jul. 2000.

[23] Y. S. Rickard and N. K. Georgieva, "Problem-independent enhancement of PML ABC for the FDTD method," *IEEE Trans. Antennas Propagat.*, vol. 51, no. 10, pp. 3002–3006, Oct. 2003.

[24] S. Kim and J. Choi, "Optimal design of PML absorbing boundary conditions for improving wide-angle reflection performance," *Electron. Lett.*, vol. 40, no. 2, pp. 104–105, Jan. 2004.

[25] X. L. Travassos, S. L. Avila, D. Prescott, A. Nicolas,

and L. Krähenbühl, "Optimal configurations for perfectly matched layers in FDTD simulations," *IEEE Trans. Magn.*, vol. 42, no. 4, pp. 563–566, Apr. 2006.

[26] N. V. Kantartzis, T. V. Yioultsis, T. I. Kosmanis, and T. D. Tsiboukis, "Nondiagonally anisotropic PML: A generalized unsplit wide-angle absorber for the treatment of the near-grazing effect in FDTD meshes," *IEEE Trans. Magn.*, vol. 36, no. 4, pp. 907–911, Jul. 2000.

[27] R. Holland, L. Simpson, and K. Kunz, "Finite-difference analysis of EMP coupling to lossy dielectric structures," *IEEE Trans. Electromagn. Compat.*, vol. EMC-22, no. 3, pp. 203–209, Aug. 1980.

[28] A. Taflove and S. Hagness, *Computational Electrodynamics: The Finite-Difference Time-Domain Method, 3 ed.* Boston, MA: Artech House, 2005.

Mohammed Hadi his B.S. degree in electrical engineering from Kuwait University in 1988 and his M.S. and Ph.D. degrees from the University of Colorado at Boulder in 1992 and 1996. Dr. Hadi is an Associate Professor at the Electrical Engineering Department of Kuwait University. His research is currently focused on FDTD development for modeling electrically large structures. He also has over a decade's experience in governmental work and consultations in the areas of engineering training, higher education planning and Kuwait's labour profile studies. Dr. Hadi was a Visiting Research Scholar at Duke University, North Carolina during 2007/08.

Extension of the 2-D CP-FDTD Thin Slot Algorithm to 3-D for Shielding Analysis

[1] Xu Li, [2] Ji-h. Yu , [2] Q.-di Wang , and [2] Y.-ming Li

[1] Automotive Engineering Institute of Chongqing Changan Automobile(Group) Co.Ltd, Chongqing P. C. 401120, China
[2] T he State Key Laboratory of Power Transmission Equipment & System Security and New Technology, Chongqing Uniersity, Chongqing P.C. 400030, China

Abstract **–** The two-dimensional CP-FDTD thin slot algorithm is extended to three-dimensions for the application to shielding analysis in electromagnetic compatibility. The accuracy and the applicability of the 3-D CP-FDTD scheme to the slot width were validated with finer mesh model and capacitive thin-slot formalism (C-TSF). The model taken by the comparison is originated from a thin slot in an enclosure wall. The numerical results indicate that the performance or accuracy will descend with the augment of the slot width. Good agreements with the results of finer mesh modeling can be expected as the slot width is on the order of the mesh dimension, and quite large discrepancies from the results of C-TSF with the slot width far less than mesh dimension. The 3D CP-FDTD algorithm will be utilized when the slot width is comparatively large and otherwise C-TSF will be used. Taking advantage of both of them will avoid finer mesh in thin slots modeling such as the shielding analysis of the electronic enclosure.

I. INTRODUCTION

The integrity of shielding enclosures is compromised by apertures and seams required for heat dissipation, cable penetration, and modular construction, among other possibilities [1]. These perforations allow energy to be radiated to the external environment from interior electronics, or energy coupled from the exterior to interfere with interior circuits [2, 3]. An understanding of energy coupling mechanisms to and from the enclosure is essential to minimize the EMI and susceptibility risk in a new design.

Some numerical methods have been applied to solve these EMI/EMC problems such as the finite difference time domain (FDTD) method [4], finite element method (FEM) [5], method of moments (MoM) [6], etc. Among these methods, the FDTD method is one of the most effective tools for the analysis of varieties electromagnetic problems, and has previously been applied for modeling apertures in shielding enclosures. If the physical size of the aperture is on the order of, or larger than the spatial cell size, then modeling this aperture with FDTD is not a problem, however, if the aperture is narrow with respect to the spatial cell, one must either reduce the spatial cell size down to that require to resolve the aperture, or adopt an alternative method to characterize the aperture. The reduction of the cell size is often not a feasible approach, and therefore alternative methods have been investigated [7]. Two of the more popular thin slot formalisms (TSF) have been proposed by Gilbert and Holland (C-TSF) [8] and Taflove (CP-FDTD) [9]. Utilizing these TSF, a thin slot segment can be modeled with a single cell, thereby saving computational resources while retaining accuracy. Previous results for slots in infinite or large planes show C-TSF computation results agree well with experimental data [4]. The two-dimensional (CP-FDTD) study based on contour path method by Taflove generally found superior accuracy of the TSF, but it can’t be applied in solving 3D electromagnetic problems.

To implement the TSF, the two-dimensional CP-FDTD thin slot algorithm is extended to three-dimensional for the application to shielding analysis in electromagnetic compatibility. The accuracy and the applicability of the 3-D CP-FDTD scheme to the slot width were validated with finer mesh model [10] and capacitive thin slot formalism (C-TSF). Results indicate that the 3D CP-FDTD algorithm will be utilized when the slot width is comparatively large and otherwise C-TSF. Taking advantage of both of them will avoid finer mesh in thin slots modeling.

II. C-TSF ALGORITHMS

Different subcellular thin-slot algorithms are employed for modeling thin slots in enclosures and conducting plates. The popular method introduced by Gilbert and Holland [8], denoted herein as the C-TSF, is based on a straight-forward quasi-static approximation. The Yee cells around a slot oriented along *z*-axis is shown in Fig. 1. Employing a quasi static approximation for narrow slots, and assuming the field quantities vary slowly in the *z*-direction, the slot can be viewed as a coplanar, parallel strip capacitor. The slot is then modeled by modifying the relative permittivity and relative permeability in the FDTD algorithm for the electric and magnetic field components in the slot.

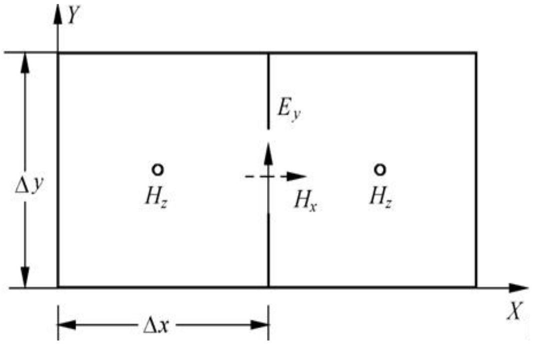

Fig. 1. FDTD cells around the slot for the C-TSF algorithm.

The C-TSF time-marching equations can be obtained for the electric field and magnetic field components in the slot by defining two line integrals, one transverse to the slot, and the other across the slot. These line integrals can be employed with the integral form of Maxwell's equations to obtain modified FDTD update equations for the field components in the slot. An extra parameter results in the finite-difference equation which is the ratio of the two line integrals, and can be shown to be an effective permittivity for the slot. The relative permittivity in the slot is then written as,

$$\varepsilon_{\mathrm{r}} = \frac{1}{\varepsilon_0}\frac{\Delta y}{\Delta x}C \tag{1}$$

where C is the parallel strip per unit length capacitance. The capacitance is evaluated within only one FDTD cell, and is denoted as the in cell capacitance. In order to maintain the free space phase velocity through the slot $v = 1/\sqrt{\varepsilon_r \mu_r \varepsilon_0 \mu_0}$, the relative permeability in the slot is given by $\mu_{\mathrm{r}}=1/\varepsilon_{\mathrm{r}}$. For the slot shown in Fig. 1., the tilde terms are the average values in and across the slot for the electric and magnetic field components, respectively. The slot capacitance per unit length is,

$$\varepsilon_{\mathrm{r}} = \frac{\Delta y}{\Delta x}\frac{K\left[\sqrt{1-w^2/\Delta y^2}\right]}{K\left[w/\Delta y\right]} \tag{2}$$

where $K(\cdot)$ is the complete elliptic integral of the first kind, w is the slot width. The relative permittivity is then related to the slot capacitance by equation (1). Therefore, the electric and magnetic field components in the slot can be updated by modifying only the permittivity and permeability in the respective equations as,

$$E^{n+1}_{y(i,j+1/2,k)} = E^{n}_{y(i,j+1/2,k)} + \frac{\Delta t}{\varepsilon_r \varepsilon_0 \Delta s}\Big[H^{n+1/2}_{x(i,j+1/2,k+1/2)} - H^{n+1/2}_{x(i,j+1/2,k-1/2)} - H^{n+1/2}_{z(i+1/2,j+1/2,k)} + H^{n+1/2}_{z(i-1/2,j+1/2,k)}\Big] \tag{3}$$

$$H^{n+1/2}_{x(i,j+1/2,k+1/2)} = H^{n-1/2}_{x(i,j+1/2,k+1/2)} - \frac{\Delta t}{\mu_r \mu_0 \Delta s}\Big[E^{n}_{y(i,j+1/2,k+1)} - E^{n}_{y(i,j+1/2,k)} - E^{n}_{z(i,j+1,k+1/2)} + E^{n}_{z(i,j,k+1/2)}\Big]. \tag{4}$$

III. 3-D CP-FDTD ALGORITHMS

The CP-FDTD method is not based on Maxwell's equations in differential form but in integral form using Ampère's and Faraday's laws, indicated as follows,

$$\frac{\partial}{\partial t}\iint_s \boldsymbol{H} \bullet \mathrm{d}\boldsymbol{S} = -\frac{1}{\mu}\oint_c \boldsymbol{E} \bullet \mathrm{d}\boldsymbol{L} \tag{5}$$

$$\frac{\partial}{\partial t}\iint_s \boldsymbol{E} \bullet \mathrm{d}\boldsymbol{S} = -\frac{1}{\varepsilon}\oint_c \boldsymbol{H} \bullet \mathrm{d}\boldsymbol{L}. \tag{6}$$

Applying Faraday's law along contour L_1—L_2—L_3—L_4 in Fig. 2, and assuming that the field value at a midpoint of one side of the contour equals the average value of that field component along that side.

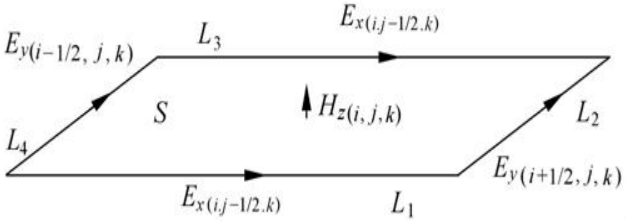

Fig. 2. Faraday's law for H_z .

Now, further assuming that $H_{z(i,j,k)}$ equals the average value of H_z over the surface S, and then the time derivative of H_z can be obtained using a central difference expression, as follows,

$$H_z^{n+1/2}(i,j,k) = H_z^{n-1/2}(i,j,k) - \frac{\Delta t}{S\mu(i,j,k)}\Big[E_x^n(i,j-1/2,k)L_1 + E_y^n(i+1/2,j,k)L_2 - E_x^n(i,j+1/2,k)L_3 - E_y^n(i-1/2,j,k)L_4\Big]. \tag{7}$$

In the same manner, we can obtain other field components.

Figures 3 and 4 illustrate the front view and vertical view of a thin slot, respectively. Width of the slot is g, assuming that the cell size is $\Delta x=\Delta y=\Delta z=\Delta s$. For Fig. 3 field components H_z is assumed to has no variation in the z direction (perpendicular to the slot gap), and the electric components E_y located within the conducting screen are assumed to zero. For Fig. 4 field components E_x are assumed to have no variation in the x direction (across the slot gap).

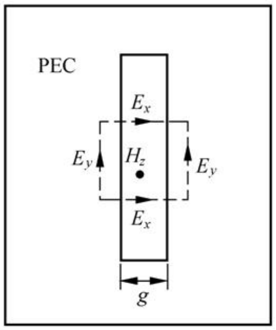

Fig. 3. Vertical view of the thin slot.

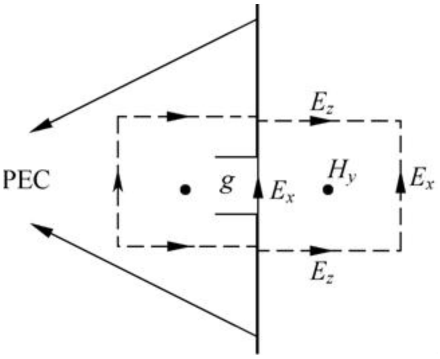

Fig. 4. Front view of the thin slot.

Subject to the foregoing algorithms, lets the contours length L_1=L_3=g, L_2=L_4=Δs for Fig. 3, and then substituting the contours area S=$g\Delta s$ into equation (7), the H_z in Fig. 3 becomes,

$$H^{n+1/2}_{z(i+1/2,j+1/2,k)} = H^{n-1/2}_{z(i+1/2,j+1/2,k)} - \frac{\Delta t}{\Delta s \mu}\left[E^{n}_{x(i+1/2,j+1,k)} - E^{n}_{x(i+1/2,j,k)}\right]. \quad (8)$$

The electric components E_x in Fig. 3 and Fig. 4 can use the basic FDTD method to calculate as follows,

$$E^{n+1}_{x(i+1/2,j,k)} = E^{n}_{x(i+1/2,j,k)} + \frac{\Delta t}{\varepsilon \Delta s}\left[H^{n+1/2}_{z(i+1/2,j+1/2,k)} - H^{n+1/2}_{z(i+1/2,j-1/2,k)} - H^{n+1/2}_{y(i+1/2,j,k+1/2)} + H^{n+1/2}_{y(i+1/2,j,k-1/2)}\right]. \quad (9)$$

The basic FDTD are also used to calculate electric components E_z as follows,

$$E^{n+1}_{z(i,j,k+1/2)} = E^{n}_{z(i,j,k+1/2)} + \frac{\Delta t}{\varepsilon \Delta s}\left[H^{n+\frac{1}{2}}_{y(i+\frac{1}{2},j,k+\frac{1}{2})} - H^{n+\frac{1}{2}}_{y(i+\frac{1}{2},j,k-\frac{1}{2})} - H^{n+\frac{1}{2}}_{x(i,j+\frac{1}{2},k+\frac{1}{2})} + H^{n+\frac{1}{2}}_{x(i,j+\frac{1}{2},k-\frac{1}{2})}\right]. \quad (10)$$

Assuming that the side contour along H_y are Δs, Δs, Δs and g, the contour is Δs^2, then using the time-stepping expression for H_y, and let ω=$g/\Delta s$ we obtain,

$$H^{n+1/2}_{y(i+1/2,j,k+1/2)} = H^{n-1/2}_{y(i+1/2,j,k+1/2)} - \frac{\Delta t}{\mu \Delta s}\left[E^{n}_{z(i+1,j,k+1/2)} - E^{n}_{z(i,j,k+1/2)} - \omega E^{n}_{x(i+1/2,j,k+1)} + E^{n}_{x(i+1/2,j,k)}\right]. \quad (11)$$

The algorithm described above is the basis of the 3-D CP-FDTD method, and equations (8) to (11) are the slot algorithm for computation the field components near the slot gap region.

IV. NUMERICAL RESULTS AND DISCUSSION

To demonstrate the accuracy and applicability of the mentioned 3-D CP-FDTD scheme for EMI issues, a model of metallic rectangular enclosure with one thin slot is presented here as shown in Fig. 5.

The inside dimension of the enclosure is 20cm×40cm×50cm, and the thin slot in an enclosure wall is 8 cm long (x direction) by w cm wide (y direction), as shown in Fig. 6. In our simulation we let w=0.6cm, 0.1cm, 0.01cm, respectively.

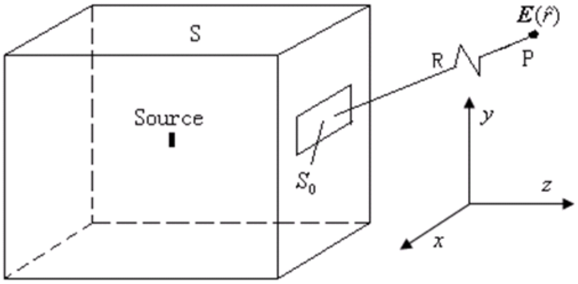

Fig. 5. Shielding enclosure with one slot.

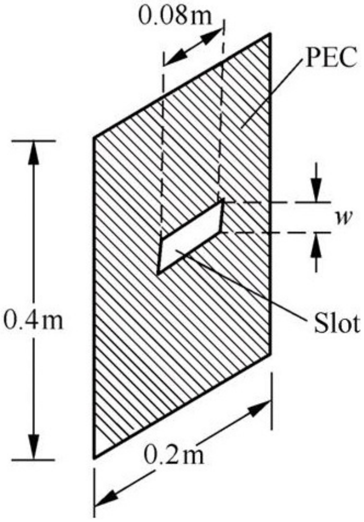

Fig. 6. Thin slot in an enclosure wall.

The elemental electric dipole oriented along x-direction is placed in the center of the enclosure. The electric dipole moment is a Gaussian pulse with T=0.0167ns wide,

$$P(t)=10^{-12}\exp\left[-\left(\frac{t-3T}{T}\right)^{2}\right]. \qquad (12)$$

For the sake of comparison, numerical simulations are carried out using the 3-D CP-FDTD, C-TSF and finer grid FDTD methods. Perfectly matched layer (PML) absorbing boundary conditions are employed for the three dimensional FDTD program and choose the space increments $\Delta x=\Delta y=\Delta z=\delta$. For the 3-D CP-FDTD and the C-TSF method, we choose δ=1cm. For finer grid FDTD method we choose δ=0.2cm.

When the slot width is w=0.6cm, we calculated the electric fields at the point with 10cm far away from the center slot wall by using 3-D CP-FDTD method and finer grid FDTD methods, the time domain and frequency domain simulation results of E_z at the point are shown in Figs. 7 and 8, respectively.

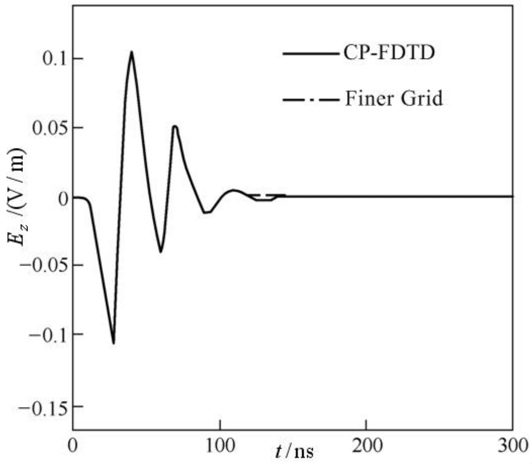

Fig. 7. Time domain results of E_z with 0.6cm slot width by using CP-FDTD and finer grid method.

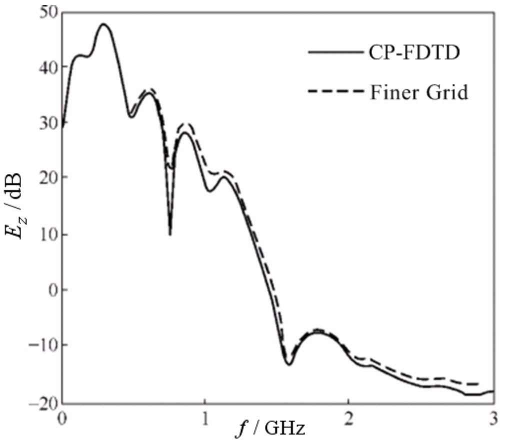

Fig. 8. Frequency domain results of E_z with 0.6cm slot width by using CP-FDTD and finer grid method.

The accurate agreements field simulation results for the slot in Figs. 7 and 8 clearly shows that the proposed 3-D CP-FDTD method can successfully works for the slot width is on the order of the mesh dimension, and can be obtained considerable high computation efficiency compared to the finer grid FDTD method.

It has been demonstrated that EMI issues associated with thin slots can computation efficiency and accuracy by C-TSF method with $w/\delta\leq0.1$, and Two-dimensional (2-D) C-TSF results for plane-wave scattering from a slot in an infinite conducting plane have been shown to agree well with method of moments (MoM) results. Typical discrepancies of less than 10% can be expected for the field quantities at locations near the slot region [10]. So, we calculated the electric field E_z at the same point by using 3-D CP-FDTD and C-TSF methods with slot width w=0.1cm, w=0.01cm, respectively. The frequency domain simulation results are shown in Figs. 9 and 10, respectively.

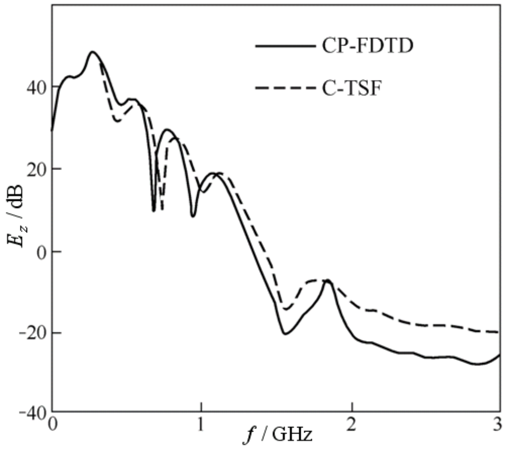

Fig. 9. Frequency domain results of E_z with 0.1cm slot width by using CP-FDTD and C-TSF method.

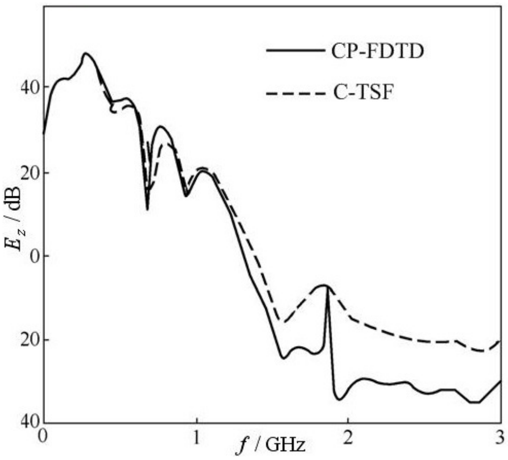

Fig. 10. Frequency domain results of E_z with 0.01cm slot width by using CP-FDTD and C-TSF method.

Figures 9 and 10 show that when w=0.1cm, 0.01cm, the results calculated by the 3-D CP-FDTD method deviate from the results calculated by the C-TSF method significantly, especially when the frequency is high, and it is apparent that result deviation is larger for w=0.01cm than that of for w=0.1cm. So, it is easy to draw a conclusion that with the slot width far less than mesh dimension, the 3-D CP-FDTD will lead to quite large discrepancies from the results of C-TSF, the reason is because the 3-D CP-FDTD based on a quasi-static approximation for narrow slots and we take for field components has no variation near the slot region, but actually field vary greatly when the slot gap is too thin, especially with the slot width far less than mesh dimension.

V. CONCLUSION

In this paper, we extended the two-dimensional CP-FDTD thin slot algorithm to three-dimensions for the application to shielding analysis in electromagnetic compatibility. The accuracy and the applicability of the 3-D CP-FDTD to the slot width were validated with finer mesh model and capacitive thin-slot formalism (C-TSF) model. The numerical results indicate that the performance or accuracy will descend with the augment of the slot width. Good agreements with the results of finer mesh modeling can be expected as the slot width is on the order of the mesh dimension, and quite large discrepancies from the results of C-TSF with the slot width far less than mesh dimension. The 3-D CP-FDTD algorithm will be utilized when the slot width is comparatively large and otherwise C-TSF. Taking advantage of both of them will avoid finer mesh in thin slots modeling such as the shielding analysis of the electronic enclosure.

REFERENCES

[1] H. H. Park and J. W. Lee, “Common-mode current on a wire through a corrugated aperture,” *ETRI Journal*, vol. 24, no. 6, pp. 429-434, 2002.

[2] C. H. Liang and D. K. Cheng, “Electromagnetic fields coupled into a cavity with a slot-aperture under resonant conditions,” *IEEE Trans. Antennas Propagat.*, vol. AP-30, pp. 664-672, July 1982.

[3] Z. Leilei, W. Quandi, Y. Jihui, and G. Qingwen, “A hybrid method based on FDTD for simulation of far field from opening in shielding enclosure**,”** *IEEE Trans. magn.*, vol. 42, pp. 859-862, April 2006.

[4] M. Li and J. Nuebel*,* **“**EMI from cavity modes of shielding enclosures FDTD modeling and measurements**,”** *IEEE Trans. Electromagn. Compat.*, vol. 42, no. 1, pp. 29-37, 2000.

[5] S. T. Mohammed, I. C. George, **“**A hybrid finite element-analytical solutions for inhomogeneously filled shielding enclosures,” *IEEE Trans. Electromagn. Compat.*, vol. 36, no. 4, pp. 380-385, 1994.

[6] M. Li and J. Nuebel, “EMI from airflow aperture arrays in shielding enclosures-experiments, FDTD, and MoM modeling” *IEEE Trans. Electromagn. Compat.*, vol. 42, no. 3, pp. 265-275, 2000.

[7] C.-T. Wu, Y.-H. Pang, and R.-B. Wu, “An improved formalism for FDTD analysis of thin-slot problems by conformal mapping technique,” *IEEE Trans. Antennas Propagat.*, vol. 50, no 9, pp. 2530-2533, 2003.

[8] J. Gilbert and R. Holland, “Implementation of the thin-slot formalism in the finite-difference EMP code THREDII,” *IEEE Trans. Nucl. Sci.*, vol. NS-28, pp. 4269–4274, December 1981.

[9] A. Taflove and K. R. Umashankar, “Detailed FDTD analysis of electromagnetic fields penetrating narrow slots and lapped joint in thick conducting screen,” *IEEE Trans. Antennas Propagat.*, vol. 36, no 2, pp. 247-257, 1988.

[10] C. D.Turner and L. D. Bacon, “Evaluation of a thin-slot formalism for finite-difference time-domain electromagnetics codes,” *IEEE Trans. Electromagn. Compat.*, vol. 30, no. 4, pp. 523-528, 1988.

Li Xu was born in Sichuan Province, China, in 1978. He received his Ph.D degree in collegeof electrical engineering from Chongqing University, Chongqing, China, in 2008. He is currently an EMC Research Engineer in Automotive Engineering Institute of Chongqing ChangAn Automobile (Group) CO.LTD. E-mail: llh_sure@yahoo.com.cn

Yu Ji-hui was born in Hunan province, China in 1944. Currently, he is a professor in college of electrical engineering Chongqing university, Chongqing, China. His main research interests are simulation and numerical computation of electromagnetic field, electromagnetic compatibility, and also in information management system field. E-mail: yujihui@cqu.edu.cn

Wang Quandi was born in Anhui province, China, in 1954. She received her Ph.D degree in College of Electrical Engineering fromChongqing University, Chongqing, China, in 1998. Currently, she is a professor in college of electrical engineering Chongqing university in China. Her main research interests are simulation and numerical computation of electromagnetic field. E-mail: wangquandi@yahoo.com.cn

Li Yong-ming was born in Jiangxi province, China in 1964. He received his Ph.D degree in college of electrical engineering from Chongqing University, Chongqing, China, in 2001. Currently, he is an associate professor in college of electrical engineering Chongqing university in China. His main research interests are simulation and numerical computation of electromagnetic field.
E-mail:cqliym@cqu.edu.

A New Implementation of the Hybrid Taguchi GA: Application to the design of a Miniaturized Log-Periodic Thin-Wire Antenna

[1]**C. M. de J. van Coevorden,** [1]**A. R. Bretones,** [1]**M. F. Pantoja,** [1]**S. G. García,**
[2]**A. Monorchio, and** [1]**R. G. Martín**

[1]Facultad de Ciencias, Departamento de Electromagnetismo, University of Granada,
18071 Granada, Spain
[2]Department of Information Engineering, University of Pisa, I-56126 Pisa, Italy

Abstract – This paper proposes a modification of the hybrid Taguchi-genetic algorithm (HTGA) for solving global numerical optimization problems with continuous variables. The HTGA is a method that combines a conventional genetic algorithm (CGA), which has a powerful global exploration capability, with the Taguchi method, which can exploit the optimum offspring. The Taguchi method is utilized in the HTGA to help in selecting the best genes in the crossover operations. The new implementation proposed in this paper (nHTGA) involves producing, at each generation, a single offspring by Taguchi method, one of its parents being the best individual found so far, instead of repeatedly applying Taguchi to generate several individuals with both parents selected at random as HTGA does. Moreover, the efficiency of the algorithm is enhanced by only crossing via Taguchi individuals with a high enough number of different genes. The performance of the proposed HTGA is assessed by solving several benchmark problems of global optimization with large number of dimensions and very large numbers of local minima. The computational experiments show that the new algorithm causes a reduction, sometimes drastic, in the number of function calls, i.e. in computational time, for all the benchmark problems proposed. As an example of application of this novel algorithm to a real-world problem, the optimization of an ultra-broadband zigzag log-periodic antenna is carried out and discussed.

Keywords: Genetic algorithm, numerical optimization, Taguchi method, log-periodic antenas, zig-zag antenas.

I. INTRODUCTION

Genetic algorithms (GAs) [1] have come a long way toward solving optimization problems [2] where conventional optimization methods fail, such as system identification [3], design [4–7], scheduling [8], routing [9], control [10, 11], and others [12]. The GAs have been demonstrated to be robust stochastic search and optimization techniques. These algorithms are a type of evolutionary algorithms based on Darwin's theory of evolution. In GA, a population of N_{pop} individuals (trial solutions) evolve in parallel by means of selection of the fittest individuals, crossover and mutation of genes. Because of its implicit parallelism [2], and a reasonable tradeoff between global and local search abilities, the GAs are considered to be robust global optimization algorithms. However, one obstacle when applying GAs to optimize complex problems where the evaluation of functions is computationally intensive is the high computational cost due to their slow convergence rate.

Many efforts have been dedicated to accelerate the convergence of GAs, such as studying optimal crossover and mutation rates or selecting appropriate genetic operators [13]. More recently, new algorithms combining GAs with local searchers have been proposed to improve the performance of GAs on global optimization problems [14–17]. In particular, Tsai et. al. presented a hybrid algorithm, called HTGA, which combines the conventional GA (CGA) [2] with the Taguchi method by inserting a Taguchi-method-based crossover between crossover and mutation operators [17]. The Taguchi method selects two random individuals from offspring already resulting from crossover and recombines them, creating a single individual via an orthogonal array experiment. The systematic reasoning ability of the Taguchi method helps to select the best genes to achieve the crossover, and consequently enhance the genetic algorithm. The process is repeated until the expected population size is met. The hybrid method was demonstrated to be more robust, statistically sound, and quickly convergent than the ones proposed previously in [14–16].

In this paper, a new implementation of the HTGA is proposed. The new hybrid method, named nHTGA, is based on the hypothesis that two low-quality parents have little chance of beating, by crossover and mutation, the best individual found so far. Therefore, the offspring of two of the worst individuals in the population resulting from an orthogonal array experiment will be, in most cases, a low-quality individual, resulting in a waste of function calls, i.e. a waste of computational time. To avoid this, we propose some modifications of the HTGA code. The main one is that, at each generation of the

GA process, only one of the new offspring is produced via Taguchi method, the best individual found so far being one of its parents. With this, we expect to save computational resources as we avoid useless matrix experiments between individuals whose offspring don't have much chance of improving the performance of the best individual in the population. Moreover, the number of experiments needed to find the optimal solution in the whole nHTGA process is further reduced by requiring a certain degree of diversity of the two chromosomes to be mated via Taguchi method.

This paper is organized as follows. Section II briefly describes the Taguchi method, the fundamentals of the nHTGA and compares the performance of the new algorithm with that of HTGA and that of other algorithms frequently used in engineering applications. As an example of application, in Section III the nHTGA is used to optimize the performance of a log-periodic thin-wire antenna.

II. THE NHTGA

A. The Taguchi Method

The Taguchi method is a robust design approach based on improving the quality of a product by minimizing the effect of the causes of variation without eliminating the causes [18]. Two major tools are used in the Taguchi method, orthogonal arrays (OAs) and the signal-to-noise ratio (SNR). In laboratory experimentation, OAs are used for determining which combinations of factor levels to use for each experimental run and for analyzing the data. OAs are matrixes of numbers arranged in rows and columns where a row represents the level of all factors in a given experiment, and a column represents the values assigned to a specific factor in the various experiments. The array is called orthogonal because columns can be evaluated independently of one another.

In this paper, we will work with two-level OA whose general nomenclature is $L_n(2^{n-1})$ where n is the number of experimental runs, n-1 the number of columns in the array (or number of factors involved in the experiments), and 2 the number of possible different values (or levels) that a factor can take. A simple algorithm for the construction of OAs can be found in [16]. An example of an OA is given in table 1, where the OA indicates 8 possible experiments determined by specific combinations of two levels (values 1 or 2) of 7 different variables (A-G). According to OA's theory, the 8 experiments are selected so that they provide a balanced comparison of the two possible levels of any factor.

The other parameter concerning the Taguchi method is the SNR, which has been traditionally used in engineering to measure the quality of a product corresponding to a specific choice of the values taken by the variables involved in a design. The SNR, for a set of quality characteristics of a given product, is related to the mean squared deviation from the target value of those quality characteristics. Several definitions of the SNR can be found depending on the type of characteristic and on the type of problem. Taguchi has generalized the concept of SNR and applied it to the assessment of the influence of the possible values of the different factors involved in a set of experiments. SNR is usually defined so that it is large for favorable situations. For example, in the GA application described in this paper, the SNR of a given experiment (chromosome or individual) will be defined in terms of the fitness function corresponding to that experiment in such a way so that better individuals correspond to greater values of SNR.

Table 1. Orthogonal array $L_8(2^7)$.

	Factors						
	A	B	C	D	E	F	G
experiment	column number						
number	1	2	3	4	5	6	7
1	1	1	1	1	1	1	1
2	1	1	1	2	2	2	2
3	1	2	2	1	1	2	2
4	1	2	2	2	2	1	1
5	2	1	2	1	2	1	2
6	2	1	2	2	1	2	1
7	2	2	1	1	2	2	1
8	2	2	1	2	1	1	2

The SNR helps on converting several repetitions of the value taken by a variable into a single number that accounts for the quality of the final product if that repeated value of the given variable is used. To this end, given a set of N experiments described by a specific OA, the effect of each variable involved is defined as,

$$E_{i,j} = \sum_{k}^{n} \delta(level(i,k) - j) SNR(k) \qquad i = 1, ..., N_v; j = 1, 2 \tag{1}$$

where N_v is the number of variables; i represents the ith-variable; k is the number of experiment; $level(i,k)$ is the level (1 or 2) taken by the ith-variable in the kth-experiment and j is either 1 or 2 (two effects are defined for each variable). The sum includes only the SNR of experiments where the level of factor i is equal to j as indicated by the delta of Kronecker symbol δ. For example, in the two-level OA of table 1, $E_{i,1}$ and $E_{i,2}$ can be defined for a given column i (i=1,..,7); $E_{i,1}$ corresponds to the sum of the SNR of all experiments where the value of factor i is equal to 1, and $E_{i,2}$ corresponds to experiments where the value of the ith-factor is equal to 2. An example of application is given in the next subsection, and, for further details, the reader is refereed to [18].

B. Generation of optimal offsprings by Taguchi method

The Taguchi method can be used to generate an optimal offspring from the mating of two parents with N_v genes. The process starts by selecting an appropriate orthogonal array $L_n(2^{n-1})$ with with $n-1 \geq N_v$ and by defining a fitness function that measures the quality of a given chromosome. The fitness function $F(k), k = 1,...,n$ is evaluated for each of the n experiments in the OA and a signal-to-noise ratio, SNR(k), is defined in terms of $F(k)$. Subsequently the effect, $E_{i,j}$, of the various factors in the SNR is calculated for each factor (gene or column in the array) $(i = 1,..,N_v)$ and each level $(j = 1, 2)$ of that factor using equation (1).

To clarify the process, let us consider the problem of finding a chromosome, k_{best}, formed by the 7 genes, $C(i, k_{best}), i = 1,...,7$, that maximize the test function,

$$f(k) = \sum_{i=1}^{7} \sin\left(C(i,k)\right) \tag{2}$$

where k refers to an specific chromosome whose genes take the values $C(i,k), i = 1,...,7$, respectively. The values permitted for each $C(i,k)$ are discrete fractions of π, ranging from 0 to π. In this context, we would perform the mating of the two 7-gene chromosomes (7 factors) given in Table 2 via Taguchi with the aid of the $L_8(2^7)$ OA given in Table 1. Table 3 shows the eight different chromosomes corresponding to the eight different experiments. The process starts with the definition of the fitness function that evaluates the goodness of a chromosome as $F(k) = \frac{f(k)}{7}$ and the calculation of the $SNR(k)$, defined in this case as $SNR(k) = F(k)^2$, for each experiment, $k = 1,...,8$, in the OA. The values of $F(k)$ and $SNR(k)$ are shown in the 9th and 10th columns in Table 3. Then the effects, $E_{i,1}$ and $E_{i,2}$, of the various genes are calculated for $i = 1,..,7$ using equation (1), resulting in the values given in Table 3. As the optimal level for each factor is decided by the larger value of either $E_{i,1}$ or $E_{i,2}$, the process resulted in the optimal levels ”2, 1, 1, 2, 2, 2, 1” for each of the seven factors respectively and therefore in the optimal chromosome given in Table 3.

Table 2. The two 7-gene chromosomes.

Chromosome 1:	$\pi/9$	$\pi/2$	$\pi/2$	$\pi/3$	$\pi/9$	$4\pi/5$	$\pi/2$
Chromosome 2:	$\pi/2$	$\pi/3$	$\pi/5$	$\pi/2$	$\pi/2$	$\pi/2$	$2\pi/3$

C. The HTGA method

The HTGA is based on the insertion of the Taguchi method between the crossover and mutation operations in a CGA. The stages in the HTGA algorithm are [19]:

1) Appropriate parameters needed for the implementation of the algorithm are decided such as the probability of crossover, p_{cross}, and probability of mutation, p_{mut}.
2) A suitable two-level OA for matrix experiments is selected.
3) A population of N_{pop} individuals is randomly created.
4) The N_{pop} individuals performance is evaluated according to the specific objective or fitness function at hand.
5) A roulette wheel selection is applied.
6) On average, p_{cross} chromosomes undergo one-point crossover as in the CGA.
7) Two chromosomes from the current population are randomly selected and mated via the Taguchi experiments, producing an optimal offspring as explained in the previous subsection. This step is repeated $\frac{1}{2} \times p_{cross} \times N_{pop}$ times.
8) Mutation with a probability of p_{mut} is applied.
9) The N_{pop} better chromosomes are selected to be the parents of the next generation.
10) Steps 5 to 9 are repeated until the stopping criterion is met.

This hybrid algorithm, which combines the powerful global exploration capabilities of GA with that of the Taguchi method for producing optimum offspring, was proven in [19] to be fast converging, robust, and statistically sound when applied to optimize several high-dimension benchmark problems.

D. The nHTGA method

In this paper we propose a new hybridization of the Taguchi and GA methods (i.e. the nHTGA) which is sketched in Figs. 1 and 2. The objective is to improve the efficiency of the Taguchi method by decreasing the total number of fitness-function evaluations (function calls) needed to find the optimal solution of the problem at hand. To this aim, as we commented in the Introduction, instead of applying Taguchi method $\frac{1}{2} \times p_{cross} \times N_{pop}$ times to mate two randomly selected individuals each time (step 7 in the previous subsection), we just produce an 'optimal' offspring per generation using the Taguchi-based crossover operator. That offspring is the descendant of the best chromosome found so far and one chromosome randomly selected with the only condition of being different enough from its mate according to a criterion explained below. This means that the number of function calls per generation is reduced from $\frac{1}{2} \times p_{cross} \times N_{pop} \times n$ in the HTGA to n in the nHTGA, being n the number of experiments in the appropriate Taguchi OA. The idea behind the modifications is that two bad-quality individuals will not likely be candidates to produce a chromosome with a better performance than that of the best chromosome in the current population.

Aiming to reduce even more the number of function calls, we set a rule to select the second individual to be mated via Taguchi in such a way that we avoid redundant

Table 3. Generating a better chromosome from two chromosomes by using the Taguchi method.

	Factors								
	A	B	C	D	E	F	G		
	Column number								
Experiment Number(k)	1	2	3	4	5	6	7	F(k)	SNR(k)
1	$\frac{\pi}{9}$	$\frac{\pi}{2}$	$\frac{\pi}{2}$	$\frac{\pi}{3}$	$\frac{\pi}{9}$	$4\frac{\pi}{5}$	$\frac{\pi}{2}$	0.7340	0.5387
2	$\frac{\pi}{9}$	$\frac{\pi}{2}$	$\frac{\pi}{2}$	$\frac{\pi}{2}$	$\frac{\pi}{2}$	$\frac{\pi}{2}$	$2\frac{\pi}{3}$	0.8869	0.7865
3	$\frac{\pi}{9}$	$\frac{\pi}{3}$	$\frac{\pi}{5}$	$\frac{\pi}{3}$	$\frac{\pi}{9}$	$\frac{\pi}{2}$	$2\frac{\pi}{3}$	0.6957	0.4840
4	$\frac{\pi}{9}$	$\frac{\pi}{3}$	$\frac{\pi}{5}$	$\frac{\pi}{2}$	$\frac{\pi}{2}$	$4\frac{\pi}{5}$	$\frac{\pi}{2}$	0.7691	0.5915
5	$\frac{\pi}{2}$	$\frac{\pi}{2}$	$\frac{\pi}{5}$	$\frac{\pi}{3}$	$\frac{\pi}{2}$	$4\frac{\pi}{5}$	$2\frac{\pi}{3}$	0.8439	0.7122
6	$\frac{\pi}{2}$	$\frac{\pi}{2}$	$\frac{\pi}{5}$	$\frac{\pi}{2}$	$\frac{\pi}{9}$	$\frac{\pi}{2}$	$\frac{\pi}{2}$	0.8471	0.7176
7	$\frac{\pi}{2}$	$\frac{\pi}{3}$	$\frac{\pi}{2}$	$\frac{\pi}{3}$	$\frac{\pi}{2}$	$\frac{\pi}{2}$	$\frac{\pi}{2}$	0.9617	0.9249
8	$\frac{\pi}{2}$	$\frac{\pi}{3}$	$\frac{\pi}{2}$	$\frac{\pi}{2}$	$\frac{\pi}{9}$	$4\frac{\pi}{5}$	$2\frac{\pi}{3}$	0.8088	0.6542
E_{i1}	2.4007	$\underline{2.7551}$	$\underline{2.9044}$	2.6599	2.3945	2.4967	$\underline{2.7727}$		
E_{i2}	$\underline{3.0090}$	2.6546	2.5053	$\underline{2.7498}$	$\underline{3.0152}$	$\underline{2.9130}$	2.6370		
Optimal level	2	1	1	2	2	2	1		
Optimal chromosome	$\frac{\pi}{2}$	$\frac{\pi}{2}$	$\frac{\pi}{2}$	$\frac{\pi}{2}$	$\frac{\pi}{2}$	$\frac{\pi}{2}$	$\frac{\pi}{2}$	1	1

experiments. Note that if, for example, we perform a matrix experiment using the OA in Table 1 with two individuals in which factors D to G are the same for both, experiments 1 and 2 will be the same, as also will be experiments 3 and 4, 5 and 6, and 7 and 8. Thus in this application of the Taguchi method, we waste four function evaluations since several experiments are repeated. In Appendix A, we describe an empirical study aimed at deciding how many experiments are redundant as a function of the number of genes with repeated values of the two mating individuals. We give an example for the case of an OA $L_{32}(2^{31})$ and $N_v = 30$. We conclude that no matrix experiments should be made if the difference between individuals is less than 15%, since nearly half of the experiments will have been already performed, resulting in a waste of computational resources. As a rule of thumb, in the present work we increase this threshold up to 25%.

E. Benchmark testing

Next we assess the performance of the nHTGA algorithm by solving several global numerical optimization problems, which fulfill the conditions to form a suitable touchstone to check the performance of evolutionary algorithms [19]. In particular, we consider the minimization of the 30-dimensional functions ($N = 30$) described in table 4 by applying the nHTGA and subsequently compare our results with the ones reported in [19].

We apply the nHTGA using a smaller population ($N_{pop} = 20$) than the one reported in [19], where HTGA was employed to solve the same problems with $N_{pop} = 200$. Therefore, in order to make a fair comparison, we increase the crossover and mutation rates to $p_{cross} = 1$ and $p_{mut} = 0.2$ so that we have the same number of fitness-function evaluations per generation due to the action of the genetic operators than in HTGA. On the other hand, as it was previously commented, we use a Taguchi-based crossover operator was used only once in each evolutionary cycle, on individuals with at least one quarter of the genes being different. Both the nHTGA and the HTGA use real encoding where each chromosome is represented by a vector of N floating-point numbers, i.e, $x_1, ..., x_N$. The criterion for stopping the execution of the nHTGA algorithm is that the value of the fitness function of the best individual in the population should be less than or equal to the mean function value reported in [20] using HTGA. Aiming for statistically robust results, each test function minimization problem is performed 50 times.

The mean number of fitness-function evaluations, the mean function value of the optimized solution calculated

Table 4. Benchmark of test functions.

Test Function	Feasible Solution Space
$f_1 = \sum_{i=1}^{N} \left(-x_i \sin\left(\sqrt{\lvert x_i \rvert}\right)\right)$	$[-500, 500]^N$
$f_2 = \sum_{i=1}^{N} \left(x_i^2 - 10\cos(2\pi x_i) + 10\right)$	$[-5.12, 5.12]^N$
$f_3 = -20\exp\left(-0.2\sqrt{\frac{1}{N}\sum_{i=1}^{N} x_i^2}\right)$ $-\exp\left(\frac{1}{N}\sum_{i=1}^{N}\cos(2\pi x_i)\right)$ $+20 + \exp(1)$	$[-32, 32]^N$
$f_4 = \frac{1}{4000}\sum_{i=1}^{N} x_i^2 - \prod_{i=1}^{N}\cos\left(\frac{x_i}{\sqrt{i}}\right) + 1$	$[-600, 600]^N$
$f_5 = \frac{1}{10}\left\{\sin^2(3\pi x_1) + \sum_{i=1}^{N} -1(x_i - 1)^2\left[1 + \sin^{(3\pi x_{i+1})}\right]\right.$ $\left.+(x_N - 1)^2\left[1 + \sin^{(3\pi x_N)}\right]\right\} + \sum_{i=1}^{N} u(x_i, 5, 100, 4)$	$[-50, 50]^N$
$f_6 = \sum_{i=1}^{N} x_i^2$	$[-100, 100]^N$
$f_7 = \sum_{i=1}^{N} \lvert x_i \rvert + \prod_{i=1}^{N} \lvert x_i \rvert$	$[-10, 10]^N$

over the 50 runs, and the standard deviation of the function values were all calculated for each test function and are presented in Table 5. Note as the table reflects, the new nHTGA gives closer to optimal solutions than the HTGA and moreover uses a lower mean number of fitness-function evaluations, greatly improving the efficiency of the algorithm. In this table we also show these data when a CGA is used (numerical results extracted from [16]).

III. LOG PERIODIC ANTENNA DESIGN

The Taguchi method has been applied to some electromagnetic optimization problems [21, 22] with success. In this work we employ the nHTGA hybrid GA and Taguchi method algorithm to optimize the design of a thin-wire antenna that must fulfill the following requirements throughout the operating band, which ranges from 450MHz to 1.35GHz:

1) Standing voltage wave ratio (SVWR) less than 2 (referenced to 75Ω)
2) Gain range (GR) less than 3dB.
3) Gain (G) greater than 5dB.
4) Front-to-back ratio (FTB) greater than 15dB.
5) Beamwidth (BW) in azimuth greater than 120°.
6) Vertical polarization.

Moreover, as the antenna is going to be mounted on a pole, its environmental impact needs to be reduced and therefore, its greatest dimension is required to be less than or equal to half of thewavelength at the lowest frequency, i.e. $\lambda_{low}/2 = 0.33m$.

To satisfy the above requirement we have considered symmetrical log-periodic antennas (LP) as suitable starting points in our designs, because LP antennas are vertically polarized, endfire radiators, and possess good FTB ratios [23].

A. *LP antenna geometry*

Log periodic antennas are radiators for which the geometry is chosen so that the electrical properties are repeated periodically with the logarithm of frequency. The first successful design of this type of antenna was proposed by DuHammel and Isbell in [24], setting a new starting point for a variety of sheet and wire LP designs [25], [26]. Among this family of antennas, the symmetrical log-periodic antennas [27] focus our interest since they provide a promising model to be optimized with the nHTGA tool in an effort to fulfil all the design specifications described above. In particular, log-periodic bent zigzag antennas (LPBZA) as the one studied in [28] were considered the starting point of our design because they do not need any phase-reversal transformers to achieve broadband performance and they are less sensitive than the bent-monopole antenna [23]. An example of a basic thin-wire LPBZA antenna is schematized in Fig. 3, where only one arm of the antenna is represented, as the antenna is symmetric with respect to the XY plane. The geometrical factor τ is the ratio of two adjacent similar dimensions of the antenna ($\tau = R_{n+2}/R_n < 1$); α_E and α_S are the angles between tip to tip on the vertical and horizontal planes of the zigzag antenna, respectively; ξ is the distance between the two antenna arms and N_t

Table 5. Comparison between HTGA and nHTGA under the same evolutionary environment.

Test function	Mean number of function evaluations			Mean function value (standard deviation)			Globally minimal function value
	nHTGA	HGTA	CGA	nHTGA	HGTA	CGA	
f_1	14677	163468	458653	-12569.4655 (0.0077)	-12569.46 (0)	-8444.7583 (65.7326)	-12569.5
f_2	5596	16267	335993	0 (0)	0 (0)	22.967 (0.7800)	0
f_3	7989	16632	336481	0 (0)	0 (0)	2.697 (5.668×10^{-3})	0
f_4	19282	20999	346971	0 (0)	0 (0)	1.258 (1.657×10^{-2})	0
f_5	14405	59003	348356	0.9×10^{-4} (1×10^{-5})	1×10^{-4} (0)	2.978 (7.210×10^{-2})	0
f_6	8917	20844	181445	0 (0)	0 (0)	4.9655 (11.3614)	0
f_7	6747	14285	170955	0 (0)	0 (0)	7.9315×10^{-1} (5.5943×10^{-1})	0

the number of tips in one arm (in the particular case shown in Fig. 3 $N_t = 7$). The antenna is excited with a voltage source at its center (see Fig. 3). In our designs, the radius of the wire, r, is constant, despite breaking the log-periodicity, in order to facilitate the future construction of the antenna.

Next, we modify the geometry of the LPBZA antennas in order to reduce their size so that the design specifications regarding the compact size of the antenna are fulfilled. With this aim, we have considered two alternative ways of keeping the antennas maximum dimension smaller that $\lambda_{low}/2$: 1) either we reduce to $\lambda_{low}/4$ (since the antenna is symmetrical over the XY plane) the height of the tooth that exceed the limit imposed (as in Fig. 4(b)); or, 2) following the ideas already presented in [29], we bend the antenna tooth in a quasi-fractal way until the antenna shrinks to the appropriate dimensions (see Fig. 4(c)). With the first option the number of peaks is kept invariant, while the second option maintains the total length of the wire.

Furthermore, to increase the electrical size of the antennas without increasing their physical size, we propose to use resistive loads located along the antenna geometries. The use of resistive loading is crucial to operate within the required frequency range and to broaden the bandwidth. This is due to the fact that, in LP antennas, most of the radiation takes place in the region where the dipole length ranges from $\lambda/2$ to $3\lambda/2$ [23]. Then, since the maximum height of our antenna must be less than $\lambda_{low}/2$, energy with a wavelength greater than approximately $\lambda_{low}/3$ will not be fully radiated if the antenna is made of perfect electric conducting wires. One way to solve this is to lengthen the wires electrically by means of loading the antenna segments with a resistive profile.

B. Antenna optimization

In this subsection, we describe how the nHTGA approach has been applied in conjunction with the method-of-moments-based NEC code to optimize the performance of an LPBZA. The design parameters are α_E, α_S, τ, ξ and the value of the resistance per unit length loading the antenna structure, which, to keep the problem tractable, is chosen to be constant for each tooth of the LPBZA and ranges from 0 Ω/m to 100 Ω/m. LPBZA, both with reduced tooth size and with bent teeth, are being considered. The radius of the wire is r=2mm, the number of tips $N_t = 25$ and, for practical reasons, designs with segments shorter than 2cm are not permitted. The variation range of the geometrical design parameters is shown in Table 6.

Table 6. Parameter design range.

Parameter	Min. Value	Max. Value
α_E	25 (deg)	65 (deg)
α_S	25 (deg)	65 (deg)
τ	0.8	0.95
ξ	6 (mm)	20 (mm)
Ω	0 (Ω/m)	100 (Ω/m)

The nHTGA starts by generating an initial population of $N_{pop} = 20$ LPBZA antennas which are encoded using real values. Then, to measure the goodness of a given individual, we define a fitness function as a weighted aggregation of the different objectives described at the

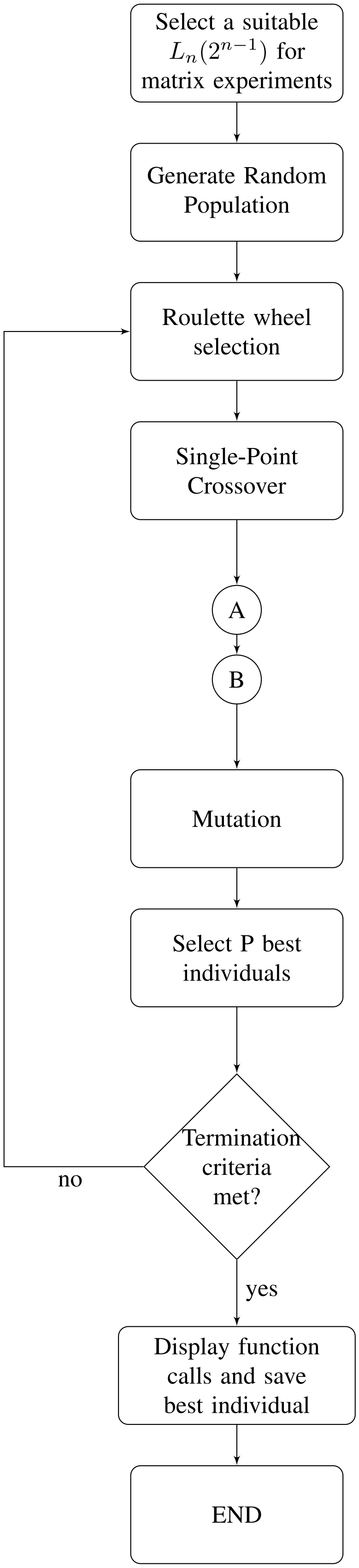

Fig. 1. Flowchart of the nHTGA for global numerical optimization problem.

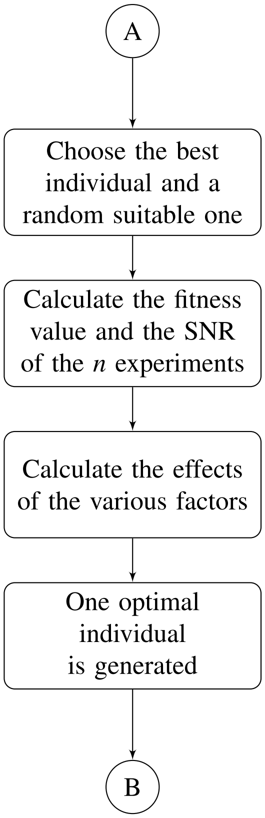

Fig. 2. New implementation of the Taguchi method over a GA.

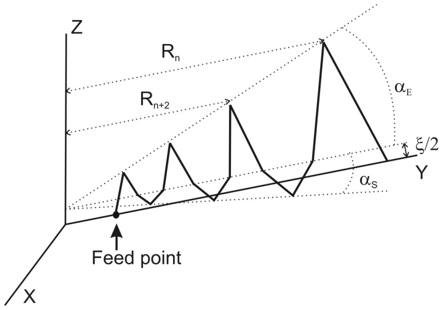

Fig. 3. Geometry of a single arm of the LPBZA.

beginning of this section as,

$$F = \frac{1}{N_\nu}\sum_{i=1}^{N_\nu}\varpi(\nu_i)\times \left[\frac{1}{4}\Theta\left(\frac{2}{SVWR(\nu_i)}\right)+\frac{1}{8}\Theta\left(\frac{3}{GR(\nu_i)}\right)+ \frac{1}{8}\Theta\left(\frac{G(\nu_i)}{5}\right)+\frac{1}{4}\Theta\left(\frac{FTB(\nu_i)}{15}\right)+\frac{1}{4}\Theta\left(\frac{BW(\nu_i)}{120}\right)\right] \tag{3}$$

where

$$\Theta(x) = \begin{cases} 1 & \text{if } x \geq 1 \\ x & \text{otherwise} \end{cases} \tag{4}$$

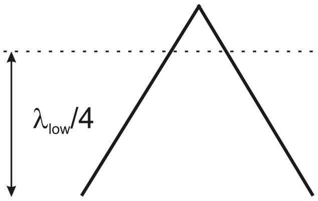

(a) Original

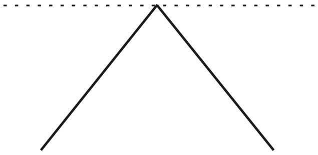

(b) Option 1

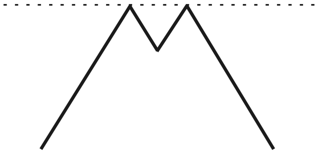

(c) Option 2

Fig. 4. Miniaturization techniques applied to an oversized tooth (a), by decreasing the tooth height (b), and by bending the tooth on a quasi-fractal way (c).

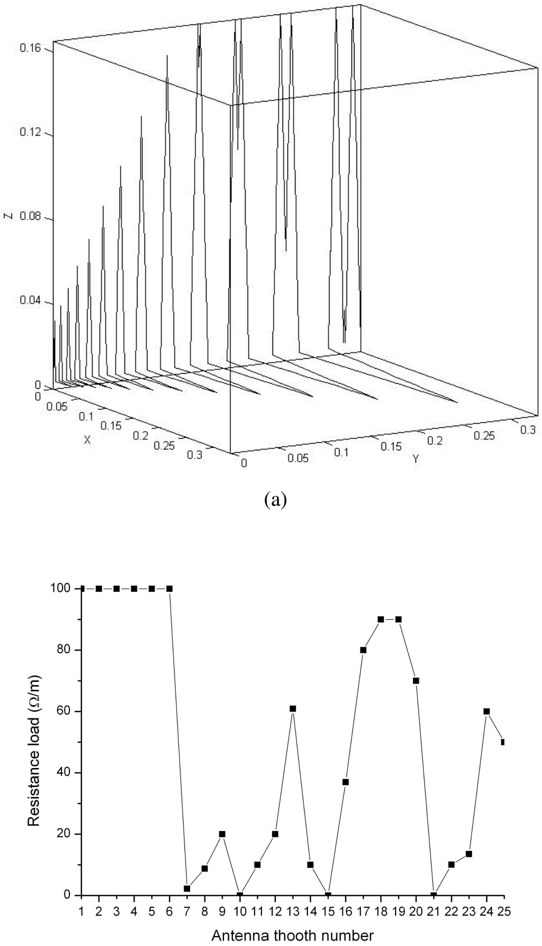

(a)

(b)

Fig. 5. Optimized LPBZA. (a) Geometry of the optimized antenna. (b) Resistive loading profile for each tooth in the optimized antenna.

and $\varpi(\nu) = C(1/\nu^3 + \nu^8)$ is a normalized weighting function that gives more importance to the accomplishment of the objective functions at the edges of the frequency band. N_ν is the number of frequency samples and ν the frequency in GHz. F is defined so that its maximum value, 1, is achieved by any antenna that fulfils all the design requirements. Thus, the application of the nHTGA operators makes the population evolve towards better antenna designs, i.e. towards individuals with higher F values.

C. Numerical results

The nHTGA code has been applied three times to ensure that the code has not been trapped in a local maximum. The best antenna found had a value of the fitness function F equal to 0.9856. Its geometry, shown in Figure 5(a), corresponds to $\tau = 0.815$, $\alpha_E = 44.691°$, $\alpha_H = 41.000°$, $\xi = 6.746\ mm$. The 25 teeth in each arm have been miniaturized in a quasi-fractal way and the resistive profile for each teeth is shown in Fig. 5(b) (the tooth are numbered from larger to smaller sizes).

The performance of the resulting antenna has been analyzed using NEC and the results are given in Figs. 6 and 7. The input impedance, normalized to $Z_0 = 75\Omega$, is plotted on a Smith chart in Fig. 6(a). The impedance plot lies at the center of the Smith chart, with all the points inside the 2:1 circle, meaning the fulfilment of objective 1 ($SVWR \leq 2$). Moreover, the impedance is balanced and can be matched to a 75Ω commercial coaxial cable without using an impedance transformer. From Fig. 6(b), which represents the gain versus frequency, it can be seen that the gain ranges from 5dB to 8dB within the band, satisfying requirements 2 ($GR \leq 3dB$) and 3 ($G \geq 5dB$).

Figure 6(c) plots the antenna 3dB horizontal beamwidth vs. frequency, which is found to be greater than $120°$ throughout the frequency range except for three frequency samples that, in any case, correspond to beamwidth values quite close to $120°$. On the other hand, the front-to-back ratio, which is represented in Fig. 6(d) vs. frequency, is greater than 15dB, except for a couple of frequencies near the low-frequency part of the band, where values are around 12dB. Therefore, objectives 4 ($FTB \geq 15dB$) and 5 ($BW \geq 120°$) have been approximately accomplished.

Finally, Fig. 7 displays, for five different frequencies within the operating antenna bandwidth, the gain as a function of the horizontal angle ϕ. The behavior of the gain with frequency is similar in the five cases, therefore corroborating the broadband antenna performance, and the figure also confirms that the design objectives in terms

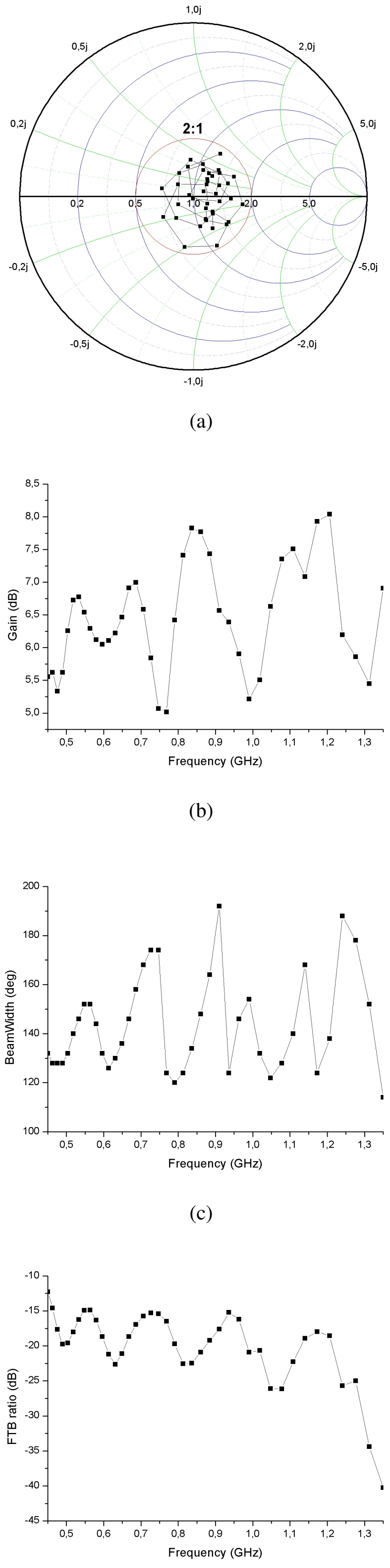

(a)

(b)

(c)

(d)

Fig. 6. Performance of the optimized LPBZA. (a) Input impedance on the Smith chart referenced to $Z_0 = 75\Omega$.(b) Gain in the endfire direction. (c) Beamwidth on the horizontal plane. (d) Front-to-back ratio.

of gain, beamwidth, and front-to-back ratio, have been accomplished for the five selected frequencies.

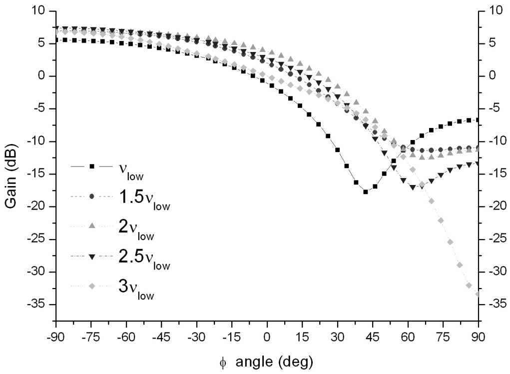

Fig. 7. Gain in the horizontal plane $(\theta = 90°)$ versus ϕ for the optimized LPBZA. $\nu_{low} = 450MHz$ is the lowest frequency of the considered band.

IV. CONCLUSION

A new implementation of the HTGA is proposed in this paper. Hybrid techniques combining the Taguchi method with traditional GAs incorporate Taguchi orthogonal arrays between the crossover and mutation operators to produce chromosomes with the best combination of design variables or genes. After the conventional GA gene-mating process, the new HTGA proposed here produces only one individual in each generation via the Taguchi-based crossover operator. The new individual is the Taguchi children of the best individual found so far and one selected at random. This process differs from previous versions of HTGA, where a percentage of the whole population at each generation is generated via Taguchi method. The computational solution of several test cases demonstrates that the proposed hybrid algorithm outperforms the HTGA and traditional GAs in terms of evolutionary efficiency. Finally an example of application of the nHTGA is given carrying out the optimization of a log-periodic thin-wire miniature antenna.

APPENDIX A
EFFICIENCY OF MATRIX EXPERIMENTS $L_{32}(2^{31})$

In this appendix, we explain how to perform a numerical experiment conceived to determine how many function evaluations are redundant in a matrix experiment when two individuals with several genes in common are crossed via Taguchi method. We propose to implement the following steps:

1) Two N_v-genes chromosomes are randomly generated.

2) N_{equal} genes of the two previous chromosomes are forced to be identical. The specific equal genes are selected at random.
3) The matrix of experiments that results from crossing the two chromosomes via Taguchi is built.
4) The number of different experiments is counted.

The numerical experiment is conducted one hundred times, each time varying $N_{equal} = 1 \ldots N_v$ (instead of considering all the $\frac{N_v!}{(N_v - N_{equal})! N_{equal}!}$ possibilities for N_{equal}). The number of different experiments found in average are plotted versus $\frac{N_{equal}}{N_v} \times 100$ and, from that graph, conclusions can be reached on how to select N_{equal} in order to avoid a certain percentage of redundant matrix experiments. As an example, Fig. 8 shows the results for the case of N=31 genes and the OA $L_{32}(2^{31})$. It plots the number of different matrix experiments (in average) versus the percentage of different genes in the pairs of 31-genes mating chromosomes considered. It can be seen that if at least 25% of the genes of the individuals going to be mated through Taguchi are different, just around the 2% of the matrix experiments are repeated. Therefore it seems reasonable to require the differences in genes to be greater than at least 25%. Numerical experiments with other OA lead to similar conclusions.

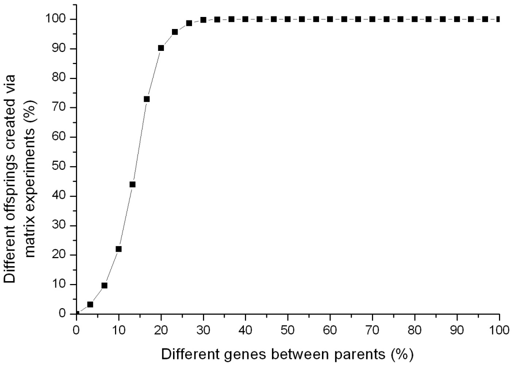

Fig. 8. Number of different experiments versus the percentage of different genes for the case of the OA $L_{32}(2^{31})$.

ACKNOWLEDGEMENT

This work was supported in part by the Spanish Projects TEC-2004-06217-C02-01, TEC-2004-04866-C04-03, PTR95-1025.OP.01, the training program and project of excellence TIC1541 of Junta de Andalucia.

REFERENCES

[1] K. de Jong, "Analysis of the behavior a class of genetic adaptative systems," Ph.D. dissertation, Dept. Comput. Commun. Sci., Univ. Michigan, Ann Arbor, 1975.

[2] D. Goldberg, *Genetic Algorithms in Search, Optimization, and Machine Learning*. Reading, MA: Addison-Wesley, 1989.

[3] K. Kristinnson and G. Dumont, "System identification and control using genetic algorithms," *IEEE Trans. Syst., Man, Cybern.*, vol. 22, no. 5, pp. 1033–1046, 1992.

[4] M. F. Pantoja, A. Monorchio, A. R. Bretones, and R. G. Martín, "Direct GA-based optimization of resistively loaded wire antennas in the time domain," *Electronic Letters*, vol. 36, no. 24, pp. 1988–1990, Nov. 2000.

[5] G. Manara, A. Monorchio, and R. Mittra, "Frequency selective surface design based on genetic algorithm," *Electronic Letters*, vol. 35, no. 17, pp. 1400–1401, Aug. 1999.

[6] C. M. de J. van Coevorden, S. G. García, M. F. Pantoja, A. R. Bretones, and R. G. Martín, "Microstrip-patch array design using a multiobjective GA," *IEEE Antenna Wireless and Propagation Letters*, vol. 4, pp. 100–103, Nov. 2005.

[7] C. M. de J. van Coevorden, A. R. Bretones, M. F. Pantoja, F. Ruiz, S. G. García, and R. G. Martín, "Ga design of a thin-wire bow-tie antenna for gpr applications," *IEEE Trans. Geosci. Remote Sens.*, vol. 44, no. 4, pp. 1004–1010, Apr. 2006.

[8] S. Uckun, S. Bagchi, and K. Kawamura, "Managing genetic search in job shop scheduling," *IEEE Expert*, vol. 8, no. 5, pp. 15–24, 1993.

[9] J. Lienig, "A parallel genetic algorithm for performance-driven VLSI routing," *IEEE Trans. Evol. Comput.*, vol. 1, no. 1, pp. 29–39, Apr. 1997.

[10] B. Dike and R. Smith, "Application of genetic algorithms to air combat maneuvering," pp. 84–94, 1993.

[11] M. Ito, F. Zhang, and N. Yoshida, "Collision avoidance control of ship with genetic algorithm," pp. 1791–1796, 1999.

[12] L. Jin, C. Yao, and X. Huang, "An improved method on meteorological prediction modeling using genetic algorithm and artificial neural network," *The Sixth World Congress on Intelligent Control and Automation*, pp. 31–35, 2006.

[13] T. Back, D. Fogel, and Z. Michalewicz, Eds., *Handbook on evolutionary computation*. IOP Publishing Ltd and Oxford University Press, 1997.

[14] J. Renders and H. Bersini, "Hybridizing genetic algorithms with hill-climbing methods for global optimization: two possible ways," *Proceedings of the First IEEE Conference on Evolutionary Computation*, pp. 312–317, 1994.

[15] J. Yen, J. Liao, B. Lee, and D. Randolph, "A hybrid approach to modeling metabolic systems using a genetic algorithm and simplex method," *IEEE Trans. Syst., Man, Cybern. B*, vol. 28, no. 2, pp. 173–191, Apr. 1998.

[16] Y. Leung and Y. Wang, "An orthogonal genetic algorithm with quantization for global numerical optimization," *IEEE Trans. Evol. Comput.*, vol. 5, no. 1, pp. 41–53, Feb. 2001.

[17] J. Tsai, T. Liu, and J. Chou, "Hybrid Taguchi-genetic algorithm for global numerical optimization," *IEEE Trans. Evol. Comput.*, vol. 8, no. 4, pp. 365–377, Aug. 2004.

[18] G. Taguchi, S. Chowdhury, and Y. Wu, *Taguchi's Quality Engineering Handbook*. John Wiley and sons, Inc., 2004.

[19] J. Tsai, J. Chou, and T. Liu, "Tuning the structure and parameters of a neural network by using hybrid taguchi-genetic algorithm," *IEEE Trans. Neural Netw.*, vol. 17, no. 1, pp. 69–80, Jan. 2006.

[20] J. Tsai, T. Liu, and J. Chou, "Optimal design of digital iir filters by using hybrid taguchi genetic algorithm," *IEEE Transactions on Industrial Electronics*, vol. 53, no. 3, pp. 867–879, Jun. 2006.

[21] W.-C. Weng, F. Yang, and A. Elsherbeni, "Linear antenna array synthesis using taguchi's method: A novel optimization technique in electromagnetics," *Antennas and Propagation, IEEE Transactions on*, vol. 55, no. 3, pp. 723–730, March 2007.

[22] W.-C. Weng, F. Yang, and A. Z. Elsherbeni, *Electromagnetics and Antenna Optimization Using Taguchi's Method*. Morgan and Claypool, 2007.

[23] R. Johnson and H. Jasik, *Antenna engineering handbook*, 2nd ed. McGray Hill, 1984.

[24] R. DuHamel and D. Isbell, "Broadband logarithmically periodic antenna structures," *IRE Int. Conv. Rec.*, vol. 5, pp. 119–128, Mar. 1957.

[25] R. DuHamel and F. Ore, "Logarithmically periodic antenna designs," *IRE Int. Conv. Rec.*, vol. 6, pp. 139–151, Mar. 1958.

[26] D. Isbell, "Log periodic dipole arrays," *IEEE Trans. on Antennas and Propagation*, vol. 8, no. 3, pp. 260–267, May 1960.

[27] D. Berry and F. Ore, "Log periodic monopole array," *IRE Int. Conv. Rec.*, vol. 9, pp. 76–85, Mar. 1961.

[28] J. Greiser and P. Mayes, "The bent backfire zigzag - a vertically polarized frequency-independent antenna," *IEEE Trans. Antennas Propag.*, vol. AP-11, pp. 281–299, May 1964.

[29] S. Sharma and L. Shafai, "Investigations on miniaturized endfire vertically polarized quasi-fractal log-periodic antenna," *IEEE Trans. Antennas Propag.*, vol. 52, pp. 1957–1962, Aug. 2004.

Analysis of the Behavior of Sierpinski Carpet Monopole Antenna

M. Naghshvarian-Jahromi and N. Komjani-Barchloui

Department of Electrical Engineering,
Iran University of Science and Technology (IUST), Narmak, Tehran, Iran

Abstract **–** Three fractal monopole antennas using the Sierpinski carpet geometry is described in this paper. The idea for these designs is gotten from semi-log-periodic behavior of fractal antenna. In this paper, we noted input impedance matching of antennas throughout the passband of them. In this point of view, we will apply the wideband, broadband and multiband for these antennas. Our first wide-band design is named antenna-1. This has a good input impedance match throughout the passband 2-20GHz. Second antenna is named antenna-2. This antenna has an interesting behavior while has a multi-band behavior from 1-7GHz and has broad-band behavior from 7-20 GHz. However, because of two slots in ground plane of this antenna, the 6-7GHz band is eliminated. Third of antennas is named antenna-3. It has a multi-band behavior from 0.5-17GHz. On average, we could match input impedance of proposed antennas, for three desired behavior. The dimension of main- square for antenna-1, antenna-2 and antenna-3 is 45, 60 and 132 mm respectively. These antennas are suitable for the operating bands of GSM, ICMS, UMTS, Bluetooth, WLAN and HIPERLAN systems.

Keyword: Fractal antenna, sierpinski-carpet, semi-log-periodic behavior.

I. INTRODUCTION

Modern telecommunication systems require antennas with wider bandwidths and smaller dimension rather than conventional ones. In recent years several fractal geometries have been introduced for antenna applications with different level of success in antenna characteristics improvement. Some of these geometries are reported recently [1, 2]. These are low profile antennas with moderate gain, and are able to be operative at multiple frequencies [3]. Generated monopolar mode polarization is interested especially for applications in ICMS, UMTS, Bluetooth, WLAN and HIPERLAN systems [4, 5].

Several fractal shapes have been introduced in recent years too. Certain fractal designs have been shown to be self-similar, small, space filling and have log periodic performances when used as antennas [6, 7]. In [8] capability of two new fractal geometries for application in antenna design is described. In [9] dual-band monopole antenna using the concept of Sierpinski carpet shape and semi-circular geometry is introduced and has interesting property.

In this paper, the behavior of Sierpinski carpet monopole antenna is described by means of experimental and computational results and we could match input impedance of antenna, for three desired behavior.

II. THE PROPOSED ANTENNA CONFIGURATION

The square patch was selected for initial design. Figure 1 shows the Sierpinski carpet iteration up to third repetitions.

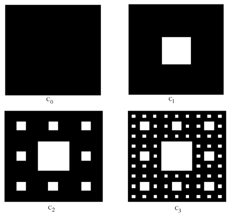

Fig. 1. Sierpinski carpet antenna up to third iteration.

Figure 2 and table 1 show the geometrical parameters of the Sierpinski carpet antenna for three desired designs.

Table 1. The geometrical parameters of the three Sierpinski carpet antennas.

	W_1 (mm)	W_2 (mm)	W_3 (mm)	W_4 (mm)
Antenna-1	45	15	5	1.67
Antenna-2	60	20	6.67	2.22
Antenna-3	132	44	14.67	4.9

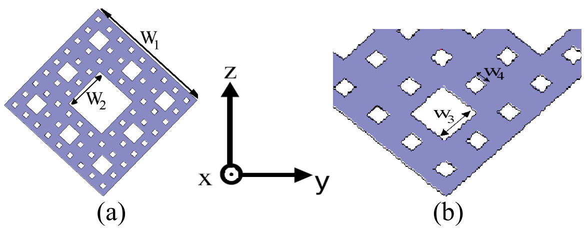

(a) (b)

Fig. 2. Geometrical parameters of Sierpinski carpet antenna in proposed design.

The ground plane of this antenna is very interesting and is the same as ground plane in [8, 9]. The size of ground-plane is approximately 110 mm for all antennas [8].

The radiation elements of antenna-1 and antenna-2 are printed on Rogers RO4003 with thickness of 60mil. For antenna-3, radiation element is printed on FR4-epoxy with thickness of 63mil. These elements are fed at apexes. Figure 3 shows the final design and the pictures of three antennas.

(a) (b) (c)

Fig. 3. The pictures of proposed antennas (a) Antenna-1, (b) Antenna-2, and (c) Antenna-3.

III. INPUT RETURN LOSS OF ANTENNAE

These antennas were simulated on Ansoft HFSS V10 using a FEM algorithm. The return loss of proposed antennas was also measured with hp8720 network analyzer from 0.5-20GHz. Figure 4 (a), (b), and (c) show the reflection coefficient relative to 50 Ω of three-monopole together. The plots corresponding to the antenna-3 antenna-2 and antenna-1 appear at the top row, middle row and bottom row respectively. Figure 5 shows all measured proposed antennas in one plot from 0.5 GHz - 20 GHz.

Antenna-1 achieved a good match with return loss about -9dB throughout the pass-band from 2 to 20 GHz. But, antenna-2 has the multiband behavior from 1-7 GHz and has broadband behavior from 7-20 GHz. However, 6-7GHz eliminated for this antenna. Because, two slots is made in ground plane of this antenna. These slots aren't simulated in HFSS and it can be seen for this band simulation and measurement results and they don't resemble together. Multi-band behavior for antenna-3 is very obvious. The obtained results for this antenna shows this antenna can operate in most commercial bands, such as: GSM900, ICMS, DECT, WLAN and HIPERLAN.

Of course, we used tiny absorber in back of antenna-1 which is shown in Fig. 6. This absorber has imaginary part of permittivity and permeability, and we couldn't simulate effect of this in our design. Because of this, there is noticeable difference between simulation and measurement results in higher frequencies.

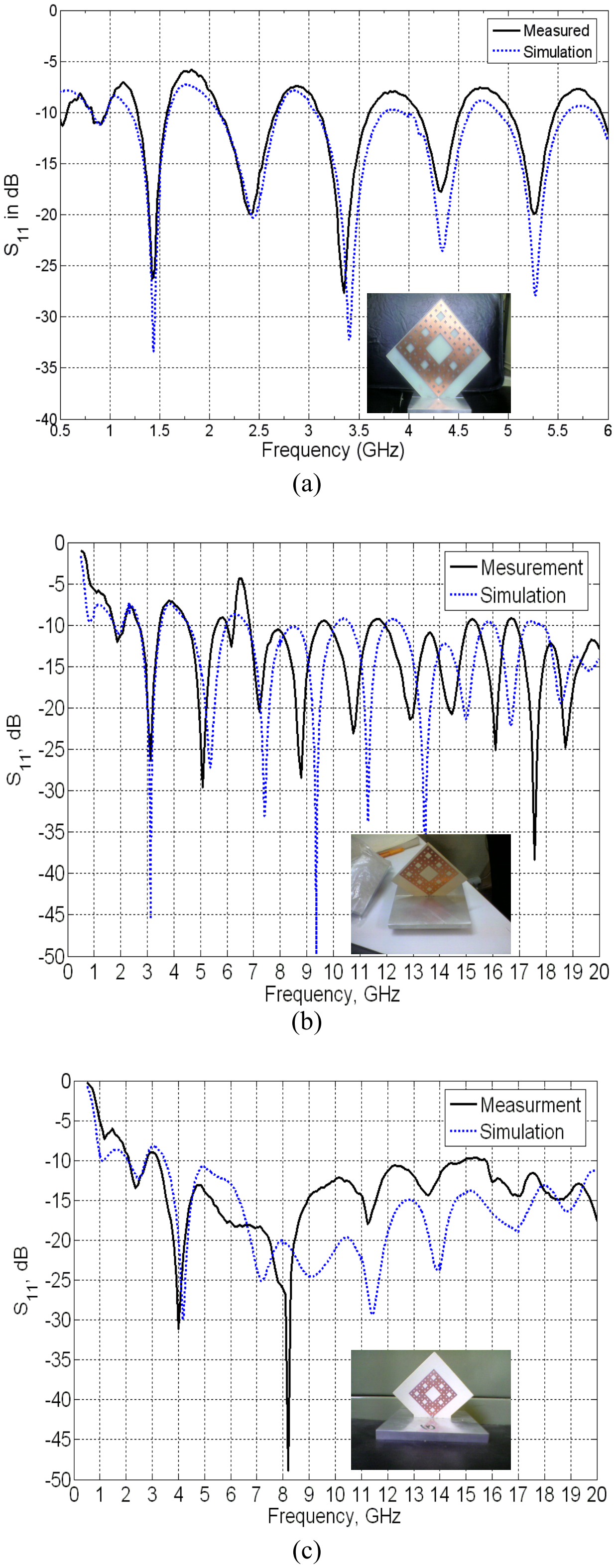

(a)

(b)

(c)

Fig. 4. Input reflection coefficient of three monopole Sierpinski carpet antenna (a) Antenna-3, (b) Antenna-2, and (c) Antenna-1.

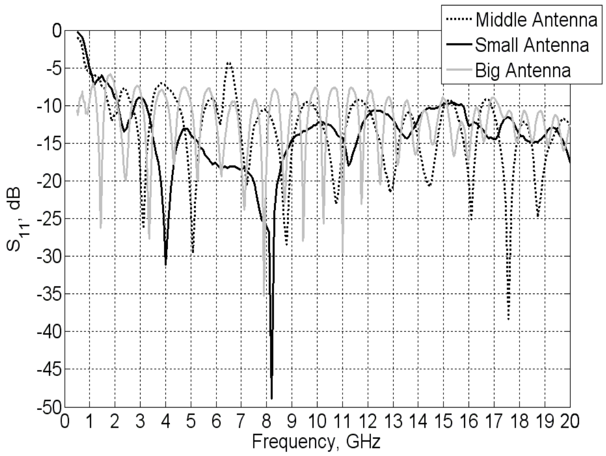

Fig. 5. Compare the measured reflection coefficient of the proposed antennas.

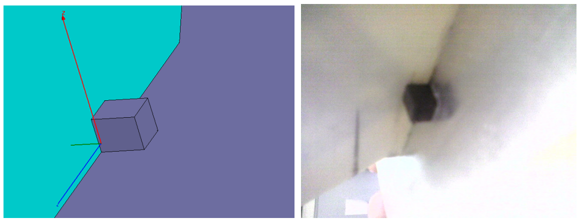

(a) (b)

Fig. 6. Absorber is used in antenna-1 (a) simulation, (b) implementation.

To get better insight on the log-periodic behavior of these antennas, in Fig. 7 the measured input impedance frequency is shown in logarithmic scale to emphasize the semi-log-periodic behavior of the proposed antennas.

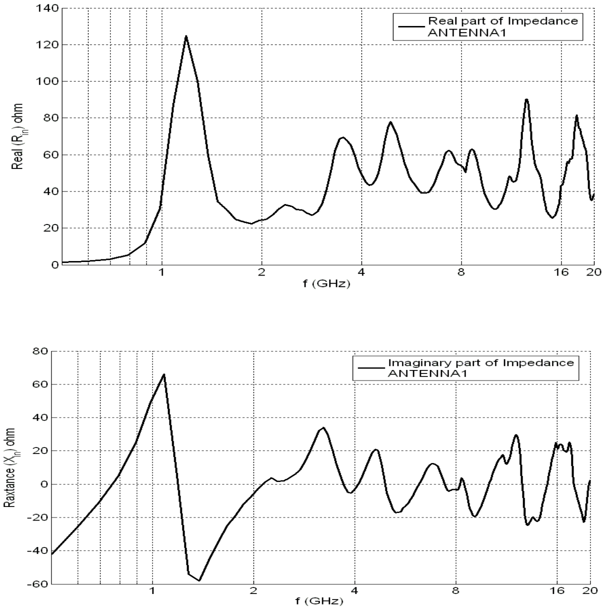

(a) Antenna-1

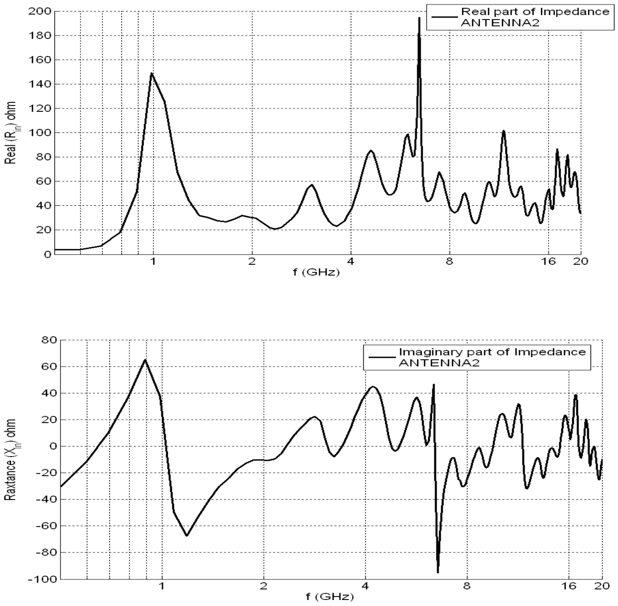

(b) Antenna-2

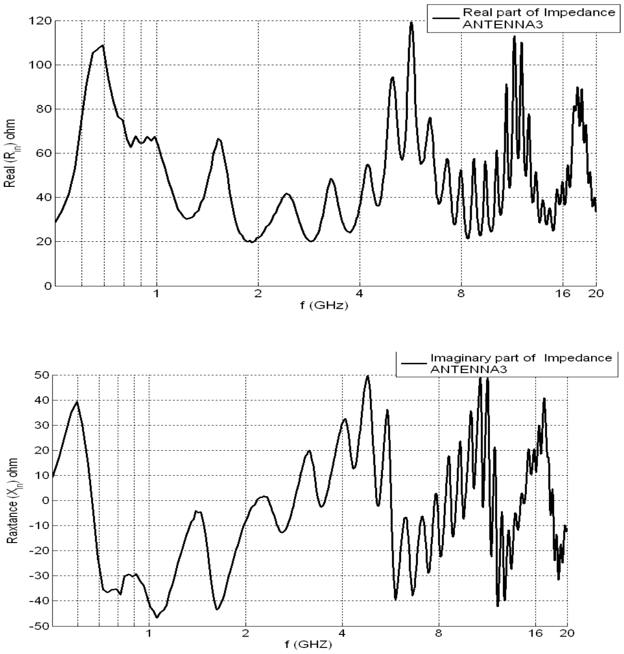

(c) Antenna-3

Fig. 7. Measured input resistance (top) and input reactance (bottom) of three monopole antennas.

IV. RADIATION PATTERNS

Figure 8 (a) and (b) show radiation patterns of antenna-1 and antenna-2 correspond to operating bands of 1.89, 2.4 and 5.2 GHz representing DECT, WLAN and HIPERLAN bands respectively. Figure 8 (c) shows radiation patterns of antenna-3, correspond to operating bands of 0.9, 2.4 and 5.2 GHz representing GSM900, WLAN and HIPERLAN bands. In all plots, the black-line is Co-polarization pattern and the gray-line shows Cross-polarization pattern. The top row of each plot shows the E-plane radiations while the bottom row shows the H-plane radiations. Because of symmetry and flatness, good radiation patterns are obtained for these bands. However, it should be noticed that the effect of the finite size of the ground-plane must be taken into account when analyzing the patterns on these figures [10]. For instance, those at upper bands show characteristic ripple, which is due to diffraction at the edges of the plane. The variations on the ripple are faster when frequency is increased since the squared plane is not self-scalable and edges are spaced a longer distance in terms of corresponding wavelength. Also, the expected null in the z-axis direction is hidden by the contribution of the anti-symmetrical mode of the ground plane overall radiated power [10].

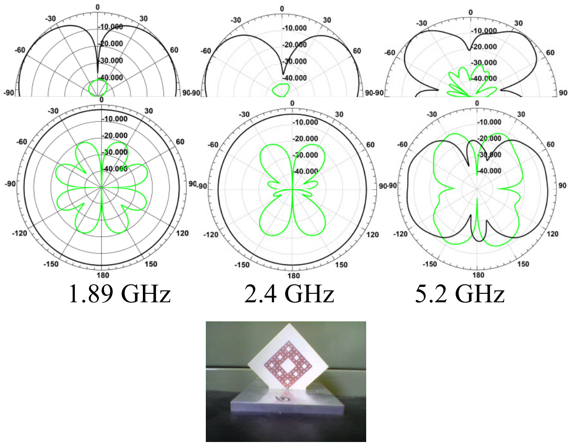

(a) Antenna-1

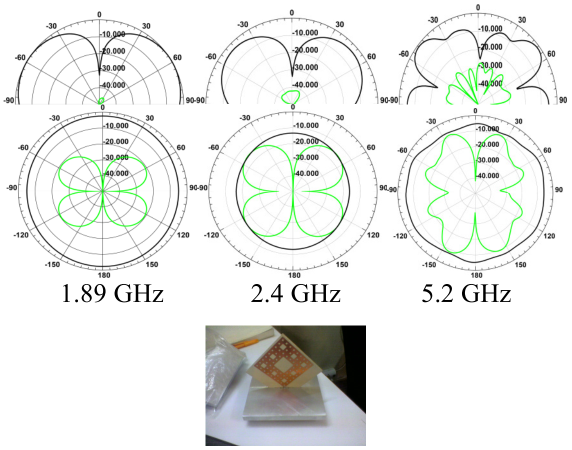

(b) Antenna-2

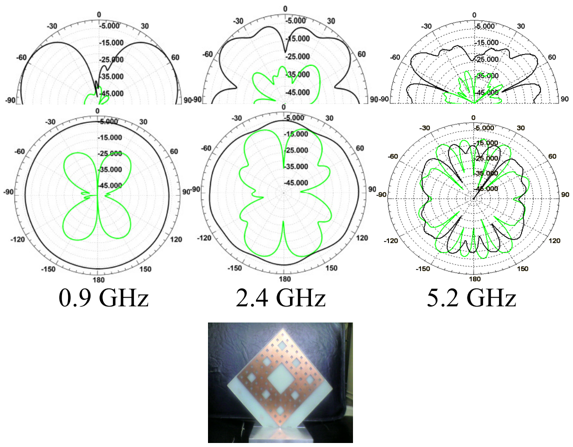

(c) Antenna-3

▬ Co-polarization
▬ Cross polarization

Fig. 8. Radiation pattern of proposed antennas (Top row of each plot is E-plane, Bottom row is H-plane).

V. MEASURED GAIN

The peak gain of the proposed antennas was measured (in dB) for some of frequencies in operating bands of each one. These are shown in Table 2. Minimum gain is 3.23 dB in measurement frequencies. In results, these antennas have moderate gain. Increase in peak antenna gain is expected when operating frequency is increased. But the minimum gain is in higher frequencies. The reason of this event is back-scattering from edge of ground plan. It forms ripples and nulls in radiation pattern of antennas. That cause reduction in gain of proposed antennas and the gain doesn't depend on frequency and geometry of antenna, exactly.

Table 2. Gain of proposed antenna, measured at various frequencies in operating bands.

	Antennas Gain (dB)		
Frequency (GHz)	Antenna-1	Antenna-2	Antenna-3
0.9	☒	☒	4.43
1	3.69	3.23	☒
1.89	☒	☒	5.96
2.4	4.03	5.46	4.97
5.2	6.6	6.3	9
8	5.47	7.62	☒
11	6.05	9.74	☒
14	5.48	9.4	☒
17	4.91	8.57	☒
20	6.98	9.64	☒

VI. THE PHISICAL INSIGHT FOR THESE DESIGNS

The idea for these designs is gotten from semi-log-periodic behavior of fractal antenna. In each conventional fractal structure and each repetition, many resonance edges are made. The edges of the each square are subtracted from the original square contribute to make resonance behavior with other edges of fractal shape. However, the resonance behavior of each edge in relation with other edges in Sierpinski carpet is very complicated and requires further study about the resonance behavior of this shape. For the antenna-1, the resonance edges of each repetition have balanced resonance frequency and with small increase in frequency in smaller wavelength, cause the majority of edges contributes to produce resonance behavior. However, we observed small mismatch in lower operating frequencies (between 2 GHz - 3.5 GHz) obviously, because of unbalancing resonance frequency of each iteration edges from other iteration edges. In antenna-2, the same phenomenon occurs. But mismatches cause multi-band behavior from 1 GHz - 7 GHz. Because of balanced resonance frequencies of iteration edges, broad-band behavior is observed from 7-20 GHz. In antenna-3, this reason (unbalancing resonance frequencies edges) cause multi-band behavior in all operating frequencies.

VII. CONCLUSION

The three fractal monopole antennas are designed using Sierpinski carpet geometry. For antenna-1 designs achieved an approximate 10:1 match for 50 Ω feeding port. Antenna-2 has multi-band behavior from 1-7 GHz and has broadband behavior for 7 GHz - 20 GHz. For this antenna, band from 6-7 GHz is eliminated. Antenna-3 has multi-band behavior and can apply for most of commercial bands. On average, the radiation patterns are suitable for current application in the GSM900, ICMS, UMTS, Bluetooth, WLAN and HIPERLAN bands. The results obtained for the antennas show capabilities of fractal geometry for wireless communications considering multi-band and wideband operations.

Furthermore, with such an antenna design, a wide range of wireless communication systems, considering frequency selective channel characteristics with multi-media transmission would become possible [8, 9].

ACKNOWLEDGEMENTS

The authors would like to thank Faramoj-Pajouh-engineering Company in Iran, for their invaluable assistance and funding for this research which is a small part of UMTS project. We would like to thanks Dr. S. A. Abrishamifar, Dr. A. Malahzedeh and Mr. H. Rahmanian-Koushkaki for invaluable assistance for this project.

REFERENCES

[1] J. Gianvittorio and Y. R. Samii, “Fractal patch antenna,” Department of Electrical Engineering, University of California, Los Angeles, 2001.

[2] K. J. Vinoy, *Fractal shaped antenna elements for wide and multi-band wireless applications*, PhD Thesis, Pennsylvania State University, 2002.

[3] M. K. A. M. Z. A. Rahim, A. Aziz, and N. Abdullah, “Wideband Sierpinski carpet monopole antenna,” *2005 Asia-Pacific Conference on Applied Electromagnetics Proceedings, IEEE,* 2005.

[4] Y. J. Guo, A. Paez, R. A. Sadeghzedeh, and S. K. Barton, “A circular patch antenna for radio LANs,” *IEEE Transaction on Antenna and propagation*, pp. 177-178, 1997.

[5] E. M. Ibrahim, N. J. McEwan, R. A. Abd-Alhameed, and P. S. Excell, ”Dual-polarised uniplanar conical-beam antennas for hiperlan,” *Electronics Letter,* vol. 35, no. 1, pp. 2-4, 1999.

[6] T. W. Hee, P. S. Hall, and K. Y. Liew, “Wideband stacked Sierpinski carpet dipole antenna,” *IEEE Transaction on Antenna and propagation*, pp. 242-245, 2003.

[7] M. Naghshvarian-Jahromi and A. Falahati, “Classic minature fractal monopole antenna for UWB applications,” *ICTTA '08*, Syria, Damascus, April 2008.

[8] M. Naghshvarian-Jahromi and N. komjani, “Novel fractal monopole wideband antenna,” *Journal of Electromagnetic Wave Application,* JEMWA, vol. 22, no. 2, pp. 195-205, 2008.

[9] M. Naghshvarian-Jahromi, “Novel miniature semi-circular-semi-fractal monopole dual band antenna”, *Journal of Electromagnetic Wave Application,* JEMWA, vol. 22, no. 2, pp. 227-237, 2008.

[10] H. Jasik, *Antenna Engineering Handbook*. New York: McGraw-Hill, pp. 2.10-2.13, 1961.

Mahdi Naghshvarian Jahromi was born in Jahrom, Iranian 1985. He is student of final year the BS.c degree in Iran University of Science and Technology (IUST), Tehran, in, 2007-2008 in electrical engineering. He is author eight journal and two conference papers and He received the title of Head of UWB in Faramoj-Pajouh-engineering Company in 2007. He is scientific fields of interest is all about antennas, arrays, and microstrip filters.

Komjani, **Nader Barchloui,** was born in Tehran, iran, in 1965. He received the B.S. , M.S. and Ph.D. degress in Communication Engineering from Iran University of Science and Technology (IUST) in 1988, 1991 and 2000 respectively. From 1991 to 1994, he joined the Iranian Science Organization of Science and Technology (IROST), where he did research on microstrip large arrays antennas for radar receivers. His current research interests are in Phased Array Antennas, UWB and multiband microstrip antenna, Numerical methods in electromagnetic. Currently he is a assistant professor and the Director of the Antenna Laboratory in the Electrical Engineering Department, University of IUST at Iran.

Design of Elliptical Dielectric Resonator Antennas Using Genetic Algorithm and Rayleigh-Ritz Technique

[1]A. Tadjalli, [1]A. Sebak, [2]T. Denidni, and [3]I. Ahadi-Akhlaghi

[1] ECE Dept, Concordia University, Mntreal, QC, H3G 1M8, Canada
a_tadjal@ece.concordia.ca, abdo@ece.concordia.ca
[2] INRS-EMT, 800 de la Gauchetiere, Montreal, QC, H5A 1K6, Canada
[3] ECE Dept, Ferdowsi University, Mashhad, Iran

Abstract – In this paper, a specialized genetic algorithm (GA) combined with Rayleigh-Ritz method is used to obtain the dimensions of elliptical dielectric resonators (EDRs) for dual-band, wide-band, or circular polarization (CP) operation. Slot-coupled elliptical dielectric resonator antennas (EDRA's) and their characteristics are investigated. Parametric studies are presented to study the dependence of the return loss on the slot parameters. These parametric studies are used to optimize the slot dimensions and its position to excite given desired modes.

I. INTRODUCTION

Dielectric Resonators (DR's) have traditionally been used in many applications, such as microwave devices and antennas. Open dielectric resonators are potentially useful antenna elements [1]. Indeed, they offer several attractive features such as small size, high radiation efficiency [1-3], compatibility with MIC's, intrinsic mechanical simplicity, and the ability to obtain different radiation patterns using different modes. Many of the concepts used in the design of microstrip antennas can also be used in the design of dielectric resonator antennas. Dielectric resonator antennas (DRA's) have many similarities with microstrip antennas, such as small size, many possible shapes, lightweight, and ease of feeding with different excitation mechanisms. In addition, several modes can be excited, and each mode has different radiation characteristics. Dielectric resonator antennas have also some advantages over microstrip antennas, such as a wider bandwidth, higher radiation efficiency, wider range of dielectric materials, more geometrical parameters, and higher power capabilities. Systematic experimental investigations on dielectric resonator antennas (DRA's) have first been carried out by Long *et al*. [4-6]. Since then, theoretical and experimental investigations have been reported by many investigators on DRA's of various shapes such as spherical, cylindrical (or cylindrical ring), rectangular, etc. [7-14].

Generating dual-band operation, wide-band operation, and circular polarization (CP) using DRA's are other reasons of their attractiveness for antenna designers. Recently more attention has focused on the circularly polarized DRA's [10] since it allows a more flexible orientation for both the transmitter and receiver. Generation of CP requires two orthogonal modes in a phase-quadrature signal. Circular polarizations can be obtained using multiple feeds or by alternating the shape of conventional DRA's. The main advantage of single-feed circularly polarized DRA's is their simple structures that do not require an external polarizer.

The application of genetic algorithms (GA) has recently attracted the attention of researchers in the field of artificial intelligence. From the literature, it is clearly seen that genetic algorithms can provide powerful tools for optimization [15-19]. Genetic algorithms are used as parameter search techniques, which utilize genetic operators to find near optimal solutions. The advantage of a GA technique is that it is independent of the complexity of the performance index considered. It suffices to specify the objective function and to place finite bounds on the optimized parameters.

In this paper, we apply the Rayleigh-Ritz method [21], [22] combined with GA optimization to design EDRA's with desired characteristics and study the effect of different feed design parameters on their input impedance. A GA is used as a parameter search technique which utilizes the genetic operators to arrive at a design for a dual-band, wide-band, or CP EDRA. To this end, we combine the Rayleigh-Ritz method with GA optimization to reach appropriate dimensions of EDR's. To validate this technique, some examples are given and discussed in the following sections.

II. ANALYSIS OF EDR

In this section, the three-dimensional wave equation in elliptic cylinder coordinates is first expressed, and its solution for an EDR is then investigated. The geometry of EDR is shown in Fig. 1. The EDR is mounted on a ground plane with a and b are the semi-major and semi-minor axes, respectively, and h is the height of the EDR. Image theory can be immediately applied where the ground plane is replaced by an image portion of the cylinder extending to z = -h. For a DR with very large dielectric permittivity, the dielectric air interface can be approximated by a hypothetical perfect magnetic conductor (PMC), which requires that the tangential components of the magnetic field vanish on that surface. Rayleigh-Ritz procedure [21] is used in this section to find cut off frequencies of the structure elliptical cross-section field patterns of the DRA. In elliptical coordinates, the scalar Helmholtz equation can be written as,

$$\frac{2}{f_o^{\,2}(\cosh 2\xi - \cos 2\eta)}\left(\frac{\partial^2}{\partial \xi^2}+\frac{\partial^2}{\partial \eta^2}\right).\begin{Bmatrix} E_z \\ H_z \end{Bmatrix}+(k^2-k_z^2)\begin{Bmatrix} E_z \\ H_z \end{Bmatrix}=0 \tag{1}$$

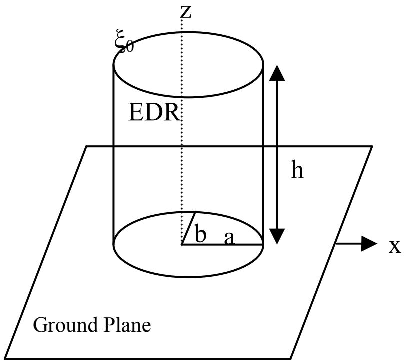

Fig. 1. Schematic diagrams of an EDR.

where f_o is the semi-focal distance of the ellipse. In order to find k_c ($\sqrt{k^2-k_z^2}$) and fields' modes, the Rayleigh-Ritz procedure [21] is employed by minimizing the energy functional of X ,

$$W(X)=\frac{1}{2}\iint_S\left[\left(\frac{\partial X}{\partial x}\right)^2+\left(\frac{\partial X}{\partial y}\right)^2\right]dxdy-\frac{k_c^2}{2}\iint_S X^2 dxdy \tag{2}$$

with

$$E_z \; or \; H_z = X.\begin{bmatrix} Sin(k_z z) \\ Cos(k_z z) \end{bmatrix},$$

where S is the EDRA cross section area. The two-dimensional field, X , may be expanded as a series of polynomials ϕ_i ,

$$X(x,y)=\sum_{i=1}^{m} C_i \phi_i \tag{3}$$

where C_i is constant and ϕ_i is polynomial to be determined later in this section. Therefore, the energy functional of X is,

$$W(X)=$$
$$\frac{1}{2}\iint_S [C]^T\left[\left(\frac{\partial\phi}{\partial x}\right)\left(\frac{\partial\phi}{\partial x}\right)^T+\left(\frac{\partial\phi}{\partial y}\right)\left(\frac{\partial\phi}{\partial y}\right)^T\right][C]dxdy$$
$$-\frac{k_c^{\,2}}{2}\iint_S [C]^T\,[\phi][\phi]^T\,[C]dxdy \tag{4}$$

where $[C]=[C_1 C_2 C_3 \dots C_m]$ and $[\phi]=[\phi_1\phi_2\phi_3\dots\phi_m]$.

Minimizing the energy functional, we obtain

$$[K][C]=k_c^2[M][C] \tag{5}$$

where the elements in the matrices K and M are given by

$$k_{i,j}=\iint_S\left(\frac{\partial\phi_i}{\partial x}\frac{\partial\phi_j}{\partial x}+\frac{\partial\phi_i}{\partial y}\frac{\partial\phi_j}{\partial y}\right)dxdy \tag{6}$$

and

$$m_{i,j}=\iint_S \phi_i\phi_j dxdy\ . \tag{7}$$

The i-*th* polynomial, ϕ_i , is defined in terms of a new polynomial $z_i(x,y)$. It is generated by the following procedure. Let $r=\lfloor\sqrt{(i-1)}\rfloor$, where the square brackets represent the integer portion of $t=(i-1)-r^2$. We define a parameter v such that,

$$v=t/2;\ 0\le v\le r\ ;\ z_i(x,y)=x^r y^v \quad \text{when t is even} \tag{8}$$

and

$$v=(t-1)/2\ ;\ 0\le v\le r-1\ ;\ z_i(x,y)=x^v y^r \quad \text{when t is odd} \tag{9}$$

The polynomial $z_i(x,y)$ has a degree of r + v and ϕ_i is defined as,

$$TM\ Case:\qquad \varphi_i(x,y)=z_i(x,y) \tag{10}$$

$$TE\ Case:\qquad \varphi_i(x,y)=\psi(x,y)z_i(x,y)\ . \tag{11}$$

where ψ is a constraint function for the elliptical cross-section and given by,

$$\psi=\frac{x^2}{a^2}+\frac{y^2}{b^2}-1 \tag{12}$$

ψ is added to satisfy the geometrical boundary conditions [21]. In equation (3), m depends on the order of X(x,y) and determines the overall accuracy and efficiency of the optimization process. By solving equation (5) for k_c and

$[C]$, we obtain solutions for E_z and H_z and hence other field components at any point in the resonator. Table 1 shows some resonant frequencies of an EDR and a circular cylindrical dielectric resonator (CDR) with the same height and same cross section area and for different eccentricity (e = f_o/a). As shown in the table 1, for the same range of frequency the number of resonant frequencies of EDR is more than the number of resonant frequencies of CDR with the same volume.

Table 1. Resonant frequencies of EDR and CDR with cross section area of 157mm^2 and height of 20 mm (same volume) and permittivity $\varepsilon_r = 12$.

Mode	e=f$_o$/a	Resonant Frequency (GHz)
TM110	0 (Circle)	3.748
TM111		4.840
TE010		6.051
TM210		6.494
TE011		6.781
TM112		7.547
TM211		8.046
TE012		8.144
TM113		8.260
TE013		8.809
Even TM110	0.866	3.371
Even TM210		5.188
Odd TM110		5.334
Even TE010		5.636
Odd TM210		6.756
Even TM111		6.990
Even TM310		7.132
Even TE110		7.234
Even TM211		8.026
Odd TM111		8.121
Even TE011		8.323
Odd TM310		8.339
Even TE020		8.990
Odd TM211		9.118
Even TM410		9.245
Even TM311		9.400
Even TE111		9.478
Even TM010		9.572
Odd TE110		9.684
Odd TM311		10.346

Figures 2 and 3 show field contours of the four lowest TM and TE modes for b/a=0.75, which are calculated using Rayleigh-Ritz method [21]. It is clear that we can obtain more excitation modes for an EDR case compared to a circular one, and also we can control priority order of modes frequencies by changing the axial ratio of the ellipse (a/b). Such field distribution patterns may be used to determine the feed location for a special modes excitation. Mode contour patterns can also be used to recognize paths on which electric or magnetic fields are zero. This allows the study of different EDR portions for different modes. For example, in Fig. 2© there are 2 paths with $H_z = 0$ with 3 portions of EDR for even TE$_{02P}$ mode. If wavenumbers of several modes are less than the cutoff wavenumber, then a feeding system can be design such that more than one mode are excited to potentially generate dual-band, circular polarized, or wide-band EDRAs.

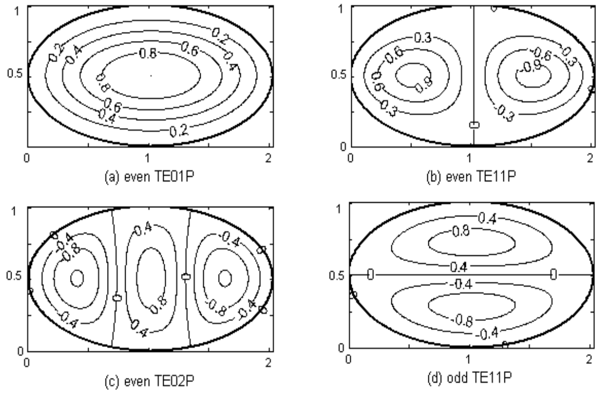
(a) even TE01P (b) even TE11P (c) even TE02P (d) odd TE11P

Fig. 2. H_z Field contour plot of TE modes.

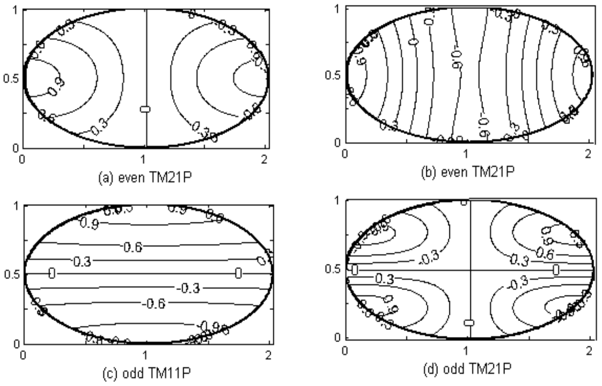
(a) even TM21P (b) even TM21P (c) odd TM11P (d) odd TM21P

Fig. 3. E_z Field contour plot of TM modes.

III. SYNTHESIS OF EDR FOR DESIRED MODES AT A GIVEN FREQUENCY

In short, Genetic Algorithms are search methods based on the principles and concepts of natural selection and evolution [22-25]. These optimization methods operate on a group of trial solutions in parallel, and they operate on the coding of the function parameters rather than the parameters directly. In a Genetic Algorithm, four operators are usually used: cross over, mutation, elitism and selection to make a new population from previous one. The single-point crossover, which is the simplest form and also the best in our case, was used in our algorithm. In this combination form, genetic information (bits) of two parent chromosomes which are chosen with probability P_x from the current population are exchanged from a random bit through their ends to form two new children. In order to perform a mutation operator, a chromosome is randomly chosen with probability P_m and one of its genes (bits) changes. Mutation is generally considered to be a background operator that ensures the probability of searching a particular subspace of the problem space, which is never zero. This has the effect of tending to inhibit the possibility of converging to a local optimum, rather than the global one. After crossover and mutation, the individual strings are selected according to their fitness to form a new generation. To ensure that the best individual of each population survives, we use elitism operator and transfer the fittest chromosome to the next generation. This process continues through subsequent generations and the average performance of individuals in a population is expected to increase, as good individuals are preserved and bred with one another and the less fit individuals die out. The GA used in this paper is terminated either when the fitness function of the best chromosome meets a predefined desired threshold or the number of generations exceeds a predefined maximum.

Resonant modes and frequencies of an EDRA are dependent on EDR dimensions, therefore dimensions of elliptical cross-section are the most important parameters to control resonant frequencies of an EDRA. In this study, the problem is defined in terms of choosing the geometric parameters a and b in such a way that the two elements of the eigenvector, obtained using Rayleigh-Ritz technique, have the desired values. To do this, first we define an appropriate encoding scheme that maps each set of feasible parameters to a bit stream. The encoding scheme is very simple: all parameters change to binary values. Using this encoding scheme, we randomly produce bit streams or chromosomes that make the first generation. In other words, each chromosome of this first population has the information of the parameters to be found. The next step is to apply the fitness function to each chromosome of the population. The fitness function for each chromosome is defined as the MSE difference between the eigenvector elements related to parameters obtained from that chromosome and the desired values of those eigenvector elements. Better individuals who have the higher fitness value have higher chances to survive according to the selection operator applied to the population. By applying cross over, mutation, elitism and selection operators to the population, the next generations are produced successively. The optimization process is shown step by step in Fig. 4. The seed chromosome is used to formulate a population of random chromosomes (parents) for simulation in the Rayleigh-Ritz procedure. The priority of primary modes can be approximately determined by the following formulas,

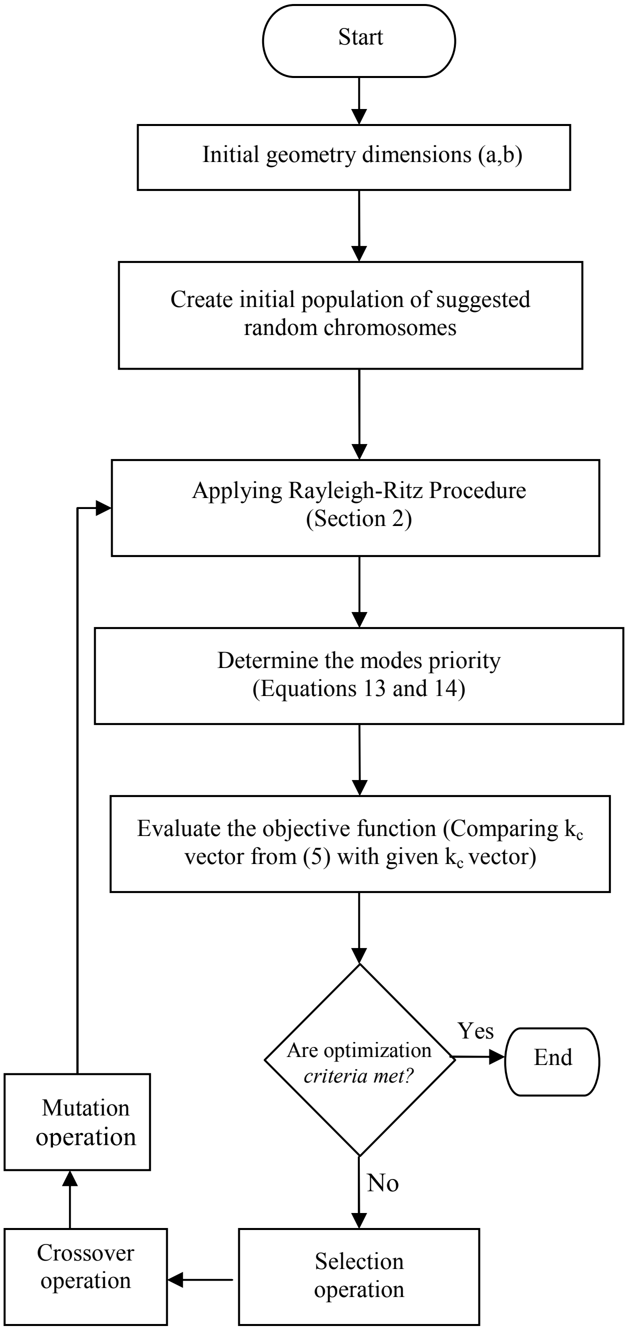

Fig. 4. Flowchart of Genetic Algorithm.

$$TE: \quad \left[\frac{(2m+1)}{2a}\right]^2 + \left[\frac{(2n+1)}{2b}\right]^2 \rightarrow P_{mn}^{TE} \qquad (13)$$

$$TM: \quad \left[\frac{m}{a}\right]^2 + \left[\frac{n}{b}\right]^2 \rightarrow P_{mn}^{TM} \; . \qquad (14)$$

where P_{mn}^{TE} and P_{mn}^{TM} are notations for the priority of the

TE and TM mnth modes, respectively. If the resonant frequency of one mode is smaller than the resonant frequency of another mode, then the priority of that mode is also smaller. For TE and TM modes, m and n, respectively, denote the number of contour lines valued zero in the contour plot in a (x) and b (y) directions (Figs. 2 and 3). The resulting mode frequencies for each geometry are obtained by the Rayleigh-Ritz procedure. If the GA converges on the target, the GA process is terminated. The selection operation determines the number of trials for which a particular chromosome (parent) is chosen for reproduction from the created population. The GA keeps looping by creating new generations until it converges to an optimum solution.

A population is created with a group of individuals created randomly in a define range. It can be seen from equations (13) and (14) for different values of a and b, the priority of primary modes changes. But this priority does not change for ranges of a and b which can be obtained by equations (13) and (14). If two best fitness of the population stock for 100 successive iterations and the objective function was not satisfied then we switch to another ranges of a and b with different priority of primary modes. The evaluation function (fitness) gives the individuals a score based on how well they perform at the given task. For the given ranges of a and b the objective vector and fitness function are defined as follow,

$$k_m = f_1 \text{ and } k_n = f_2 \Rightarrow Objective\ Vector = \begin{bmatrix} k_1 \\ \vdots \\ k_m = f_1 \\ \vdots \\ k_n = f_2 \\ \vdots \end{bmatrix} \quad (15)$$

$$EigenVector\ of\ an\ Individual = \begin{bmatrix} k_{10} \\ \vdots \\ k_{m0} \\ \vdots \\ k_{n0} \\ \vdots \end{bmatrix}$$

$$\Downarrow \qquad . \quad (16)$$

$$Fitness = (f_1 - k_{m0})^2 + (f_2 - k_{n0})^2$$

This continues until a suitable solution has been found or a certain number of generations have passed. In roulette wheel selection, individuals are given a probability of being selected that is directly proportionate to their fitness.

IV. APPLICATION OF GA TO DESIGN EDRA WITH GIVEN CHARACTERISTICS

Having control over excitation modes' frequencies gives us a flexibility to achieve certain design requirements or given characteristics. For example, an EDRA can be designed such that it has two desired resonant modes close to given frequencies to generate CP wave at those frequencies, and so on. Designing multi-band, wide-band or circularly polarized antennas is remarkably simple using this method. The previously described hybrid technique, i.e. GA and Rayleigh-Ritz procedure, is applied to EDRs. Figure 5 shows the geometry of an offset slot-coupled EDRA fed by microstrip line. The finite ground plane with an etched slot is located on the top of the surface of a substrate. To examine this issue, some examples to show different slot-coupled EDRAs are presented and discussed in the following sub-sections. Mode patterns presented in Figs. 2 and 3 lead us to locate the feeding system to excite two desired modes.

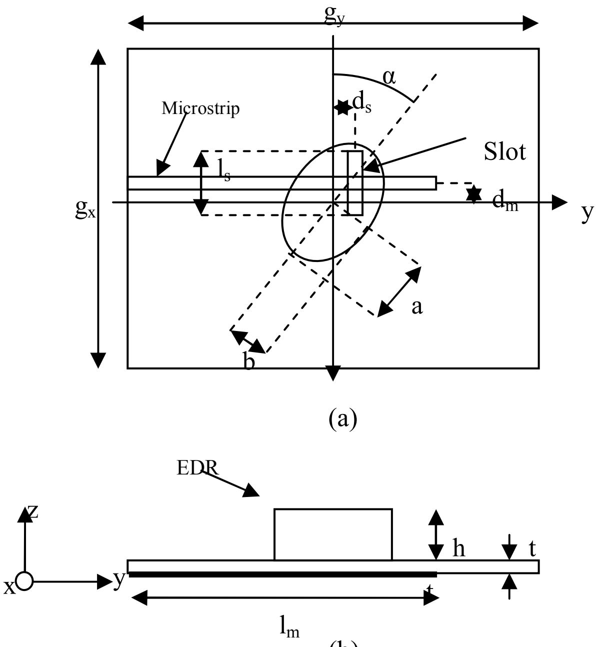

(a)

(b)

Fig. 5. Schematic diagrams of the proposed EDRA. (a) Top view. (b) Side view.

A. Dual-Band EDRA

Dual band operation of DRAs may be obtained by proper excitation of the DR. Consider an EDRA with a required dual-band operation at 2.5 and 4 GHz. The GA is applied in order to obtain a and b.

We set two different modes (for example here we chose odd TM_{210} and even TM_{310}) at 2.5GHz and 4GHz. To compensate for the PEC approximation to calculate fields of the EDRA, the size of the slot and its position with respect to the EDR can be tuned. We fixed the values of h=26mm, l_m=22mm, l_s=24mm, w_s=1.2mm, $\alpha=23^0$, $g_x=g_y$=80mm, t=1.5mm and obtained suitable DR dimensions based on GA: a=13.37mm, and b=16.49mm. Figure 6 illustrates the magnitude of the return loss of the offset slot-coupled EDRA. By applying GA, the simulated center frequencies are 2.48GHz and 4.03GHz. Ansoft-HFSS [27] simulations with optimizing size and position of slot, give mode resonant frequencies 2.51 and 4.00GHz, respectively. Figures 7 and 8 plot the simulated radiation patterns at 2.5 and 4GHz in the y-z and x-z planes. From these results, the patterns are similar to those radiated by a horizontal magnetic dipole at these two frequencies.

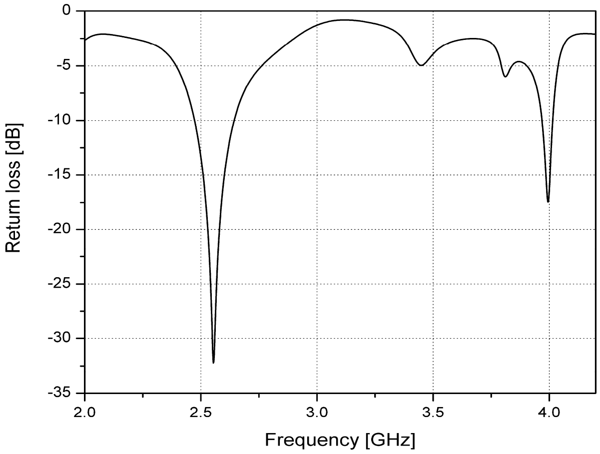

Fig. 6. Return Loss of the Designed Dual-Band EDRA.

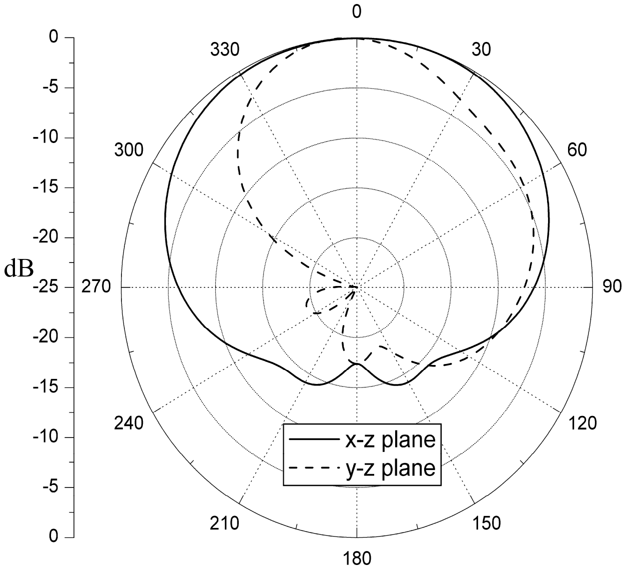

Fig. 7. Far Field Pattern of the EDRA at 2.5 GHz.

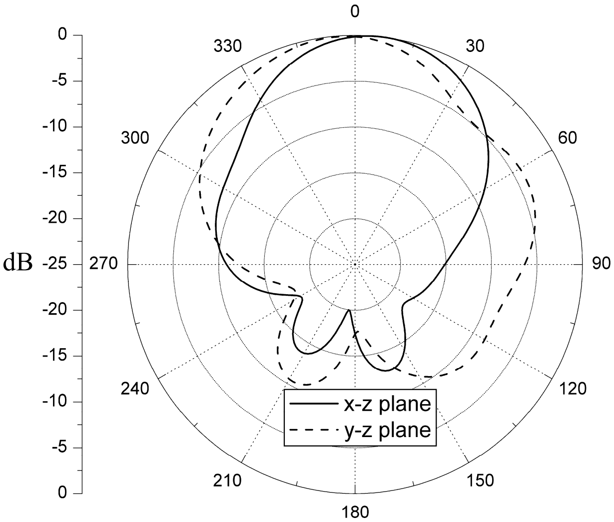

Fig. 8. Far Field Pattern of the EDRA at 4 GHz.

B. Wide-Band EDRA

In this example, we discuss the design of a wideband slot-fed EDRA at 2.9GHz. Using the proposed GA, the second and eighth modes were set at 2.7 and 3.1GHz, respectively. Varying the slot offset has some effect on the resonant frequencies of the excited modes. Figure 9 shows the simulated return loss as a function of frequency for an EDRA after GA and feed tuning were used. A bandwidth of 21.7% around 2.9GHz is achieved. The optimized parameters are h=30mm, l_m=25mm, l_s=18mm, w_s=1.5mm, $\alpha=17^0$, a=15.02mm, b=19.53mm, $g_x=g_y$=80mm, and t=1.5mm. The radiation patterns of the proposed antenna in both x-z and y-z planes were simulated at 2.70, 2.90, and 3.10 GHz, and are shown in Figs. 10 to 12. As shown in Figs. 10 to 12, variation of far field patterns is not too much over the band.

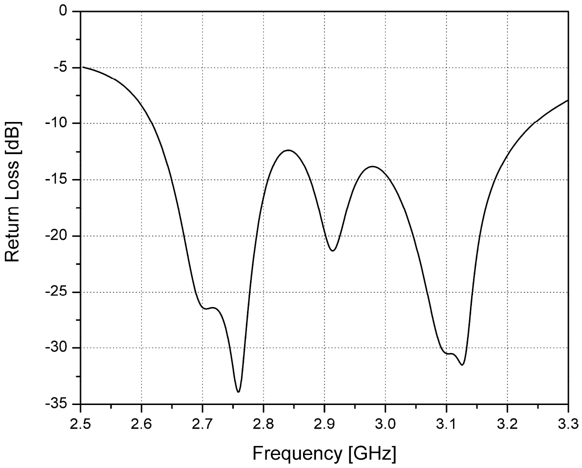

Fig. 9. Return Loss of the Designed Wide-Band EDRA

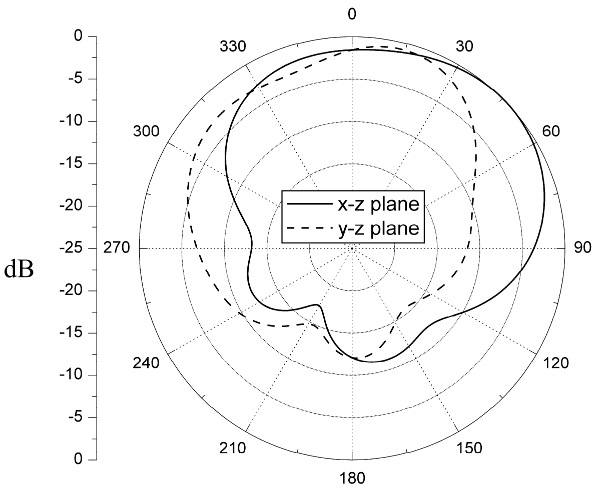

Fig. 10. Far Field Pattern of the EDRA at 2.7 GHz.

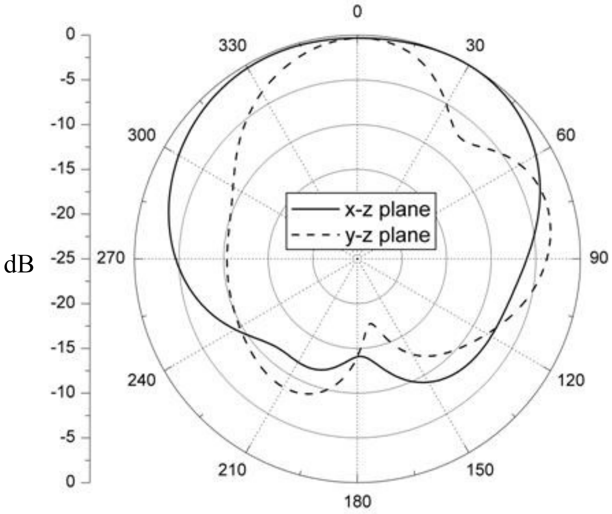

Fig. 11. Far Field Pattern of the EDRA at 2.9 GHz.

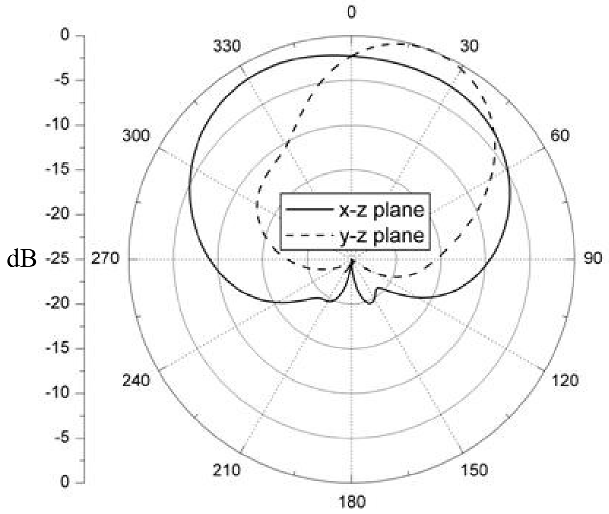

Fig. 12. Far Field Pattern of the EDRA at 3.1 GHz

C. Circularly Polarized EDRA

Recently, the circularly polarized (CP) DRA has received increasing attention because of its insensitivity to antenna orientation between the transmitter and receiver, which is very useful in satellite communications. Quadrature feeds and special DRAs have often been used for CP DRA design. However, the former increases the size and complexity of the feed network, whereas the latter is not easily available on the commercial market. Recently, most CP DRA work has concentrated on a single feed using normal DRAs. In this third example, we focus on the design of a CP DRA at 3 GHz. Applying GA, we set even TE_{020} mode at 2.95GHz and odd TE_{110} mode at 3.05GHz. Similar to the two previous sections, by tuning the slot size and its position, good results are obtained for an EDRA with h=29mm, l_m=25mm, l_s=18mm, w_s=1.5mm, $\alpha=15^0$, a=14.97mm, b=20.96mm, $g_x=g_y$=80mm, and t=1.5mm. Figure 13 shows the return loss versus frequency. Figure 14 shows the corresponding axial ratio (AR). From these results, it is observed that the -3dB AR bandwidth is 2.7%, which is reasonable for a single-fed CP EDRA. The simulated x-z and y-z plane radiation patterns at 3.03GHz are displayed in Fig. 15, where broadside field patterns are observed, as expected.

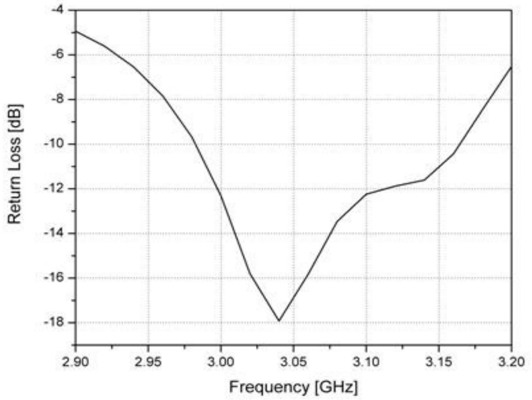

Fig. 13. Return Loss of the Designed Circular polarized EDRA.

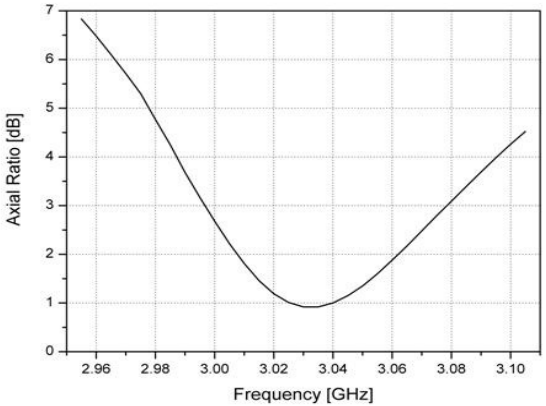

Fig. 14. Axial Ratio of The EDRA at $\theta=0^0$.

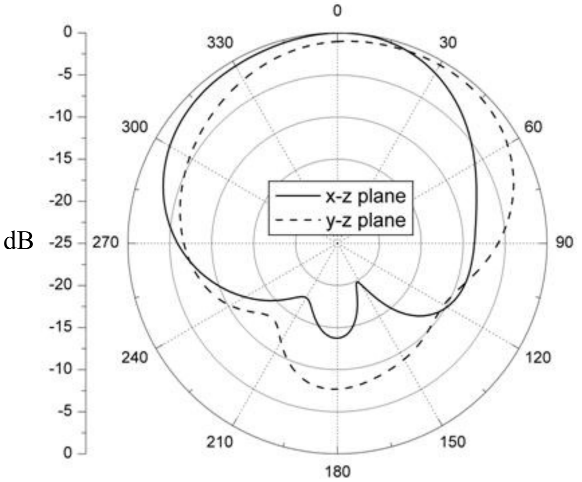

Fig. 15. Far Field Pattern of the EDRA at 3.03 GHz.

V. CONCLUSION

In this paper, a genetic algorithm has been introduced and presented for numerical optimization to obtain suitable dimensions of an EDRA with resonant modes at specified frequencies. The Rayleigh-Ritz method together with GA is used to calculate minor and major radii of the ellipse. Since each element of the calculated eigenvector using the Rayleigh-Ritz technique related to a mode frequency, we can require that a particular mode become excited at a certain frequency. Therefore, this technique is used to design EDRAs with desired characteristics. Examples are given to demonstrate the design of a dual band EDRA at two desired frequencies, and a wide band EDRA with 21.7% bandwidth at a given centered frequency. Also, an example is presented to show a single fed EDRA with two resonant modes close to each other to generate CP with 2.7% CP bandwidth. This paper illustrates that EDRA is a good candidate for a small antenna with wide range of given antenna characteristics including circular polarization, wide-band and dual-band operation.

REFERENCES

[1] R. K. Mongia and P. Bhartia, "Dielectric resonator antennas—A review and general design relations for resonant frequency and bandwidth," *Int. J. Microwave Millimeter-Wave Eng*., vol. 4, pp. 230–247, July 1994

[2] R. K. Mongia, A. Ittipiboon, and M. Cuhaci, "Measurement of radiation efficiency of dielectric resonator antennas," *IEEE Microwave Guided Wave Lett.,* vol. 4, pp. 80–82, Mar. 1994.

[3] A. Petosa, A. Ittipiboon, Y. M. M. Antar, D. Roscoe, and M. Cuhaci, "Recent advances in dielectric resonator antenna echnology*," IEEE Antennas Propagat. Mag*., vol. 40, pp. 35–48, June 1998..

[4] S. A. Long, M. McAllister, and L. C. Shen, "The resonant cylindrical cavity antenna," *IEEE Trans. Antennas Propagat*., vol. AP-31, pp. 406–412, May 1983.

[5] M. McAllister, S. A. Long, and G. L. Conway, "Rectangular dielectric resonator antenna," *Electron. Lett.*, vol. 19, pp. 219–220, Mar. 1983.

[6] M. Young, The Techincal Writers Handbook. Mill Valley, CA: University Science, 1989.

[7] M. McAllister and S. A. Long, "Resonant hemispherical dielectric antenna," *Electron. Lett.*, vol. 20, pp. 657–659, Aug. 1984.

[8] K. W. Leung, K. M. Luk, K. Y. A. Lai, and D. Lin, "Theory and experiment of a coaxial probe fed hemispherical dielectric resonator antenna," *IEEE Trans. Antennas Propagat.*, vol. 41, pp. 1390–1398, Oct. 1993.

[9] R. K. Mongia, A. Ittipiboon, P. Bhartia, and M. Cuhaci, "Electric monopole antenna using a dielectric ring resonator," *Electron. Lett.*, vol. 29, pp. 1530–1531, Aug. 1993.

[10] R. K. Mongia, A. Ittipiboon, M. Cuhaci, and D. Roscoe, "Circularly polarized dielectric resonator antenna," *Electron. Lett.*, vol. 30, pp. 1361–1362, Aug. 1994.

[11] Y. M. M. Antar and Z. Fan, "Characteristics of aperture coupled rectangular dielectric resonator antenna," *Electron. Lett.*, vol. 31, pp. 1209–1210, July 1995.

[12] S. M. Shum and K. M. Luk, "Analysis of aperture coupled rectangular dielectric resonator antenna," *Electron. Lett.*, vol. 30, pp. 1726–1727, Oct. 1994.

[13] T. B. Ng, Y. O. Yam, and M. L. Lam, "Active quarter-wavelength dielectric radiator with circularly polarized radiation pattern*," Electron. Lett*., vol. 27, pp. 1758–1759, 1991.

[14] G. D. Loos and Y. M. M. Antar, "A new aperture-coupled rectangular dielectric resonator antenna array*," Microwave Opt. Tech. Lett*., vol. 7, pp. 677–678, 1994.

[15] A. Tadjalli, A. R. Sebak, T. A. Denidni, A. A. Kishk, "Spheroidal dielectric resonator antenna," *URSI Digist, 2004 USNC/URSI National Radio Science Meeting*, p. 184, 2004

[16] R. Fletcher, Practical Methods of Optimization. Chichester, U.K.: Wiley Intersci., 1980.

[17] L. C. W. Dixon, Global Optima Without Convexity, in Design and Implementation of Optimization Software. Sijnoof Noordhof, The Netherlands: Aalphen aan den Rijn, 1978.

[18] L. Davis, Genetic Algorithms and Simulated Annealing. London, U.K.: Pittman, 1987.

[19] K. A. DeJong, An analysis of the behavior of a class of genetic adaptive systems, Ph.D. dissertation, Univ. Michigan, 1975.

[20] D. E. Goldberg, Genetic Algorithms in Search, Optimization and Machine Learning. Reading, MA: Addison–Wesley, 1989.

[21] A. Tadjalli, A. R. Sebak and T. Denidni, "Elliptical Cylinder Dielectric Resonator Antenna," *ANTEM International Symposium*, Ottawa, Aug. 2004

[22] B. Singh and D. K. Tyagi, "Transverse vibrations of an elliptic plate with variable thickness," *J. Sound Vib.*, vol. 99, no. 3, pp. 370- 391, 1985.

[23] R. L. Haupt, "An Introduction to Genetic Algorithms for Electromagnetics*," IEEE Antennas and Propagation Magazine*, vol. 37, no. 2, pp. 7-15, April 1995.

[24] J. M. Johnson, Y. Rahat-Samii, "Genetic Algorithms in Engineering Electromagnetics," *IEEE Antennas and Propagation Magazine*, vol. 39, no. 4, pp. 7-21, Aug. 1997.

[25] J. M. Johnson, Y. Rahat-Samii, "Genetic Algorithm Optimization and its Application to Antenna Design," *IEEE Antennas and Propagation Society International Symposium Digest*, vol. 1, pp. 326-329, Jun 1994.

[26] B. Orchard, "Optimising Algorithms for Antenna Design," MSc Dissertation, University of the Witwatersrand, 2002.

[27] Ansoft HFSS v.9.2.1, Ansoft Corporation, Pittsburgh, PA 15219-1119, USA.

A Closed-Form Rational Model of Coupled Right/Left-Handed Ladder Networks for New Microwave Circuits Design

G. Antonini

Dipartimento di Ingegneria Elettrica e dell’Informazione
Università degli Studi dell’Aquila
Monteluco di Roio, 67040, L’Aquila, Italy
antonini@ing.univaq.it

***Abstract* –** The analytical characterization of coupled composite righ/left-handed ladder networks is presented. Relying on closed-form polynomials, the two-port representation of the composite right/left-handed ladder network is obtained in a rational form, leading to identify its poles and residues and, thus, the state-space macromodel of the network. The proposed macromodel is successfully validated by comparing the numerical results with those obtained using conventional frequency domain techniques of finite periodic structures.

Keywords: Metamaterials, composite righ/left-handed ladder networks, transient analysis, rational macromodeling.

I. INTRODUCTION

Over 30 years ago Veselago [1] theoretically investigated materials with simultaneously negative permittivity and permeability, or left-handed (LH) materials. Recently a transmission line approach of left-handed (LH) materials has been presented in [2, 3] where an equivalent circuit for a left-handed transmission line (LH-TL) is proposed. Such equivalent circuit has been also extended to composite right/left handed (CRLH) metamaterials in [4].

The low insertion loss and broad bandwidth of the LH-TL make it an efficient candidate for microwave frequencies. Due to their negative propagation constant, LH-TLs exhibit phase advance instead of a phase delay as the conventional right-handed transmission lines. This characteristic leads to new designs for many microwave circuits, antennas and couplers.

Artificial CRLH structures are periodic networks whose unit cell consists of a conventional transmission line which is electrically short and loaded with series and shunt elements such that it exhibits a CRLH behavior. Typically the transmission line is loaded by longitudinal (interdigital) capacitances and transverse (short-stub) inductances. As a consequence, the analysis of such type of structures requires modeling either the continuous nature of the transmission line or the discrete behavior of lumped elements. In [5] this task is carried out by solving the Telegrapher’s equations for a continuous transmission line problem.

As long as the spatial period of loading lumped elements is electrically short, the resulting structure can be regarded as a finite periodic half-T ladder network (HTLN) which is the best candidate to model composite right/left handed structures.

HTLNs have been widely used in transmission lines modeling [6] under the hypothesis that electrically small sections of length $\Delta\ell$ are assumed ($\Delta\ell \ll \lambda_g$, λ_g being the guided wavelength [3]). In the case of artificial CRLH structures obtained by periodically loading transmission lines or by cascading lumped elements, half-T ladder networks represent their exact model [7, 8].

While a great attention has been devoted to frequency-domain analysis of composite right/left handed structures [3, 9], their time-domain analysis is a relatively new issue. The fact that transient analysis provides information about the system response over many frequencies, makes it attractive to investigate metamaterials properties in a fast and efficient way. In addition, non-linear terminations call for time-domain macromodels.

Time-domain transmission line matrix (TLM) modeling of metamaterials with negative refractive index has been derived in [10]. A composite right/left-handed equivalent circuit FDTD method is presented in [11] and applied to investigate several transient and refractive phenomena occurring at the interface between a CRLH metamaterial and a purely right-handed (PRH) structure. More recently, a stability analysis of 1-D double negative transmission lines is presented in [5] where a method of moments (MOM) [12] approach is employed to perform time-domain computations.

In [13] a systematic approach to composite righ/left-handed ladder networks (CRLH-LNs) has been presented. The aim of this work is to extend such a methodology to coupled composite righ/left-handed ladder networks. Metamaterial coupled-line couplers have the advantage of providing arbitrary coupling level in addition to the broad bandwidth of conventional coupled-line couplers. A comprehensive frequency-domain analysis of this type of structures is presented in [14] where mechanisms of coupling are derived in the framework of generalized transmission lines.

Based on the ladder structure of the system, a rigorous analysis of coupled CRLH-LNs is developed, which is based on closed-form polynomials, leading to a rational macromodel of the transfer functions of the system. In the recent years new and effective techniques have been developed to generate macromodels from frequency-domain response of electromagnetic systems [15–17]. CRLH-LN structures can be regarded as periodic and finite; as a consequence, any electrical quantities of the CRLH-LNs, such as voltages and currents, can always be expressed in a rational form due to the RLCG nature of the network. This target is achieved by using closed-form polynomials depending on the cell matrix $\boldsymbol{K}(s) = \boldsymbol{Y}_2(s)\boldsymbol{Z}_1(s)$ of the ladder network. Polynomial coefficients are *a-priori* analytically computed and stored. The resulting rational macromodel is the exact representation of the CRLH-LN and can be used for both time and frequency-domain analysis of coupled CRLH-LNs.

The paper is organized as follows: Section II presents the polynomial model of CRLH ladder networks leading to a rational multiport representations of coupled CRLH-LNs, described in Section III, which is suitable for an efficient computation of poles/residues and, thus, for a time-domain macromodel. Section IV presents the computation of the dispersion diagram and a comparison with that of CRLH-TLs. Numerical tests are carried out and reported in Section V. The conclusions are drawn in Section VI.

II. POLYNOMIAL MODEL OF CRLH-LNS

Composite right/left handed transmission lines can be modeled as the cascade of n elementary identical half-T cells, as shown in Fig. 1, characterized by both longitudinal and transversal inductances and capacitances [4]. In addition, longitudinal resistances and transverse conductances are added to take the ever existing losses into account.

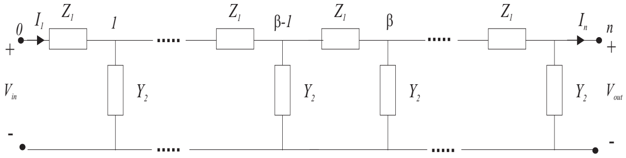

Fig. 1. Half-T ladder network.

The resulting structure is a *high-pass* filter mimicking a composite right/left handed transmission line. The equivalent circuit shown in Fig. 2 represents a possible model of a cell although other topologies can be considered [2].

The transmission line model can still be adopted under the hypothesis that the unit cell is electrically small [2, 18], but a rigorous analysis of practical realizations of CRLH structures is desirable and useful to designers. The main difference with respect to the continuous transmission line model relies on the fact that the half-T ladder network is a periodic structure which is characterized by having any transfer function to be written as rational function. Obviously, standard multiport network theory can be used to analyze the ladder network in the frequency domain [19] but such an approach is not suitable to provide a time-domain macromodel.

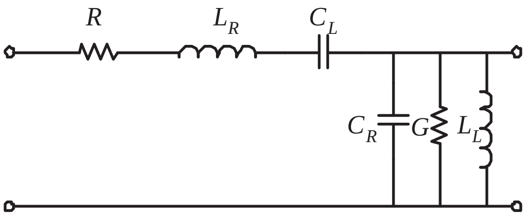

Fig. 2. Elementary half-T cell for a composite right/left handed ladder network (CRLH-LN).

To the aim to develop the closed-form macromodel of a CRLH-LN, is useful to define the unit cell impedance and admittance in the Laplace domain,

$$\begin{aligned} Z_1(s) &= R + sL_R + \frac{1}{sC_L} = \frac{s^2 L_R C_L + sRC_L + 1}{sC_L} \\ Y_2(s) &= G + sC_R + \frac{1}{sL_L} = \frac{s^2 L_L C_R + sGL_L + 1}{sL_L}, \end{aligned} \tag{1a}$$

which are rational functions.

In [20] it is shown that, in the hypothesis of a uniform, linear and time invariant HTLN, the voltage at the generic node β in the Laplace-domain can be expressed as,

$$V_\beta(s) = \frac{P_b^{n-\beta}(K(s))}{P_b^n(K(s))} V_{in}(s) \tag{2}$$

where the cell factor $K(s)$ is,

$$K(s) = Y_2(s) Z_1(s) \tag{3}$$

and

$$P_b^{n-\beta}(K(s)) = \sum_{j=0}^{n-\beta} b_{j,n-\beta} K^j(s) \tag{4}$$

is a polynomial in $K(s)$, of order $n-\beta$ with $0 \le \beta \le n$. Polynomial coefficients b are generated as [21],

$$b_{i,j} = \begin{pmatrix} i+j \\ j-i \end{pmatrix} = \begin{pmatrix} i+j \\ 2j \end{pmatrix} \tag{5}$$

which leads to the generation of the following triangle known as DFF triangle [20], shown in Table II.

The general expression of the longitudinal branch current $I_{\beta 1}(s)$ is,

$$I_{\beta 1}(s) = \frac{1}{Z_1(s)} \frac{P_c^{n-\beta+1}(K(s))}{P_b^n(K(s))} V_{in}(s) \tag{6}$$

Table 1. DFF triangle.

i^j	0	1	2	3	4
0	1				
1	1	1			
2	1	3	1		
3	1	6	5	1	
4	1	10	15	7	1
...	....				

where the corresponding roots are,

$$P_c^{n-\beta+1}\left(K(s)\right) = \sum_{j=0}^{n-\beta+1} c_{j,n-\beta+1} K^{j+1}\left(s\right) \tag{7}$$

is a polynomial in $K\left(s\right)$ of order $n-\beta+1$ and the coefficients c are obtained as [21],

$$c_{i,j} = \left(\begin{array}{c} i+j+1 \\ j-i \end{array}\right) = \left(\begin{array}{c} i+j+1 \\ 2j+1 \end{array}\right) \tag{8}$$

leading to the triangle known as DFFz triangle [20], shown in Table II.

Table 2. DFFz triangle.

i^j	0	1	2	3	4
0	1				
1	1	1			
2	1	3	1		
3	1	6	5	1	
4	1	10	15	7	1
...	....				

It is worth noticing that polynomials $P_b^n(K(s))$ and $P_c^n(K(s))$ allow to describe any kind of finite periodic structure, provided the cell factor $K(s)$ is given. In particular it can be used to model CRLN-LNs.

III. COUPLED CRLN-LNS

As stated before, no assumption is done either on the cell factor $K(s)$ as for the nature of longitudinal impedance $\boldsymbol{Z}_1(s)$ and transverse admittance $\boldsymbol{Y}_2(s)$ or its dimension; hence, the extension to the multidimensional case is straightforward. To this aim, let us consider N coupled CRLH-LNs (Fig. 3 shows an example with $N=2$) and define the longitudinal impedance and transverse admittance matrices as,

$$\boldsymbol{Z}_1\left(s\right) = \boldsymbol{R} + s\boldsymbol{L}_R + \frac{1}{s}\boldsymbol{C}_L^{-1} \tag{9a}$$

$$\boldsymbol{Y}_2\left(s\right) = \boldsymbol{G} + s\boldsymbol{C_R} + \frac{1}{s}\boldsymbol{L}_L^{-1}, \tag{9b}$$

where $\boldsymbol{R}$ and $\boldsymbol{G}$ are diagonal matrices containing the resistance and conductance of each half-T cell, $\boldsymbol{L}_R$ and $\boldsymbol{C}_R$ are the right-handed inductance and capacitance matrices and $\boldsymbol{L}_L$ and $\boldsymbol{C}_L$ are the left-handed inductance and capacitance matrices, respectively. These latter are diagonal matrices.

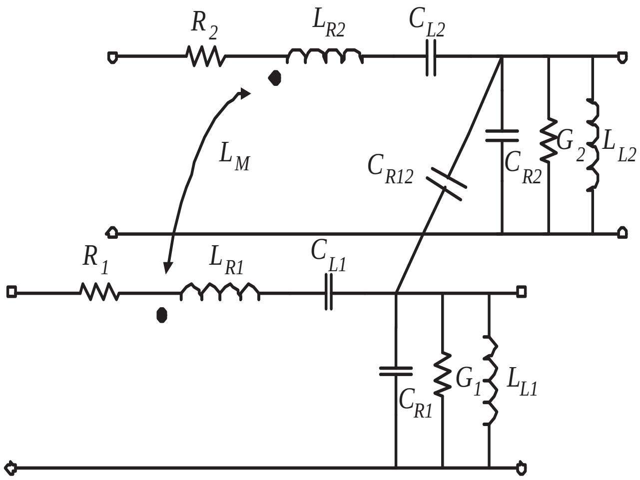

Fig. 3. Elementary half-T cell for a coupled composite right/left handed ladder network (CRLH-LN).

In the multidimensional case, the cell factor $\boldsymbol{K}(s)$ becomes a matrix and can be defined as,

$$\boldsymbol{K}\left(s\right) = \boldsymbol{Y}_2\left(s\right)\boldsymbol{Z}_1\left(s\right). \tag{10}$$

The polynomials $P_b^n(K(s))$ and $P_c^n(K(s))$ become polynomial matrices,

$$P_b^n\left(\boldsymbol{K}(s)\right) = \sum_{j=0}^{n} b_{j,n}\boldsymbol{K}^j\left(s\right) \tag{11a}$$

$$P_c^n\left(\boldsymbol{K}(s)\right) = \sum_{j=0}^{n} c_{j,n}\boldsymbol{K}^{j+1}\left(s\right). \tag{11b}$$

When general terminal conditions need to be considered, the chain parameters [6] of the half-T ladder network can be obtained as,

$$\boldsymbol{\Phi}_{11}(s) = \sum_{j=0}^{n-1} b_{j,n-1}\boldsymbol{K}^j(s) = P_b^{n-1}\left(\boldsymbol{K}(s)\right), \tag{12a}$$

$$\begin{aligned}\boldsymbol{\Phi}_{12}(s) &= -\left(\sum_{j=0}^{n} c_{j,n}\boldsymbol{K}^{j+1}(s)\right)\cdot\boldsymbol{Y}_2^{-1}(s) \\ &= -P_c^n\left(\boldsymbol{K}(s)\right)\cdot\boldsymbol{Y}_2^{-1}(s),\end{aligned} \tag{12b}$$

$$\begin{aligned}\boldsymbol{\Phi}_{21}(s) &= -\left(\sum_{j=0}^{n} c_{j,n}\boldsymbol{K}^{j+1}(s)\right)\cdot\boldsymbol{Z}_1^{-1}(s) \\ &= -P_c^n\left(\boldsymbol{K}(s)\right)\cdot\boldsymbol{Z}_1^{-1}(s),\end{aligned} \tag{12c}$$

$$\boldsymbol{\Phi}_{22}(s) = \sum_{j=0}^{n} b_{j,n}\boldsymbol{K}^j(s) = P_b^n\left(\boldsymbol{K}(s)\right). \tag{12d}$$

Polynomials $P_b^{n-1}\left(\boldsymbol{K}(s)\right)$ and $P_c^n\left(\boldsymbol{K}(s)\right)$ can be factored into zero-pole pairs. Their factorization is accomplished by using the poles given by the expressions presented in [21],

$$P_b^{n-1}\left(\boldsymbol{K}(s)\right)=\prod_{j=1}^{n-1}\left(\boldsymbol{K}(s)-u_{j,n-1}\boldsymbol{U}_N\right) \tag{13a}$$

$$P_c^{n}\left(\boldsymbol{K}(s)\right)=\prod_{j=1}^{n-1}\left(\boldsymbol{K}(s)-v_{j,n-1}\boldsymbol{U}_N\right)\cdot\boldsymbol{K}(s), \tag{13b}$$

where $\boldsymbol{U}_N$ is the identity matrix of order N and polynomial roots $u_{j,n}$ and $v_{j,n}$ can be computed analytically as,

$$u_{j,n} = -4\sin^2\left[\frac{(2j-1)}{(2n+1)}\frac{\pi}{2}\right] \tag{14a}$$

$$v_{j,n} = -4\sin^2\left[\frac{j}{(n+1)}\frac{\pi}{2}\right], \tag{14b}$$

for $j=1\cdots n$.

The knowledge of the chain parameters Φ allows to obtain the rational form of any other two port matrix representation. The $\boldsymbol{Z}(s)$ matrix entries can be evaluated in terms of $P_b^n\left(\boldsymbol{K}(s)\right)$ and $P_c^n\left(\boldsymbol{K}(s)\right)$ polynomials as,

$$\boldsymbol{Z}_{11}(s) = P_b^n\left(\boldsymbol{K}(s)\right)\cdot\left(P_c^n\left(\boldsymbol{K}(s)\right)\cdot\boldsymbol{Z}_1^{-1}(s)\right]^{-1} \tag{15a}$$

$$\boldsymbol{Z}_{12}(s) = -\left(P_c^n\left(\boldsymbol{K}(s)\right)\cdot\boldsymbol{Z}_1^{-1}(s)\right)^{-1}, \tag{15b}$$

$$\boldsymbol{Z}_{21}(s) = -\left(P_c^n\left(\boldsymbol{K}(s)\right)\cdot\boldsymbol{Z}_1^{-1}(s)\right)^{-1}, \tag{15c}$$

$$\boldsymbol{Z}_{22}(s) = P_b^{n-1}\left(\boldsymbol{K}(s)\right)\cdot\left(P_c^n\left(\boldsymbol{K}(s)\right)\boldsymbol{Z}_1(s)^{-1}\cdot\right]^{-1}. \tag{15d}$$

The previous expressions (15a)- (15d), taking into account that $\boldsymbol{K}(s)\cdot\boldsymbol{Y}_2^{-1}(s)=\boldsymbol{Z}_1\left(s\right)$, can be factored in the following way,

$$\begin{aligned}\boldsymbol{Z}_{11}(s) &= \prod_{j=1}^{n}\left(\boldsymbol{K}\left(s\right)-u_{j,n-1}\boldsymbol{U}_N\right)\\ &\cdot\left[\prod_{j=1}^{n-1}\left(\boldsymbol{K}\left(s\right)-v_{j,n-1}\boldsymbol{U}_N\right)\cdot\boldsymbol{Y}_2\left(s\right)\right]^{-1} \end{aligned}\tag{16a}$$

$$\begin{aligned}\boldsymbol{Z}_{21}(s) &= \boldsymbol{Z}_{12}\\ &= -\left[\prod_{j=1}^{n-1}\left(\boldsymbol{K}\left(s\right)-v_{j,n-1}\right)\cdot\boldsymbol{Y}_2\left(s\right)\right]^{-1}\end{aligned} \tag{16b}$$

$$\begin{aligned}\boldsymbol{Z}_{22}(s) &= \prod_{j=1}^{n-1}\left(\boldsymbol{K}\left(s\right)-u_{j,n-1}\boldsymbol{U}_N\right)\\ &\cdot\left[\prod_{j=1}^{n-1}\left(\boldsymbol{K}\left(s\right)-v_{j,n-1}\boldsymbol{U}_N\right)\cdot\boldsymbol{Y}_2\left(s\right)\right]^{-1}\end{aligned} \tag{16c}$$

The poles of the open-ended CRLH-LN are obtained as the zeros of the following equation,

$$\mathcal{P}(s)=\det\left[\prod_{j=1}^{n-1}\left(\boldsymbol{K}\left(s\right)-v_{j,n-1}\boldsymbol{U}_N\right)\cdot\boldsymbol{Y}_2\left(s\right)\right]=0 \tag{17}$$

which can be rewritten as,

$$\prod_{j=1}^{n-1}\det\Big[\boldsymbol{K}\left(s\right)-v_{j,n-1}\boldsymbol{U}_N\Big]\cdot\det\Big[\boldsymbol{Y}_2\left(s\right)\Big]=0. \tag{18}$$

The poles of the CRLH-LN can be identified as,

1) the roots of polynomial,

$$\det\Big[\boldsymbol{Y}_2\left(s\right)\Big]. \tag{19}$$

2) the roots of polynomials,

$$\det\Big[\boldsymbol{Y}_2\left(s\right)\boldsymbol{Z}_1\left(s\right)-v_{j,n-1}\boldsymbol{U}_N\Big],\quad j=1\cdots n-1. \tag{20}$$

Residues of the i-th pole can be obtained as,

$$\begin{aligned}&\boldsymbol{R}_{11,i} =\\ &\prod_{j=1}^{n}\left(\boldsymbol{K}(s)-u_{j,n-1}\boldsymbol{U}_{\boldsymbol{N}}\right)\cdot\left(s-p_i\right)\big|_{s=p_i}\\ &\cdot\text{adj}\left[\prod_{j=1}^{n-1}\left(\boldsymbol{K}(s)-v_{j,n-1}\boldsymbol{U}_{\boldsymbol{N}}\right)\boldsymbol{Y}_2(s)\right]/\mathcal{P}(s)\end{aligned} \tag{21}$$

$$\begin{aligned}&\boldsymbol{R}_{12,i} =\\ &-\text{adj}\left[\left(\prod_{j=1}^{n-1}\left(\boldsymbol{K}(s)-v_{j,n-1}\boldsymbol{U}\right)\right)\boldsymbol{Y}_2(s)\right]/\mathcal{P}(s)\\ &\cdot\left(s-p_i\right)\big|_{s=p_i},\end{aligned} \tag{22}$$

$$\begin{aligned}&\boldsymbol{R}_{21,i} =\\ &\text{adj}\left[\left(\prod_{j=1}^{n-1}\left(\boldsymbol{K}(s)-v_{j,n-1}\boldsymbol{U}\right)\right)\boldsymbol{Y}_2(s)\right]/\mathcal{P}(s)\\ &\cdot\left(s-p_i\right)\big|_{s=p_i},\end{aligned} \tag{23}$$

$$\begin{aligned}&\boldsymbol{R}_{22,i} =\\ &\prod_{j=1}^{n-1}\left(\boldsymbol{K}(s)-u_{j,n-1}\boldsymbol{U}_{\boldsymbol{N}}\right)\cdot\left(s-p_i\right)\big|_{s=p_i}\\ &\cdot\text{adj}\left[\prod_{j=1}^{n-1}\left(\boldsymbol{K}(s)-v_{j,n-1}\boldsymbol{U}_{\boldsymbol{N}}\right)\boldsymbol{Y}_2(s)\right]/\mathcal{P}(s),\end{aligned} \tag{24}$$

for $i=1\cdots P_Z$, being P_Z the total number of poles of the $\boldsymbol{Z}$ matrix entries and adj indicates the adjugate operator. The reciprocity of the LN guarantees that matrices $\boldsymbol{R}_{21,i}=\boldsymbol{R}_{12,i}$.

A. Remarks

If we consider two identical coupled HTLNs some observations can be addressed when computing poles of equation (20). In fact, in this case, the diagonal elements of all matrices are identical and exists a unique nonsingular transformation which diagonalizes both matrices $\boldsymbol{L}_R$ and $\boldsymbol{C}_R$. As stated before, matrices $\boldsymbol{R},\boldsymbol{G},\boldsymbol{C}_L$ and $\boldsymbol{L}_L$ are already diagonal. The transformation is,

$$\boldsymbol{T}=\frac{1}{\sqrt{2}}\begin{bmatrix}1 & 1\\ 1 & -1\end{bmatrix}. \tag{25}$$

Hence, multiplying the original matrix $\boldsymbol{Y}_2(s)\,\boldsymbol{Z}_1(s)$ in equation (20) on the left by $\boldsymbol{T}^{-1}$ and on the right by $\boldsymbol{T}$, the determinant remains the same since $\boldsymbol{T}$ is nonsingular and can be written as,

$$\det\Big[\boldsymbol{T}^{-1}\boldsymbol{Y}_2(s)\,\boldsymbol{Z}_1(s)\,\boldsymbol{T} - v_{j,n-1}\boldsymbol{U}_2\Big] = \tag{26}$$

$$\det\Big[\left(\boldsymbol{R} + \boldsymbol{T}^{-1}\boldsymbol{L}_R\boldsymbol{T} + \frac{1}{s}\boldsymbol{C}_L^{-1}\right) \tag{27}$$

$$\cdot\left(\boldsymbol{G} + \boldsymbol{T}^{-1}\boldsymbol{C}_R\boldsymbol{T} + \frac{1}{s}\boldsymbol{L}_L^{-1}\right) - v_{j,n-1}\boldsymbol{U}_2\Big].$$

From equation (26), it is worth noticing that poles of equation (20) can be computed as the roots of two quartic equations,

$$\det\left[\tilde{Z}_{1c}\tilde{Y}_{2c} - v_{j,n-1}\right] = 0 \tag{28a}$$

$$\det\left[\tilde{Z}_{1d}\tilde{Y}_{2d} - v_{j,n-1}\right] = 0, \tag{28b}$$

where

$$\tilde{Z}_{1c} = R + s\left(L_R + L_M\right) + \frac{1}{s}C_L^{-1}, \tag{29a}$$

$$\tilde{Y}_{2c} = G + s\left(C_R + C_M\right) + \frac{1}{s}L_L^{-1}, \tag{29b}$$

$$\tilde{Z}_{1d} = R + s\left(L_R - L_M\right) + \frac{1}{s}C_L^{-1}, \tag{29c}$$

$$\tilde{Y}_{2d} = G + s\left(C_R - C_M\right) + \frac{1}{s}L_L^{-1}, \tag{29d}$$

and L_R, L_M represents the self and mutual inductance of the lines, C_R, C_M represents the self and mutual capacitance of the lines, respectively.

Hence, the poles of the coupled CRLH-LN can be computed by solving two quartic algebraic equations corresponding to two separate CRLH-LNs, characterized by common and differential mode right-handed parameters. The quartic equations (28) can be analytically solved using the method described in [22]. Since the system is physically stable, the exact solution of equations (28) ensures the stability of both the decoupled and coupled CRLH-LNs because the transformation (25) is purely real.

It is also to be pointed out that the proposed method is general as far as the topology and nature of impedance $\boldsymbol{Z}_1$ and admittance $\boldsymbol{Y}_2$ which can be eventually dispersive.

In [8] an equivalent circuit is used to model double-negative metamaterial lenses; recursive relations are provided giving the node voltages and branch currents and the link with the Fibonacci problem is pointed out. The proposed method completely exploits the polynomial nature of the problem, leading to closed-form models of CRLH-LNs. The polynomial coefficients reduce to Fibonacci's numbers when $\boldsymbol{Z}_1(s) = \boldsymbol{Y}_2(s)^{-1}$ so that $\boldsymbol{K}(s) = \boldsymbol{I}_N$ [20].

B. Rational macromodel

The explicit knowledge of poles and residues allow to select the dominant poles according to the frequency range of interest; among the selected poles, only those whose residues significantly impact the frequency response are retained. This two-step process leads to generate a reduced order model of the CRLH-LN.

The poles-residues representation of the impedance matrix $\boldsymbol{Z}$ allows to generate a macromodel in the state-space form, leading to a set of first order differential equations which reads,

$$\begin{aligned}\frac{d}{dt}\mathbf{x}(t) &= \mathcal{A}\mathbf{x}(t) + \mathcal{B}\mathbf{u}(t)\\ \mathbf{y}(t) &= \mathcal{C}\mathbf{x}(t) + \mathcal{D}\mathbf{u}(t),\end{aligned} \tag{30}$$

where $\mathcal{A} \in \mathrm{R}^{p\times p}$, $\mathcal{B} \in \mathrm{R}^{p\times q}$, $\mathcal{C} \in \mathrm{R}^{q\times p}$, $\mathcal{D} \in \mathrm{R}^{q\times q}$, p is the number of states and q is the number of ports. Since the impedance matrix representation is used, the input and the output vectors, $\mathbf{u}(t)$ and $\mathbf{y}(t)$ respectively, correspond to port currents $\boldsymbol{i}(t)$ and voltages $\boldsymbol{v}(t)$, respectively. The set of first order differential equations (30) are completed with the terminal conditions and solved numerically.

It is to be remarked that the proposed macromodeling methodology can be used for longitudinal impedance $\boldsymbol{Z}_1(s)$ and transverse admittance $\boldsymbol{Y}_2(s)$ different from the series ones of equations (9a) and (9b) (e.g. see [2]).

IV. DISPERSION RELATION OF THE PERIODIC CRLH-LN

The dispersion relation of a CRLH-LN is obtained by applying periodic boundary conditions to the unit cell represented by its $ABCD$ matrix. As a consequence, the output voltages and currents are related to the input voltages and currents by the propagation term $e^{-\gamma\ell}$, being ℓ the length of each cell. Hence, in the multidimensional case, according to the Bloch-Floquet theorem, the following relations hold,

$$\begin{bmatrix}\boldsymbol{A} & \boldsymbol{B}\\ \boldsymbol{C} & \boldsymbol{D}\end{bmatrix}\cdot\begin{bmatrix}\boldsymbol{V}_{in}\\ \boldsymbol{I}_{in}\end{bmatrix} = \boldsymbol{\psi}\begin{bmatrix}\boldsymbol{V}_{in}\\ \boldsymbol{I}_{in}\end{bmatrix} \tag{31}$$

which is an eigensystem with eigenvalues $\psi_n = e^{-\gamma_n\ell}$. For a half-T unit cell, $ABCD$ parameters are,

$$\boldsymbol{A} = \boldsymbol{I}_N + \boldsymbol{Z}_1\boldsymbol{Y}_2 \tag{32a}$$

$$\boldsymbol{B} = \boldsymbol{Z}_1, \tag{32b}$$

$$\boldsymbol{C} = \boldsymbol{Y}_2, \tag{32c}$$

$$\boldsymbol{D} = \boldsymbol{I}_N. \tag{32d}$$

The computation of the eigenvalues ψ_n leads to determine the dispersion relations. The eigensystem (31) can be rewritten as a homogeneous linear system which must have a zero determinant to provide non trivial solution [3]. For coupled CRLH-LNs, the eigenvalues ψ_n are computed as the solution of the following equation,

$$\det\begin{bmatrix}\boldsymbol{A} - \boldsymbol{\psi}_n & \boldsymbol{B}\\ \boldsymbol{C} & \boldsymbol{D} - \boldsymbol{\psi}_n\end{bmatrix} = 0. \tag{33}$$

From its solutions ψ_n, the propagation constants are obtained as,

$$\gamma_n = -\frac{1}{\ell}\log\psi_n \tag{34a}$$
$$\alpha_n = \mathrm{Re}(\gamma_n), \tag{34b}$$
$$\beta_n = \mathrm{Im}(\gamma_n). \tag{34c}$$

For a single CRLH-LN with a half-T unit cell, it is trivial finding,

$$\gamma = -\frac{1}{\ell}\log\left(1+\frac{Z_1Y_2}{2}\pm\sqrt{\left(1+\frac{Z_1Y_2}{2}\right)^2-1}\right) \tag{35}$$

where ℓ is the length of each section.

In [4] it is shown that CRLH-LN is equivalent to the homogenous CRLH-TL for small electrical lengths and the dispersion relation obtained applying periodic boundary conditions reduces to the homogenous dispersion relation. Since such a condition holds only within a limited frequency range, the transmission line model cannot be used for accurate broadband time-domain analysis of CRLH-LN structures. In fact, due to the left-handed lumped elements C_L and L_L, for a fixed length ℓ, the imaginary part of the propagation constant greatly differs, at low frequencies, from that of the transmission line, as confirmed by the numerical results in the next section.

V. NUMERICAL RESULTS

A. *Dispersion diagram analysis*

To the aim of investigating the difference between the continuous and the periodic structures, the CRLH-LN described in [4] has been considered. It is characterized by global parameters $R = 10^{-3}\ \Omega, L_R = 2.45$ nH, $C_L = 0.68$ pF, $G = 10^{-3}$ S, $C_R = 0.5$ pF and $L_L = 3.38$ nH; 10 unit cells have been considered of length $\ell = 6.1$ mm.

Figure 4 shows the dispersion diagram of the CRLH-LN described in ([4], page 41) using the Bloch-Floquet theorem [3], the approximated one under the hypothesis of electrically small sections and that of a homogeneous CRLH-TL. It is seen that the hypothesis of electrically small network leads to significantly different results from the Bloch-Floquet theorem in the gigahertz range.

This result is expected since the wavelength is inversely proportional to the phase constant β. At frequencies below 1 GHz the phase constant of the CRLN-LN is larger than that of the CRLH-TL, leading to smaller wavelengths. Figure 5 shows the phase velocity diagram. Again, a significant difference is observed, below 1 GHz, between the result of the Bloch-Floquet theorem and those obtained assuming the hypothesis of electrically small sections.

Figure 6 shows the attenuation constant as evaluated using the homogeneous CRLH-TL and the discrete CRLH-LN models. A significant difference is observed up to few gigahertz.

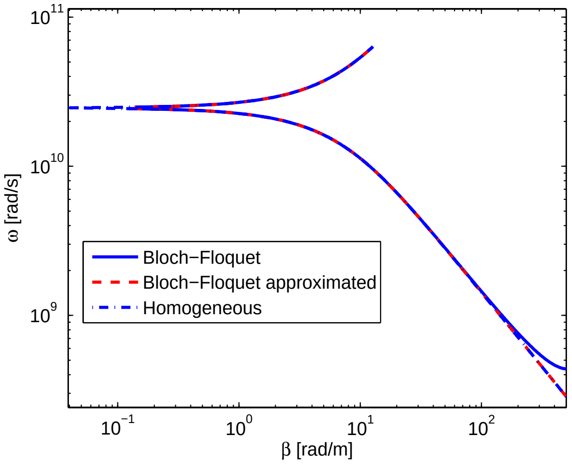

Fig. 4. Dispersion diagram. The solid line refers to the Bloch-Floquet theorem, the dashed line refers to the approximation under the hypothesis of electrically small network, the dashdot line refers to the homogeneous CRLN-TL (example V-A).

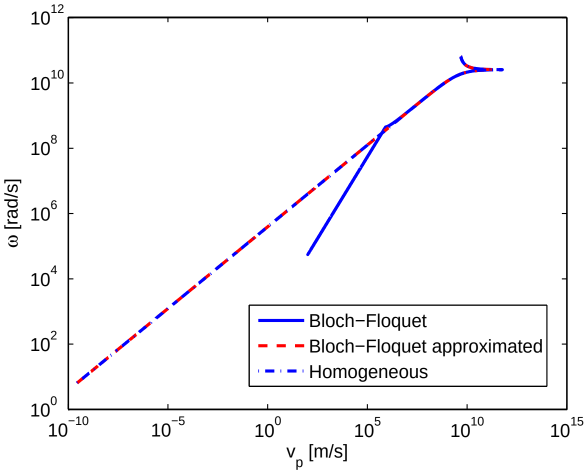

Fig. 5. Phase velocity diagram. The solid line refers to the Bloch-Floquet theorem, the dashed line refers to the approximation under the hypothesis of electrically small sections, the dashdot line refers to the homogeneous CRLN-TL (example V-A).

The previous results point out that the homogeneous CRLH-TL may be not accurate at low frequencies and may generate inaccuracies when adopted for broadband macromodeling of CRLH-LN structures.

Figure 7 shows the poles in the complex plane. A large number of poles is clustered close to zero and determine the left handed low frequency oscillatory behavior of the response.The selection of dominant poles may be a difficult task due to the presence of many clustered poles which leads to ill-conditioning.

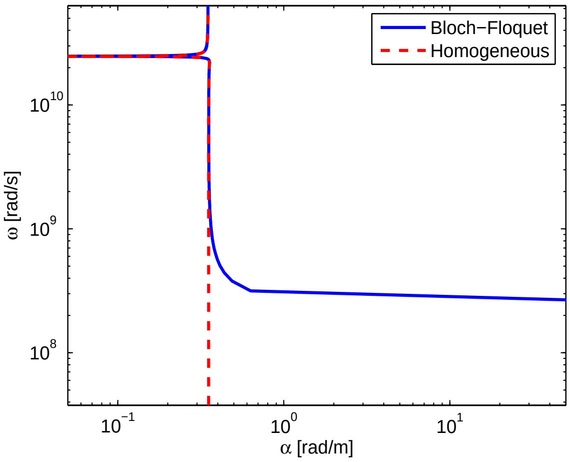

Fig. 6. Attenuation constant (example V-A).

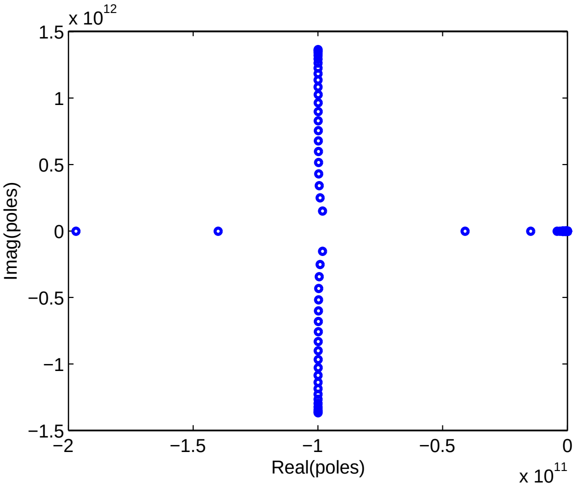

Fig. 7. Location of poles in the complex plane (example V-A).

The chain parameters of the CRLH-LN of order 10 have been computed using the proposed polynomial method and compared with those obtained by inversion of the global transmission matrix computed as cascade of ten identical sections and those of the equivalent CRLH-TL. Figure 8 shows the magnitude spectrum of Φ_{11} up to 0.5 GHz. It is clearly seen that the polynomial approach is in a very good agreement with the result of the CRLH-LN while, again, the equivalent CRLH-TL exhibits a significant difference.

The CRLH-LN has been excited by a pulse with 100 ps rise and fall times and width 5 ns. The input is terminated on 50 Ω resistance, the output port is left open. Figure 9 shows a sample of the output voltage as evaluated using the equivalent CRLH-TL model via IFFT, the half-T ladder network via IFFT and the proposed time-domain macromodel.

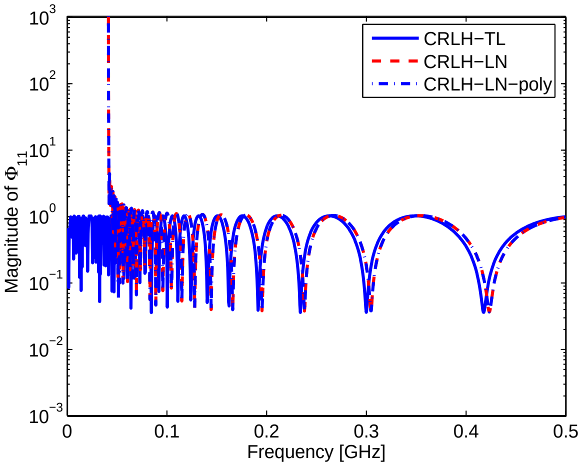

Fig. 8. Chain parameter Φ_{11}. The solid line refers to the equivalent CRLH-TL, the dashed line refers to the result obtained by inversion of the global transmission matrix, the dashdot line refers to the proposed polynomial approach (example V-A).

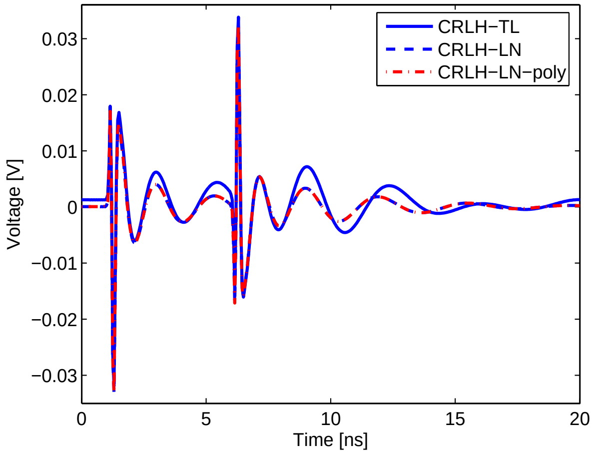

Fig. 9. Output voltage. The solid line refers to the equivalent CRLH-TL via IFFT, the dashed line refers to the result obtained by inversion of the CRLH-LN model via IFFT, the dashdot line refers to the proposed time-domain macromodel (example V-A).

As before, the polynomial-based macromodeling approach is in perfect agreement with the analysis of the global ladder network while the equivalent CRLH-TL exhibits a significant difference. In particular, the CRLH-LN is characterized by a larger attenuation than the CRLH-TL, as expected from Fig. 6. Furthermore, the use of the IFFT, combined with a underestimated attenuation, causes a not accurate *dc* value of the CRLH-TL results.

B. Two coupled CRLH-LNs

In the second example a coupled CRLH-LN is considered. It is constituted by 40 half-T cells with parameters $L_{R1} = L_{R2} = 1.938$ nH, $C_{R1} = C_{R2} = 0.841$ pF, $L_{L1} = L_{L2} = 0.749$ nH, $C_{L1} = C_{L2} = 0.416$ pF, $L_M = 0.361$ nH, $C_M = -0.189$ pF, $R_1 = R_2 = 10$ mΩ, $G_1 = G_2 = 1$ mΩ. The coupled ladder networks are terminated on 50 Ω resistances at the input ports and 1.5 pF capacitances at the output ports. The rational macromodel has been generated leading to 316 poles; among them only 172 have been selected as dominant in the 0-20 GHz range. Figure 10 shows the location of poles in the complex plane: the circles refer to the set of poles of the CRLH-LN, the stars to those selected as dominant.

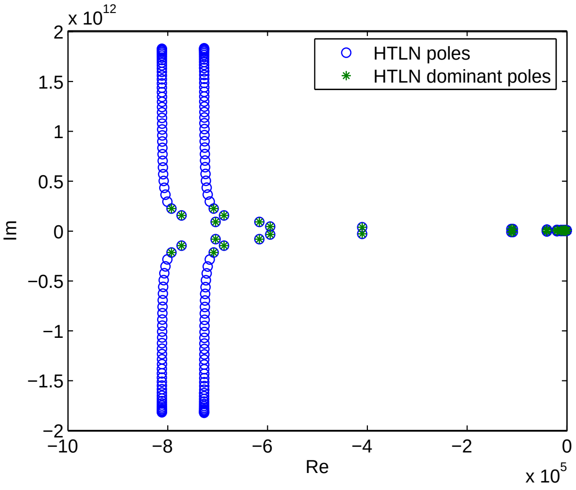

Fig. 10. Location of poles in the complex plane (example V-B).

Figure 11 reports the magnitude of the corresponding residues: circles refer to the set of poles computed by equations (19) and (20), stars indicate those selected as dominant in the frequency range of interest.

A sample of the magnitude and phase spectra of the impedances Z_{11} and Z_{12} is presented in Figs. 12 and 13. For the sake of comparison impedances are computed using both the polynomial (HTLN-pol) and the pole/residue (HTLN-RP) forms; as seen, a perfect agreement is obtained.

The knowledge of poles and residues of the HTLN has allowed to generate a rational macromodel in a state-space form. Figure 14 shows the transient voltage at the input port of the second line as evaluated by using the standard frequency-domain model combined with the IFFT to obtain the time-domain results and the proposed reduced macromodel; as seen, no significant difference is observed.

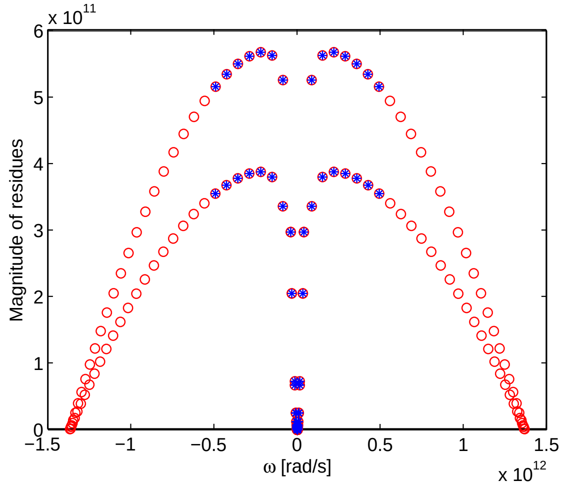

Fig. 11. Magnitude of residues of impedance Z_{13} (example V-B).

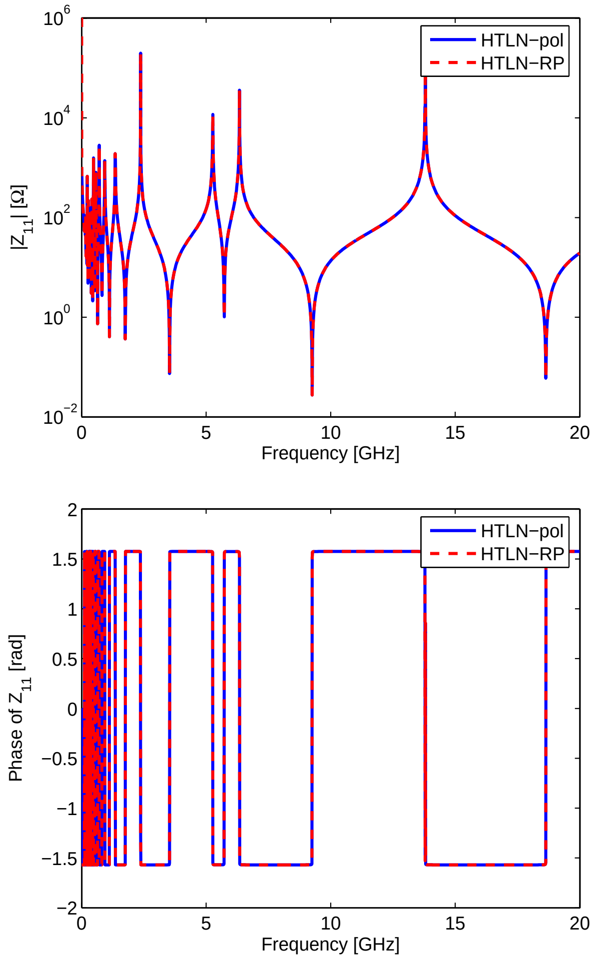

Fig. 12. Magnitude and phase spectra of Z_{11} (example V-B).

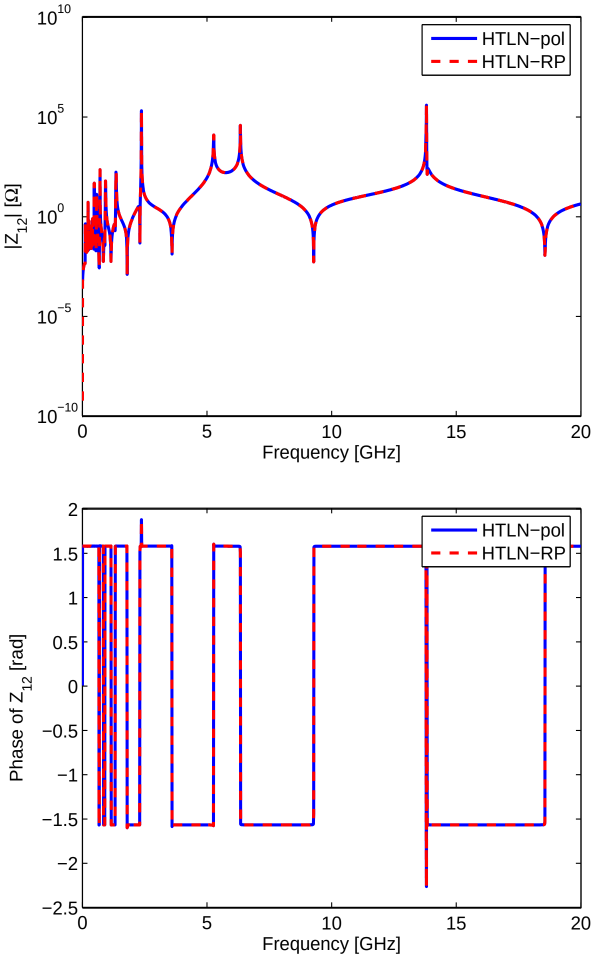

Fig. 13. Magnitude and phase spectra of Z_{12} (example V-B).

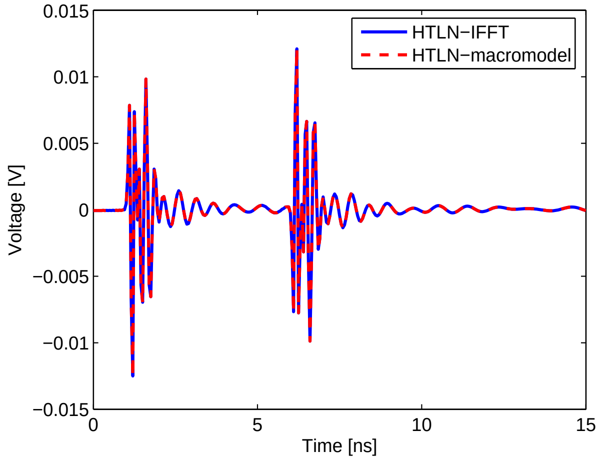

Fig. 14. Port voltage V_2 (example V-B).

C. Four coupled CRLH-LNs

In the third test the CRLH-LN is obtained using four equally spaced coplanar microstrips ($\ell = 0.1\text{m}, \sigma = 5.8 \cdot 10^7$ S/m) on a alumina substrate ($\varepsilon_r = 9.8$). The cross section of the CRLH-LN structure is sketched in Fig. 15. The width of the strips is $w = 241$ μm, the spacing is $s = 800$ μm, the thickness of the dielectric and conductors are $h = 254$ and $t = 34.8$ μm, respectively, the shoulder $d = 2021.6$ μm. The computation of the per-unit-length parameters has been performed using the method of moments [23], yielding,

$$\boldsymbol{L}_r = \begin{bmatrix} 0.3982 & 0.01369 & 0.00387 & 0.00203 \\ 0.01369 & 0.3979 & 0.01357 & 0.00387 \\ 0.00387 & 0.01357 & 0-3979 & 0.01369 \\ 0.002037 & 0.00387 & 0.01369 & 0.3982 \end{bmatrix} \mu\text{H/m} \tag{36a}$$

$$\boldsymbol{C}_r = \begin{bmatrix} 172 & -0.5501 & -0.1206 & -0.0616 \\ -0.5501 & 172 & -0.5462 & -0.1206 \\ -0.1206 & -0.5462 & 172 & -0.5501 \\ -0.0616 & -0.1206 & -0.5501 & 172 \end{bmatrix} \text{pF/m}, \tag{36b}$$

$$\boldsymbol{R} = \begin{bmatrix} 80.83 & 2.399 & 0.7926 & 0.4507 \\ 2.399 & 80.80 & 2.381 & 0.7926 \\ 0.7926 & 2.381 & 80.80 & 2.399 \\ 0.4507 & 0.7926 & 2.399 & 80.83 \end{bmatrix} \Omega/\text{m}, \tag{36c}$$

$$\boldsymbol{G} = \begin{bmatrix} 0 & 0 & 0 & 0 \\ 0 & 0 & 0 & 0 \\ 0 & 0 & 0 & 0 \\ 0 & 0 & 0 & 0 \end{bmatrix} \text{S/m}. \tag{36d}$$

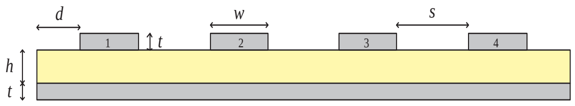

Fig. 15. Coplanar microstrips cross section (example V-C).

The microstrips are loaded with 15 longitudinal capacitances $C_L = 0.15$ nF and transverse inductances $L_L = 0.2$ μH.

The presence of the longitudinal capacitance C_L and the transverse inductance L_L causes a complex resonant behavior even at low frequency. Figure 16 shows an example of the magnitude spectrum of the input impedance $\boldsymbol{Z}_{11}$ evaluated using both the polynomial approach and the residue-pole form. The spectrum exhibits several resonances from 0 to 500 MHz while the inductive nature dominates at higher frequencies.

This fact is confirmed by the location of the poles in the complex plane, shown in Fig. 17. It is easy to recognize four families of poles, corresponding to four decoupled CRLH-LN and a cluster of poles close to zero determining the highly oscillating behavior at low frequency.

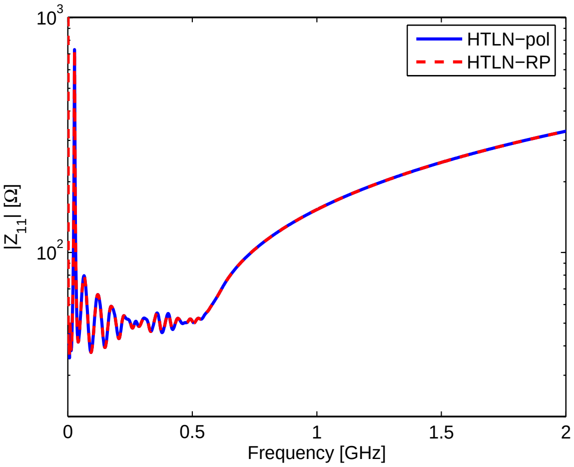

Fig. 16. Magnitude spectrum of impedance Z_{11} (example V-C).

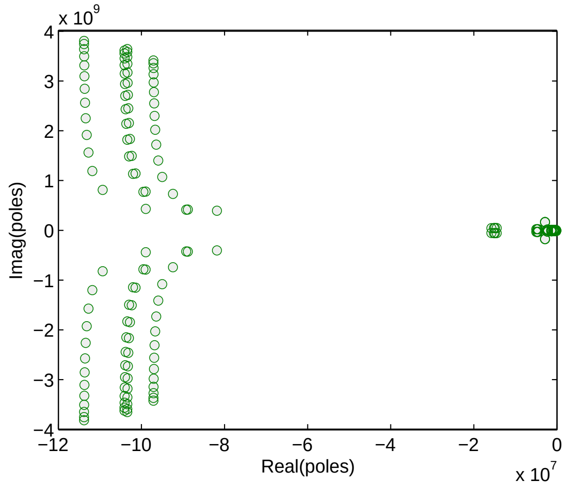

Fig. 17. Location of poles in the complex plane (example V-C).

The rational macromodel has been generated in the state-space form. The four CRLH-LNs are terminated on 50 Ω at the input ports and 2 pF capacitances at the output ports. Figure 18 shows the transient voltages at the output of the first and fourth CRLH-LN as evaluated using the frequency-domain approach via inverse fast Fourier transform (HTLN-IFFT) and the proposed macromodel (HTLN-macromodel). Again, a very good agreement is obtained.

VI. CONCLUSIONS

In this work a systematic approach to coupled CRLH-LNs is presented. The closed-form two-port representation of CRLH-LNs is obtained relying on analytical polynomials which allow to exactly represent voltages and currents along the network. The rational form of the impedance matrix $\boldsymbol{Z}$ allows an easy identification of the true poles and the corresponding residues of the CRLH-LN and, thus, the generation of a rigorous state-space macromodel which is proved to be accurate from *dc* to daylight. Hence, the proposed method is well suited to represent N-coupled CRLH-LNs with general topology of longitudinal impedance $\boldsymbol{Z}_1$ and transverse admittance $\boldsymbol{Y}_2$. The presented numerical results have validated the method and confirmed its accuracy when compared with standard frequency-domain techniques.

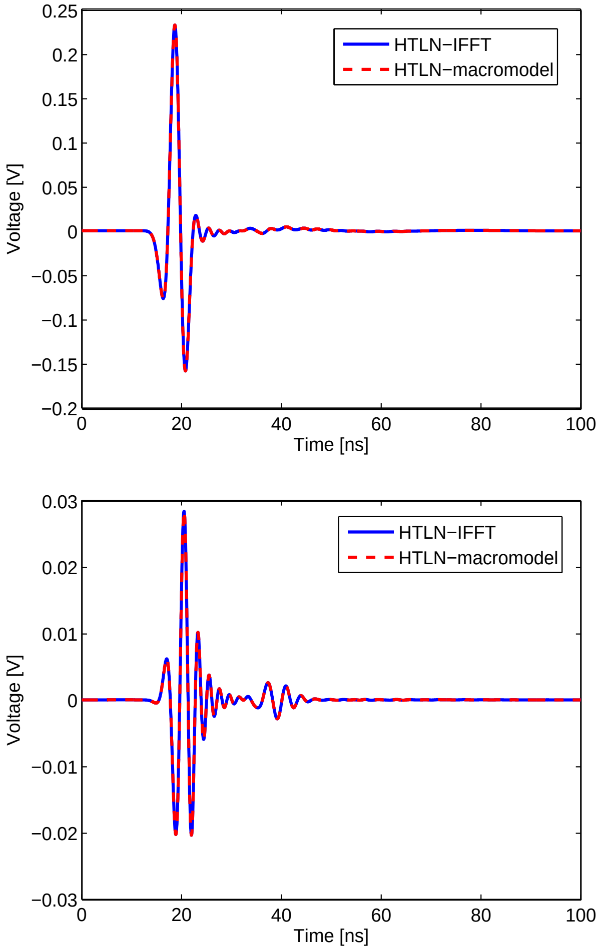

Fig. 18. Transient voltages at the output port of the first (top) and forth (bottom) CRLH-LNs (example V-C).

REFERENCES

[1] V. G. Veselago, “The electrodynamics of substances with simultaneously negative values of ε and μ,” *Sov. Phys. Usp.*, vol. 47, pp. 509–514, Jan.-Feb., 1968.

[2] C. Caloz and T. Itoh, “Transmission line approach of left-handed (LH) materials and microstrip implementation of an artificial LH transmission line,”

IEEE Transactions on Antennas and Propagation, vol. 52, no. 5, pp. 1159–1166, May 2004.

[3] ——, *Electromagnetic Metamaterials: Transmission Line Theory and Microwave Applications*. Wiley-IEEE Press, 2005.

[4] A. Lai, C. Caloz, and T. Itoh, "Composite right/left-handed transmission line metamaterals," *IEEE Microwave Magazine*, pp. 34–50, Sep. 2004.

[5] Y. Zhang and B. E. Spielman, "A stability analysis for time-domain method of moments analysis of 1-D double-negative transmission lines," *IEEE Transactions on Microwave Theory and Techniques*, vol. 55, no. 9, pp. 1887–1898, Sep. 2007.

[6] C. R. Paul, *Analysis of Multiconductor Transmission Lines*. New York, NY: John Wiley & Sons, 1992.

[7] A. Alù and N. Engheta, "Pairing an epsilon-negative slab with a mu-megative slab: resonance, tunneling and tranparency," *IEEE Transactions on Antennas and Propagation*, vol. 51, no. 10, pp. 2558–2570, Oct. 2003.

[8] ——, "Physical insight into the growing evanuescent fiels of double-negative metamaterial lenses using their circuit equivalence," *IEEE Transactions on Antennas and Propagation*, vol. 54, no. 1, pp. 268–272, Jan. 2006.

[9] G. V. Eleftheriades and K. G. Balmain, *Negative Refraction Metamaterials: Fundamental Principles and Applications*. Wiley-IEEE Press, 2005.

[10] P. P. So and W. J. R. Hoefer, "Time domain TLM modeling of metamaterials with negative refractive index," pp. 1779–1782, Jun 2004.

[11] A. Rennings, S. Otto, C. Caloz, A. Lauer, W. Bilgic, and P. Waldow, "Composite right/left-handed extended equivalent circuit," *Int. J. Numer. Model.*, vol. 19, pp. 141–172, 2006.

[12] R. F. Harrington, *Field Computation by Moment Methods*. Malabar: Krieger, 1982.

[13] G. Antonini, "Reduced order modeling for metamaterial transmission lines," *Applied Computational Electromagnetic Society Newsletter*, vol. 21, no. 3, pp. 78–103, Nov. 2006.

[14] H. V. Nguyen and C. Caloz, "Generalized couple-mode approach of metamaterial coupled-line couplers: coupling theory, phenomenological explanation and experimental demonstration," *IEEE Transactions on Microwave Theory and Techniques*, vol. 55, no. 5, pp. 1029–1039, May 2007.

[15] B. Gustavsen and A. Semlyen, "Rational approximation of frequency domain responses by vector fitting," *IEEE Transactions on Power Apparatus and Systems*, vol. 14, no. 3, pp. 1052–1061, Jul. 1999.

[16] D. Deschrijver, B. Haegeman, and T. Dhaene, "Orthonormal vector fitting : a robust macromodeling tool for rational approximation of frequency domain responses," Feb. 2007.

[17] D. Deschrijver, T. Dhaene, "Broadband macromodelling of passive components using orthonormal vector fitting," *Electronics Lett.*, vol. 41, no. 21, pp. 1160–1161, Oct. 2005.

[18] G. V. Eleftheriades, O. Siddiqui, and A. K. Iyer, "Transmission line models for negative refractive index media and associated implementations without excess resonators," *IEEE Microwave and Wireless Components Letters*, vol. 13, no. 2, pp. 51–53, Feb. 2003.

[19] J. Vlach and K. Singhal, *Computer Methods for Circuit Simulation*. Van Nostrand Reinhold Co, New York, 1983.

[20] M. Faccio, G. Ferri, and A. D'Amico, "A new fast method for ladder networks characterization," *IEEE Transactions on Circuits and Systems, I*, vol. 38, no. 11, pp. 1377–1382, Nov. 1991.

[21] M. Faccio, G. Ferri, A. D'Amico, "The DFF and DFFz triangles and their mathematical properties," *Applications of Fibonacci Numbers, G. E. Bergum et al.,(eds)*, vol. 5, pp. 199–206, 1990.

[22] E. W Weisstein, "Quartic Equation," *Mathworld–A Wolfram Web Resource*, http://mathworld.wolfram.com/QuarticEquation .html.

[23] A. R. Djordjevic, M. B. Bazdar, T. K. Sarkar, and R. F. Harrington, *Matrix parameters for multiconductor transmission lines*. Boston London: Artech House Publishers, 2000.

Giulio Antonini received his Laurea degree (summa cum laude) in Electrical Engineering in 1994 from the Università degli Studi dell'Aquila and the Ph.D. degree in Electrical Engineering in 1998 from University of Rome "La Sapienza". Since 1998 he has been with the *UAq EMC Laboratory*, Department of Electrical Engineering of the University of L'Aquila where he is currently Associate Professor. His research interests focus on EMC analysis, numerical modeling and in the field of signal integrity for high-speed digital systems. He has authored or co-authored more than 120 technical papers and 3 book chapters. Furthermore, he has given keynote lectures and chaired several special sessions at international conferences. He has been the recipient of the IEEE Transactions on Electromagnetic Compatibility Best Paper Award in 1997, the CST University Publication Award in 2004, the IBM Shared University Research Award in 2004, 2005 and 2006; in 2006 he has received a Technical Achievement Award from the IEEE EMC Society "for innovative contributions to computational electromagnetic on the Partial Element Equivalent Circuit (PEEC) technique for EMC applications". He holds one European Patent.Prof. Antonini is vice-chairman of the dell'IEEE EMC Italy Chapter, he is member of the TC-9 committee and vice-chairman of the TC-10 Committee of the IEEE EMC Society. Prof. Antonini serves as reviewer in a number of international journals.

A Novel Green's Function Analysis of Wave Scattering by an Infinite Grating using Complex Images Technique

[1]H. Alaeian and [2]R. Faraji-Dana

Center of Excellence on Applied Electromagnetic Systems,
School of Electrical & Computer Engineering, University of Tehran, P.O. Box 14395-515, Tehran, Iran
[1]h.alaian@ece.ut.ac.ir, [2]reza@ut.ac.ir

Abstract – A new method, based on the complex images technique is presented for solving the electromagnetic scattering from the infinite metallic and dielectric gratings. The main idea of this method lies in representing the infinite summation of the structure period Green's functions in terms of finite summations of complex images. The method of moments (MoM) is then employed to find the current distribution, reflection and transmission coefficients of the gratings. The validity of the presented method is shown through various examples for different grating geometries and incident wave polarizations. Fast convergence, simple formulations and flexibility of the method in analyzing different structures are the main advantages of the proposed method.

Keywords: Integral equation, grating, Green's function, complex image.

I. INTRODUCTION

Theoretical studies of electromagnetic scattering from periodic metallic or dielectric structures or gratings go back to more than a hundred years ago [1, 2]. Since then various analytical or numerical techniques have been developed to formulate the electromagnetic scattering from the periodic scatterers [3, 4].

The interesting feature of these structures as frequency and polarization selective devices and their extra degree of freedom in controlling the scattered fields, have made them an important choice in design and fabrication of various devices especially at microwave and optical frequencies. In fact they have been used extensively in the fabrication of devices such as filters, waveguides, couplers, sensors, antenna substrates and reflectors [5, 6].

In recent years the emergence of photonic bandgap devices in discrete periodic dielectric and metallic structures and their potentials in realizing narrow-band filters, high-quality resonators, linear waveguides and mirrors have attracted much attention toward the topic of periodic structures. Beside photonics, plasmonic phenomena dealing with periodic metallic structures in optical frequencies further improved this topic. The observation of enhanced transmission phenomena in subwavelength perforated metallic screens has directed lots of studies to the investigation of transmittance and reflectance behavior of the metallic gratings in those devices [7, 8].

A one-dimensional periodic array of cylindrical objects made of metal or dielectric is a typical geometry of periodic structures. The frequency response of the array is determined by the scattering characteristics of each cylinder and the multiple scattering under the presence of the periodic scatterers. A two-dimensional photonic bandgap structure can be obtained with multilayered one-dimensional arrays. The multiple interaction of the scattered space harmonics from these layers modifies the electromagnetic properties of the final structure [9]. Various frequency responses can be obtained by using different types of scatterers and arranging them in different geometries. During the past decade, a vast amount of investigation on the electromagnetic scattering by layered periodic arrays of cylindrical objects has been done. In these investigations various techniques such as mode matching method, homogenization method, Fourier modal method, finite difference method and time domain techniques have been applied to the periodic structures [9-17]. Integral equation methods are among the most accurate and flexible semi-analytical approaches that have been used in analyzing such structures [18]. Efficient computation of the slowly convergent series of periodic Green's functions encountered in these methods is still the main challenge of their applications in this domain.

In this paper, we will present an accurate integral equation method for dealing with a two-dimensional electromagnetic scattering from periodic arrays of cylindrical objects based on the complex images Green's function, for the first time. The approach is quite general with the capability to be applied on various configurations of periodic arrays of two-dimensional metallic or dielectric cylindrical objects. In the proposed method the periodic Green's function has been efficiently approximated with a finite series of complex images and a closed form can be obtained through this approximation. This approximated Green's function has been used afterward in the analysis of the one-dimensional periodic cylindrical objects. The reflectance and transmittance behavior of metallic and dielectric gratings with circular and rectangular cross-sectioned rods for different polarizations have been computed and compared as a representation of the method versatility.

This paper is organized as follows. In section II, the complex images representation of the Green's function for one-dimensional periodic structures is developed. Section III is devoted to the MoM formulation of the problem based on the developed complex images Green’s function. As E and H-modes are two independent solutions of the 2D case, the formulation has been done for these two cases, separately. The diffraction properties of a general polarization can be obtained through its decomposition to these two fundamental modes.

In section IV numerical results will be presented. At first the validity of the complex images Green's function is shown through an example. Then the grating simulation results will be presented showing the behavior of different gratings against various polarizations. The validity of these results has been investigated by checking the energy balance and edge conditions. Concluding remarks with be given in section V.

II. COMPLEX IMAGES REPRESENTATION OF A 1-D PERIODIC GREEN'S FUNCTION

According to Floquet-Bloch theorem Eigen modes in a periodic lattice can be expressed as $G(\vec{r})\exp(-j\vec{k}.\vec{r})$ where G is the distribution in a unit cell and $\vec{k}$ is the lattice wavevector [19]. This simply means that the propagation of a mode in a periodic lattice leads to a phase change without any variations in the form of its distribution. Using this concept, it is quite straight forward to show that the Green's function of a one-dimensional periodic structure, as shown in Fig.1 can be expressed as,

$$G^{per}(\vec{r}\,|\,\vec{r}\,')=\sum_{m=-\infty}^{\infty} G(\vec{r}\,|\,x'+md, y', z')\, e^{-jmdk_x} \quad (1)$$

where G is the Green's function of a source of the array and d is the period of the lattice (Fig. 1). As the gratings are composed of two-dimensional cylindrical objects, one-dimensional array of line sources should be considered here. Therefore $G(r,r')$ can be written as,

$$G=\frac{1}{4j}H_0^{(2)}(k_0\sqrt{(x-x'-md)^2+(y-y')^2}\,)\;. \quad (2)$$

The series in equation (1) converges very slowly especially when the observation point is far from the field point. It is also known that applying Poisson's transform to that series leads to its corresponding modal series which suffers from slow convergence for near fields. In order to accelerate the convergence of these kind of series different methods such as Kummer's transform, Ewald transform and Shank's transform have been proposed in the literature [20, 21]. Although these methods can be successfully applied to the periodic Green’s functions in the form of equation (1), it must be kept in mind that these Green's functions are used in the kernel of the integral equations. Therefore the employed integral equation methods will suffer from numerical deficiency as the Green’s functions would have no closed form representation. In the complex images representation developed below however, the periodic Green’s function of equation (1) is given in a closed form which is valid for all the sources and field points. This will bring numerical efficiency to the relevant integral equation techniques.

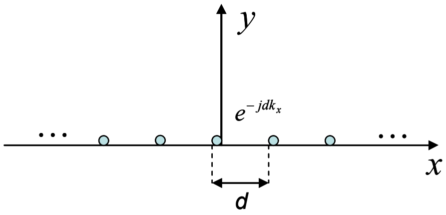

Fig. 1. One-dimensional array of line sources.

In order to derive the complex images representation of equation (1) while $G(r,r')$ has been replaced with equation (2), we can use the following identity,

$$\frac{1}{4j}H_0^{(2)}(k_0\sqrt{(x-md)^2+y^2}\,) =\frac{1}{2\pi}\int_{-\infty}^{\infty}\frac{e^{-j\beta_x|x-md|}}{j2\beta_x}e^{-jk_y y}\,dk_y \quad (3)$$

where $\beta_x=\sqrt{k_0^2-k_y^2}$.

By substituting equation (3) in equation (1) and changing the order of summation and integration operators, a geometric series will be obtained. For field points in a unit cell i.e. $0<x<d$ ($x'=0$ is assumed) after some simple manipulations the following equation can be obtained,

$$G^{per}(\vec{r}\,|\,\vec{r}\,')=\frac{1}{2\pi}\int_{-\infty}^{\infty}\frac{e^{-jk_y y}}{j2\beta_x}\,\frac{e^{-j\beta_x x}}{1-e^{j(k_x-\beta_x)d}}\,dk_y + \frac{1}{2\pi}\int_{-\infty}^{\infty}\frac{e^{-jk_y y}}{j2\beta_x}\,\frac{e^{-j\beta_x|x-d|}}{1-e^{-j(k_x+\beta_x)d}}\,dk_y\;. \quad (4)$$

As the name of complex images technique implies the main goal is to preserve the form of the original sources and find an approximation that its terms resemble the ones in the first series [22]. Obviously this aim can be fulfilled if the fractions in the kernel of inverse Fourier

Transform integral of equation (4) can be approximated by a finite series of exponential. That is,

$$\frac{e^{-j\beta_x x}}{1-e^{j(k_x-\beta_x)d}} = e^{-j\beta_x x} + \frac{e^{j(k_x-\beta_x)d}}{1-e^{j(k_x-\beta_x)d}}\, e^{-j\beta_x x} \tag{5a}$$
$$= e^{-j\beta_x x} + \sum_{m=1}^{M_1} a_m e^{-j(x+jb_m)\beta_x}$$

and

$$\frac{e^{-j\beta_x|x-d|}}{1-e^{-j(k_x+\beta_x)d}}$$
$$= e^{-j\beta_x|x-d|} + \frac{e^{-j(k_x+\beta_x)d}}{1-e^{-j(k_x+\beta_x)d}}\, e^{-j\beta_x|x-d|}\,. \tag{5b}$$
$$= e^{-j\beta_x|x-d|} + \sum_{m=1}^{M_2} c_m e^{-j(|x-d|+jd_m)\beta_x}$$

Prony's method [22], GPOF [23] or least square methods can be used to realize these approximations accurately. The approximation path of Fig. 2 in the β_x plane has been found to be appropriate to perform the above approximations. In this path T_0 is determined according to the relative distance between field and source points [22]. It may be mentioned that the existence of poles which may occur near the approximation path (Fig. 2) can deteriorate the above mentioned approximation. In that case one can extract the poles from the approximating function and include its effects manually [22].

Substituting the above approximations in equation (4) and using the identity equation (3) leads to,

$$\begin{aligned}G^{per}(r,r') &= \frac{1}{4j}H_0^{(2)}\left(k_0\sqrt{x^2+y^2}\right)+\\ &e^{-jdk_x}\frac{1}{4j}H_0^{(2)}\left(k_0\sqrt{(x-d)^2+y^2}\right)+\\ &\sum_{m=1}^{M_1} a_m\frac{1}{4j}H_0^{(2)}\left(k_0\sqrt{(x+jb_m)^2+y^2}\right)+\\ &\sum_{m=1}^{M_2} c_m e^{-jdk_x}\frac{1}{4j}H_0^{(2)}\left(k_0\sqrt{(|x-d|+jd_m)^2+y^2}\right).\end{aligned} \tag{6}$$

This completes the derivation of complex images representation of the periodic Green's function of equation (1). It can be seen that the first two terms in equation (6) correspond to the two of sources in the array that have the most effects on the field points located in a unit cell. The presence of these two terms in the final representation guarantees satisfactory results for the near fields especially in the vicinity of the boundaries. The two finite summations in equation (6) correspond to the complex images which have the same forms as real sources in the array except that they are located in complex positions and have complex values. They are more important when the field point is located away from the boundaries within a unit cell. It is clear that equation (6) offers a closed form representation of the Green's functions in terms of two finite summations; so the issue of convergence for infinite series does not exist anymore. It is clear that the same procedure can be applied to an array of point sources. Moreover it can be easily extended to 2-D periodic Green's functions of line sources, and to the 2-D and 3-D periodic Green's functions of point sources.

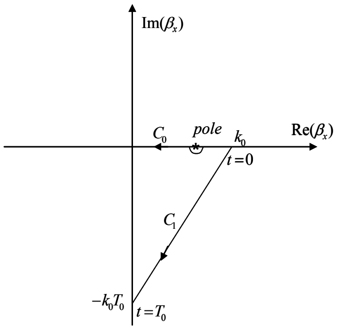

Fig. 2. The approximation path in the β_x plane.

Examination of the accuracy of the developed complex images Green's function will be deferred until section V.

III. MOM FORMULATION OF THE PROBLEM

Figure 3 shows a grating of typical cylindrical objects studied in this paper illuminated by a plane wave with wavevector $\overline{k}$. Since there is no variation along the z-axis, TE and TM polarizations can exist independently.

In TM polarization (H_x, H_y, E_z) are the only existing components of the EM fields. For PEC rods in the array, by applying the proper boundary condition on the rod located in the unit cell, the following electric field integral equation (EFIE) determines the current flowing on the rod.

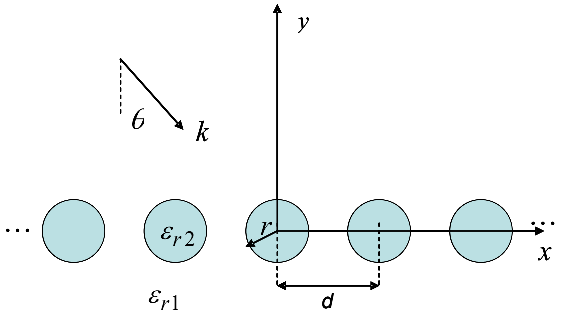

Fig. 3. Cross section of a grating of typical cylindrical objects.

$$E_z^{inc}(l) = j\omega\mu_0 \oint_{body} G^{per}(l,l')J_z(l')dl' . \qquad (7)$$

In TE polarization (E_x, E_y, H_z) are the only existing components of the EM fields. Considering the same PEC rods and formulating the problem for magnetic field after applying the proper boundary condition on the rod, the following magnetic field integral equation (MFIE) gives the current distribution.

$$J_l(l) = H_z^{inc}(l) + \oint_{body} \frac{\partial G^{per}(l,l')}{\partial n'} J_l(l')dl' . \qquad (8)$$

In the above integral equations G^{per} is given by equation (6) while l represents the transverse coordinate on a rod [24].

For a grating made of dielectric rods instead of PEC (Fig. 3), one can derive the integral equations by using the equivalent surface electric and magnetic currents and boundary integral equations (BIE). The equivalent surface currents are given by,

$$\begin{array}{l} \vec{J}_s(l) = \alpha\, \hat{n} \times \vec{H}_t(l) \\ \vec{M}_s(l) = -\alpha\, \hat{n} \times \vec{E}_t(l) \end{array} \quad . \qquad (9)$$

Where subscript t represents the total field on the boundary of the rod and α is a factor equal to 1 and -1 for exterior and interior problems, respectively. Using these equivalent currents the following equations can be written for exterior and interior regions in TM polarization, respectively,

$$\begin{array}{l} \vec{E}^{inc}(l) + \vec{E}^{sca}(l) = 0 \quad l \in interior\ region \\ \vec{E}^{sca}(l) = 0 \quad l \in exterior\ region\ . \end{array} \qquad (10)$$

Similarly the above equations can be written for H in a TE polarized illumination.

To solve for the unknown current distribution in the above integral equations, the method of moments has been employed by using pulse basis functions and applying the point matching technique [24]. When the current distribution has been determined all the diffraction characteristics of the grating can be obtained using the scattered fields.

Because of the periodic nature of the structure the reflected and transmitted electromagnetic waves contain infinite diffraction orders. The parallel component of the diffraction orders can be obtained from the following formula,

$$k_{\|} = k_x + \frac{2m\pi}{d} = k_0 \sin\theta + \frac{2m\pi}{d} \quad m \in \mathrm{Z} . \qquad (11)$$

The reflectance and transmittance of a grating order have been defined as the ratio of the power carried in that order to the incident power. For a diffracted plane wave to carry energy away from the grating, the following condition must be satisfied,

$$k_0 \geq | k_0 \sin\theta + \frac{2m\pi}{d} | \quad . \qquad (12)$$

In the above relation m is an algebraic integer representing the order of diffraction. The above formula explicitly shows that the number of propagating waves that carry energy away from the grating depends on the incident angle and the normalized frequency as well. The power transmitted to each diffraction order can be controlled by the geometry of the grating and the type of elements composing the array. Using multilayer gratings with various elements one can control the diffraction characteristics of the gratings as well.

Applying different optimization algorithms on the structure it can be optimized to carry power in a determined diffraction order or to obtain a desired frequency response.

In the next section the simulation results of plane wave scattering by different gratings in both polarizations will be presented.

IV. NUMERICAL RESULTS

In this section, first the numerical accuracy of the developed complex images Green's function is examined by using an example. In this example d=4, λ=5 and k_x=0 are assumed in the array of line sources (Fig. 1). Table 1 gives the values of exponential coefficients in the complex images representation (5) for M_1=M_2=5 found through the GPOF algorithm when the path truncation parameter T_0=15 is assumed (Fig. 2).

Table 1. Exponential coefficients for d=4, λ=5 and k_x=0.

a_m	b_m
(-0.1416-j0.2625)×10^{-10}	17.7235-j17.9114
(-0.1226-+j0.9336)×10^{-4}	7.6704-j13.2827
0.0554-0.0106	2.0320-j9.5251
0.7973-j0.6096	-0.04528-j7.6087
1.00425+j0.00564	0.00123-j4.0030

Figure 4 shows the magnitude of the error between the exact spectral function (5a) and its finite summation approximation found through the GPOF technique. The error has been computed along the approximation path of Fig. 2 for different number of exponentials used in the summation. It can be seen that for just 3 terms in the exponential summation an accurate approximation of the spectral function is achieved almost along the whole path.

This demonstrated the efficiency of the proposed approximation.

Figure 5 compares the magnitude and phase of $G^{pre}(r,r')$ found by complex images representation of equation (6) with the values of the Green's function in the form of infinite images and modal series accelerated with the Shanks' transform. It can be seen that the results obtained by the complex images method are in excellent agreements with those obtained from image and modal series. Also it can be observed that the complex images results show the singularity of the source near the boundary while the modal series has difficulty in showing this behavior as its convergence deteriorates in the near fields.

Figure 6 shows the convergence of the approximate complex images Green's function versus number of terms in the summation by evaluating the errors between the results obtained form the infinite modal series and the finite summation of complex images. It is clear that even for small number of terms, i.e., for M=6 negligible errors occur in the proposed complex images representation.

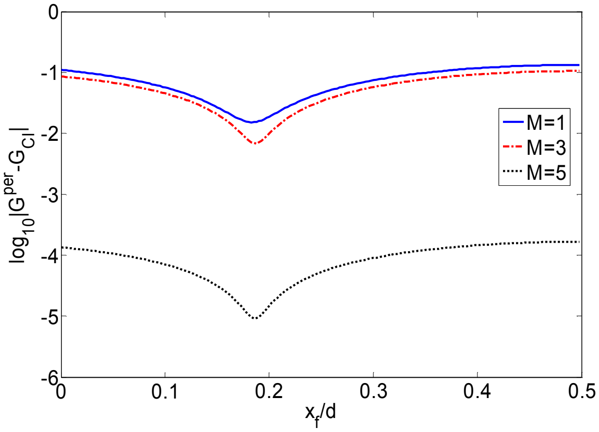

Fig. 6. The magnitude of error at different field points in complex images Green's function for different exponential terms.

The proposed approach has been used in the analysis of various metallic and dielectric gratings. All gratings have been investigated for their reflectance behavior in subwavelength regime where $d/\lambda<1$. In order to study the frequency and polarization selectivity of these structures their responses for different normalized frequencies and polarizations have been obtained. Since, as a filter, the sensitivity of the response to the incident angle is an important factor, this factor has been studied by considering the arrays in a fixed normalized frequency for various incident angles. Finally the effect of the shape on the responses has been studied with comparison of the results of the circular cross sectioned cylinders with square ones. The reflected and transmitted EM fields in each order have been evaluated on a constant line above and below the grating.

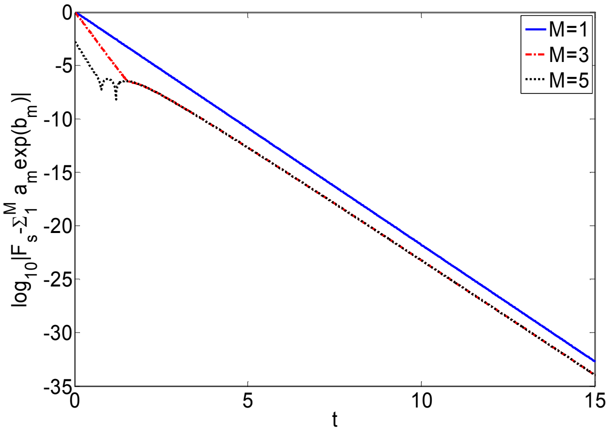

Fig. 4. The magnitude of error between the spectral function and its corresponding finite summation approximation for different number of exponential terms.

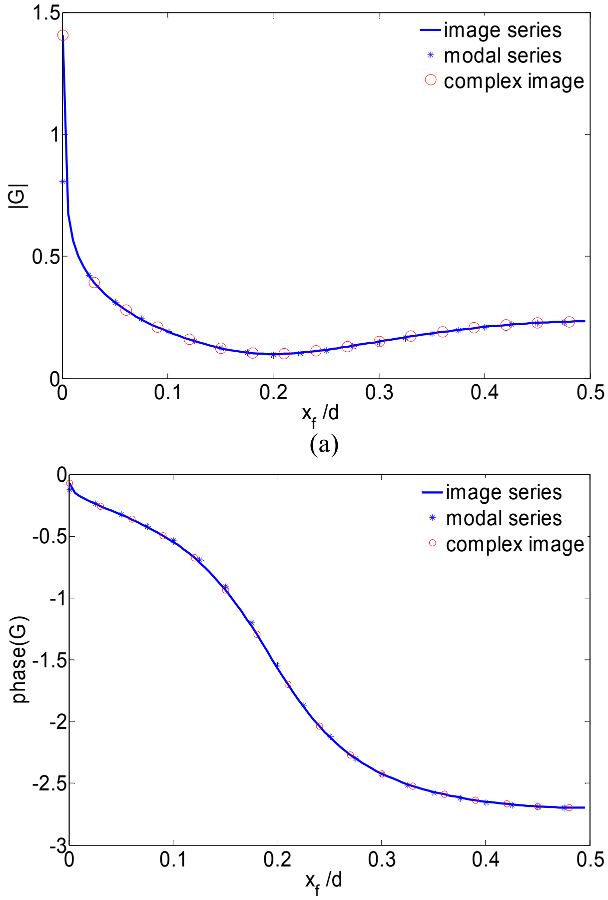

(a)

(b)

Fig. 5. (a) Magnitude, (b) phase of the periodic Green's function of 1-D line sources with d=4, λ=5 and k_x=0 for field points on the x-axis.

The first example (Fig. 7) compares the zeroth order reflection coefficient, R_0, of a metallic grating composed of PEC rods with $r = 0.15d$ with one of a dielectric grating with $r = 0.3d$ and $\varepsilon_r = 2$ for TM polarization. In this case, since the zeroth order is the only propagating component that carries power away from the grating, the figure contains that diffraction order only. Good agreements can be observed between these results and those reported in [25]. In the above figure there is a resonance frequency in the dielectric case while PEC array does not show this behavior.

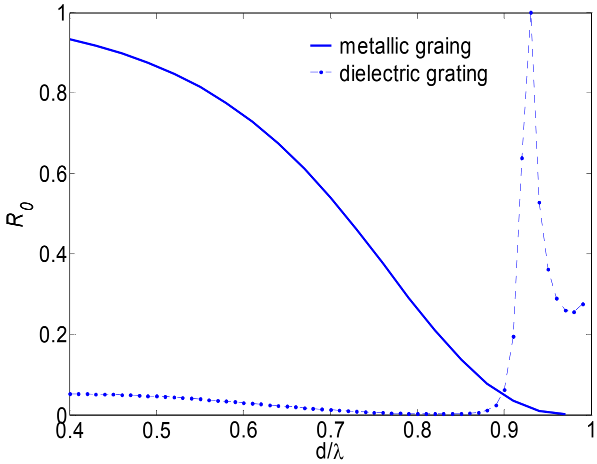

Fig. 7. R_0 versus normalized frequency for gratings composed of PEC rods with r=0.15d and dielectric rods with r=0.3d.

Figure 8 shows the frequency response of a grating composed of PEC rods with r/λ=0.08 located in a medium with ε_{r1}=2.33 when a TM polarized plane wave illuminates the array at θ=45°. Variations of the reflection coefficients R_0, R_{-1}, R_{-2} are given versus the normalized frequency $NF = d / \lambda$.

In this case the metallic grating reflects all the power in a wide range of frequencies and behaves as a reflector. At *NF=0.39* the -1st diffraction order gains the power and decreases the power carried by the zeroth order. At *NF=0.77* the -2nd order carries power as well. Figure 9 shows the response of the same array at *NF=0.5* when the TM polarized incident plane wave illuminates the grating at different angles.

The last example compares the effect of the rods geometry on the diffraction characteristics of the grating. Figure 10 compares the frequency response of the zeroth order reflection coefficient of two metallic gratings, one made of rods with circular cross-section (with r/λ=0.08) and the other made of rods with square cross-section (with a/λ=0.16, where *a* denotes the square side). Both gratings are located in a medium with ε_{r1}=2.33 and are illuminated with a TE-polarized plane wave at θ=45°.

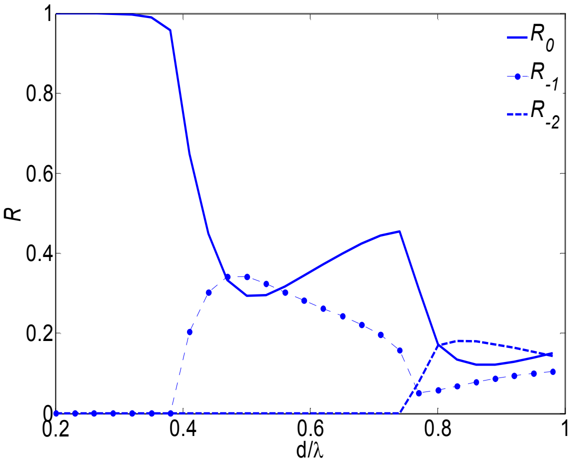

Fig. 8. R_0, R_{-1} and R_{-2} versus normalized frequency for a metallic grating with ε_{r1}=2.33, r=0.08λ and θ=45° for TM polarization.

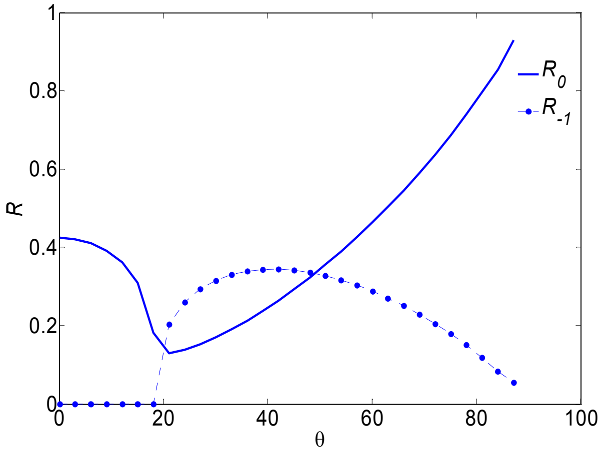

Fig. 9. R_0 and R_{-1} vs. incident angle for a metallic grating with ε_{r1}=2.33, r=0.08λ and NF=0.5 for TM polarization.

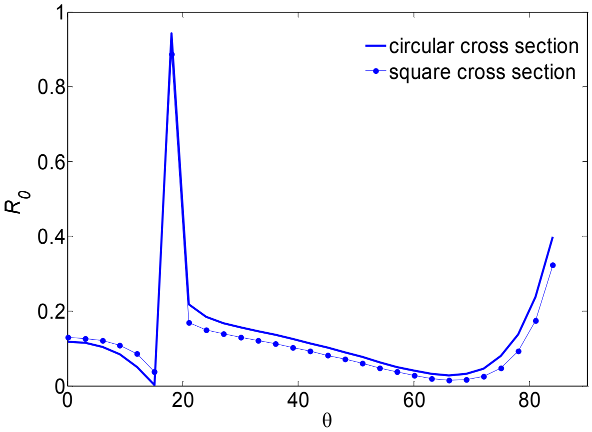

Fig. 10. Comparison of R_0 versus incident angle for two metallic gratings made of rods with circular cross-section with r=0.08λ, and square cross-section with a/λ=0.16 at NF=0.5 for TE polarization.

Comparing these results with those presented in Fig. 9 reveals that the response of a metallic grating varies drastically as the polarization changes. While most of the power is reflected by the grating in TM polarization, in the TE case considerable amount of power is transmitted except for an anomalous increase observed at $\theta=18^o$ angle. Also it can be observed that the rods geometry affects the diffraction characteristics of the grating significantly.

V. CONCLUSION

In this paper a novel complex images representation of the free-space periodic Green's function has been presented. Using this closed form representation, fast and accurate computation of the Green's function is possible for all the field points. Moreover each term in this representation has the same form as the sources forming the periodic array, i.e. a line source for 2-D sources and a point source for 3-D sources. This will facilitate the application of integral equation techniques for analyzing the periodic structures under study significantly.

Using the developed complex images Green's functions in the integral equations, 1-D periodic structures made of PEC or dielectric rods have been investigated and their diffraction characteristics in TE and TM polarizations have been studied.

Although single-row 1-D periodic arrays were considered here, the method can be easily applied to multi-row gratings with different periods and various elements in each row.

ACKNOWLEDGMENT

This work was partially supported by Iran Telecommunication Research Center (ITRC) through a research Grant.

REFERENCES

[1] H. Lamb, "On the reflection and transmission of electric waves by metallic grating," *Proc. London Math. Soc.* vol. 29, no. 1, pp. 523-545, 1898.

[2] L. Rayleigh, "On the dynamical theory of grating," *Proc. R. Soc. (London)*, Ser. A, vol. 79, pp. 399-416, 1907.

[3] V. Twersky, "On scattering of waves by the infinite grating of circular cylinders," *IRE Trans. Antennas Propagat.*, vol. 10, pp. 737-765, Nov. 1962.

[4] M. J. Lockyear, A. P. Hibbins, K. R. White, and J. R. Sambles, "One-way diffraction grating," *Phys. Rev. E* 74, 056611, 2006.

[5] J. M. Lourtioz, A. de Lustrac, F. gadot, S. Rowson, A. Chelnokov, T. Brillat, A. Ammouche, J. Danglot, O. Vanbesien, and D. Lippens, "Toward controllable photonic crystals for centimeter- and millimeter-wave devices," *J. Lightw. Technol.,* vol. 17, no. 11, pp. 2025-2031, Nov. 1999.

[6] A. Scherer, T. Doll, E. Yablonovitch, H. O. Everitt, and J. A. Higgins, "Special section on electromagnetic crystal structures, design, synthesis, and applications," *J. Lightw. Technol.,* vol. 17, no. 11, pp. 1928-2207, 1999.

[7] B. Pradarutti, C. Rau, G. Torosyan, and R. Beigang, "Plasmonic response in a one-dimensional periodic structure of metallic rods," *Appl. Phys. Lett.* 87, 24105, 2005.

[8] K. F. Tsang, L. Mo, and Z. B. Ye, "Analysis of millimeter wave scattering by the infinite plane metallic grating using PCG-FFT technique," *International J. Infrared Millimeter waves*, vol. 24, no. 6, pp. 1005-1022, Jun. 2003.

[9] K. Yasumoto, H. Toyama, and T. Kushta, "Accurate analysis of two-dimensional electromagnetic scattering from multilayered periodic arrays of circular cylinders using lattice sums technique," *IEEE Trans. Antennas Propagat.*, vol. 52, no. 10, pp. 2603-2611, Oct. 2004.

[10] E. Popov and B. Bozhkov, "Differential method applied for photonic crystals," *Appl. Opt.,* vol. 39, no. 27, pp. 4926-4932, 2000.

[11] M. Koshibe, Y. Tsuji, and M. Hikari, "Time-domain beam propagation methods and its application to photonic crystal circuits," *J. Lightw. Technol.*, vol. 18, no. 1, Jan. 2000.

[12] S. F. Halfert and R. Pregla, "Efficient analysis of periodic structures," *J. Lightw. Technol.*, vol. 16, no. 9, Sep. 1998.

[13] H. Jia and K. Yasumoto, "S-Matrix solution of electromagnetic scattering from periodic arrays of metallic cylinders with arbitrary cross section," *IEEE Antennas Wireless Propagat. Lett.*, vol. 3, pp. 41-44, Jan. 2004.

[14] M. Ohki, T. Kurihara, and S. Kozaki, "Analysis of electromagnetic wave diffraction from a metallic Fourier grating by using the T-matrix method," *JEMWA*, vol. 11, pp. 1257-1272, 1997.

[15] M. Ohki, K. Sato, M. Matsumoto, and S. Kozaki, "T-Matrix analysis of electromagnetic wave diffraction form a dielectric coated Fourier grating," *PIER,* vol. 53, pp. 91-108, 2005.

[16] H. A. Kalhor, "EM scattering by an array of perfectly conducting strips by a physical optics approximation," *IEEE Trans. Antennas Propagat.*, vol. 28, no. 2, pp. 277-278, Mar. 1980.

[17] N. P. K. Cotter, T. W. Preist, and J. R. sambles, "Scattering-matrix approach to multilayer diffraction," *J. Opt. Soc. Am. A*, vol. 12, pp. 1097-1103, 1995.

[18] R. Petit, *Electromagnetic Theory of Gratings*, Springer-verlag, New York 1980.

[19] R. Collin, *Field Theory of Guided Waves.* McGraw-Hill, New York, USA, 2nd ed., 1991.

[20] S. Singh, W. F. Richards, J. R. Zinecker, and D. R. Wilton, "Accelerating the Convergence of Series Representing the Free Space Periodic Green's function", *IEEE Trans. Antennas Propagat.*, vol. 38, no. 12, pp. 1958-1962, Dec. 1990.

[21] R. Lampe, P. Klock, and P. Mayes, "Integral Transforms Useful for the Accelerated Summation of Periodic Free-Space Green's Function," *IEEE Trans. Microw. Theory Tech.*, vol. 33, no. 8, pp. 734-736, Aug. 1985.

[22] Y. L. Chow, J. J. Yang, D. G. Fang, and G. E. Howard, "A closed-form spatial Green's function for the thick microstrip substrate," *IEEE Trans. Microw. Theory Tech.*, vol. 39, no. 3, pp. 588- 592, Mar. 1991.

[23] Y. Hua and T. K. Sarkar, "Generalized Pencil-of-Function method for extracting poles of an EM system from its transient response," *IEEE Trans. Antennas Propagat.*, vol. 37, pp. 229-234, 1989.

[24] R. F. Harrington, *Field Computation by Moment Methods.* New York: IEEE Press, 2nd Ed., 1993.

[25] T. Kushta and K. Yasumoto, "Electromagnetic scattering from Periodic Arrays of Two Circular Cylinders per Unit Cell," *PIER*, vol. 29, pp.69-85, 2000.

Hadiseh Alaeian was born in 1984 in Tehran, Iran. She received the B.Sc. and M.Sc. degrees in electrical engineering from the University of Tehran, Iran, in 2004 and 2006, respectively. She is currently a research assistant in the antenna laboratory of the school of Electrical and Computer Engineering at the University of Tehran. Her major areas of interest are electromagnetic bandgap structures and their modeling, meta-materials and THz devices.

Reza Faraji-Dana received the B.Sc. degree (with honors) from the University of Tehran, Tehran, Iran, in 1986 and the M.A.Sc. and Ph.D. degrees from the University of Waterloo, Waterloo, ON, Canada, in 1989 and 1993, respectively, all in electrical engineering. He was a Postdoctoral Fellow with the University of Waterloo for one year. In 1994, he joined the School of Electrical and Computer Engineering, University of Tehran, where he is currently a Professor. He has been engaged in several academic and executive responsibilities, among which was his deanship of the Faculty of Engineering for more than four years, up until summer 2002, when he was elected as the University President by the university council. He was the President of the University of Tehran until December 2005. He is the author of several technical papers published in reputable international journals and refereed conference proceedings.

Prof. Faraji-Dana has been the Chairman of the IEEE-Iran Section since March 2007. He received the Institution of Electrical Engineers Marconi Premium Award in 1995.

Functional Imaging of Compressed Breast by Microwave Radiometry

S. Iudicello and F. Bardati

Dipartimento di Informatica Sistemi e Produzione,
Università di Roma Tor Vergata, via del Politecnico 1,Roma, Italy, 00133

Abstract **–** A tumor is visible by a passive microwave radiometer scanning the breast surface if it changes the radiometer output of a healthy breast to an extent that overcomes the radiometric resolution for the given sensing antenna and integration time. In this paper the breast is intentionally squeezed between the radiometric antenna and the chest wall and the temperature is evaluated for the deformed breast together with the generated radiometric signal. To be compared with the radiometric resolution, the difference signal between the outputs in the presence of a lesion and in its absence has to be evaluated. To achieve this, a mechanical, thermal and electromagnetic model of the breast has been developed. A finite-element code has been used to solve for the mechanical and thermal problems, while FDTD has been exploited for electromagnetic computations. We show that compressing the breast improves the radiometric visibility depending on tumor depth and deformation.

I. INTRODUCTION

In principle microwave radiometry, i.e. passive detection of spontaneous thermal radiation from a body in the microwave frequency band can provide information on the thermal status of tissues to a depth of some centimeters [1]. In clinics, microwave radiometry has been considered in the attempt to cope with two major challenges, i. e. non-invasive temperature monitoring during thermal treatment of extended regions of tissue, and early detection of tumor malignancies. First-type applications have been proposed in [2,3] and, recently, revived in connection with a curtain of radiofrequency radiators for antitumoral hyperthermia treatment of chest wall recurrences [4]. The diagnostic application has been investigated also in connection with the problem of retrieving a temperature profile from a set of radiometric data [5-8]. In spite of some positive evidence, however, microwave radiometry has not yet reached a general consensus as a screening modality for early detection of cancer although recent results seem encouraging [9]. A renewed interest in clinical microwave radiometry can be explained on the basis of the improved performance of both microwave instrumentation and computer modeling of complex systems.

During a typical session a contacting antenna scans the surface of a breast. When a thermal anomaly is located within the radiation solid of the antenna, i. e. the volume of breast that contributes almost all the net real power entering the antenna from the breast, the receiver output increases to some amount. The anomaly is radiometrically visible if such amount is larger than the instrumental resolution. In spite of the simplicity of the underlying rationale, measurements on patients may fail because inadequacies of the instruments and presence of artifacts due to spurious radiation. When the antenna explores the breast, in fact, the data may vary because any change in the antenna match causes a variation in the back reflection of thermal noise from the receiver. An ideal radiation-balance radiometer [10] prevents this drawback. Moreover, the increment in received power due to a visible thermal anomaly must overcome the floor power due to thermal emission from normal tissue. A parametric study on the radiometric visibility of thermal anomalies has been presented in [11] for an elementary antenna consisting of a circular aperture in a perfectly conducting screen. An improved model of breast, which includes a portion of chest and a skin layer, has been considered in [12]. The results of these investigations show that a 10mm spherical lesion is radiometrically visible by a system with 0.1 C° resolution if it is not deeper than 2.5cm. When a contacting sensor is scanned on the breast a pressure is normally exercised. The breast is deformed so that the distance of a lesion from the contacted surface is lowered while its visibility is changed. While breast flattening has been treated as a negligible effect in the modeling by previous authors, in this paper the breast is intentionally squeezed between antenna and thorax and we estimate the thermal behavior and the corresponding radiometric signal for the deformed breast. Breast compression is routinely performed during compression mammography to an extent that is indicated by regulatory agencies [13].

For the signal S in output to a radiation balance microwave radiometer we shall use,

$$S = \int_{\Omega} W(\underline{r}) T(\underline{r}) dV \qquad (1)$$

where W is called weighting function, T is the physical temperature and Ω is the overall volume that is sensed by the antenna. Due to reciprocity in antenna theory W can be obtained as,

$$W(\underline{r}) = \frac{P_d(\underline{r})}{\int_{\Omega} P_d(\underline{r}) dV} \tag{2}$$

where $P_d(\underline{r})$ is microwave power deposition at point $\underline{r} \in \Omega$ when the antenna radiates onto the body in active modality [14]. The presence of a malignancy may result in an excess of temperature ΔT as well as in a change ΔP_d within Ω, due to a change in permittivity of tumor tissue with respect to normal tissue. The radiometric resolution (sensitivity) will be denoted by δS. In the next Section the breast deformation due to a compression exercised normally to the chest wall will be studied, while the thermal and electromagnetic models that are necessary to estimate S will be presented in Section III. The mechanical and thermal problems have been solved in a finite-element frame using the commercial tool COMSOL Multiphysics [15]. The electromagnetic problems have been solved by FDTD using a proprietary code. Preliminary results will be presented showing the increase in visibility that are consequent to breast compression.

II. BIOMECHANICAL MODEL

To evaluate the radiometric signal the mechanical, thermal and electromagnetic properties of the breast must be specified for each tissue component. The normal breast consists of a tree-like structure of glandular tissue supported by connective tissue, immersed in fat and surrounded by skin. However, to simplify the problem, we model the breast as a homogeneous hemisphere supported by a square box of muscle (Fig. 1). Assuming that the breast is made of an equal amount of fat and glandular tissue, the homogeneous model results from averaged mechanical properties.

To model the breast deformation under compression, a simulation model, which can handle large deformations and nonlinear, nearly incompressible materials, must be implemented. In literature breast-deformation modeling is receiving attention due to the need of data fusion from X-ray mammography in different views and Magnetic Resonance Imaging in early cancer diagnostics as well as to achieve suitable information for surgery or needle insertion during a biopsy [16-20]. Biological tissues have been shown to exhibit non-linear stress-strain laws [21, 22] and this is the case for the range of strains involved during mammographic screens. Different material models for breast tissues are proposed in the literature. A review of strain-stress relationships can be found in [17]. The resulting stress for a given strain is largely dependent on the model, while a criterion for model validation can be the plausibility of the achieved deformation in the comparison with experimental outcomes. E.g. in [23] the displacement of a set of landmarks positioned on a patient has been measured for increasing net deformation. The exponential models are more accurate than linear and neo-hookean ones in retrieving large breast deformation. However, as a drawback, they originate non-realistic compression forces [23,24].

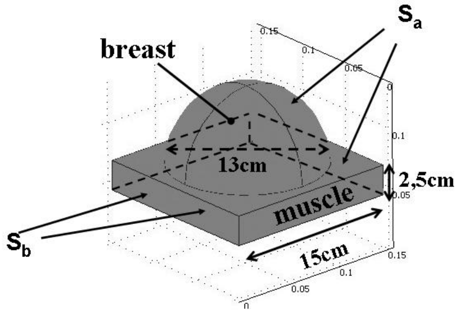

Fig. 1. Hemispherical model of undeformed breast on a muscle box.

The kinematic problem is to find the coordinates $\underline{x}$ of the deformed body, given the coordinates $\underline{X}$ of the undeformed body. The displacement vector and the Green-Lagrange strain tensor are respectively defined as,

$$\underline{U} = \underline{x} - \underline{X} \tag{3}$$

$$E_{ij} = \frac{1}{2}\left(\frac{\partial U_i}{\partial X_j} + \frac{\partial U_j}{\partial X_i} + \frac{\partial U_k}{\partial X_i}\frac{\partial U_k}{\partial X_j}\right) \tag{4}$$

where summation over repeated indices is intended. The deformation gradient tensor $F_{ij} = \partial x_i / \partial X_j$ is introduced. The Second Piola-Kirchoff tensor, T_{mn}, is generally used as stress definition in large deformation problems. T_{mn} is defined as the force acting on the undeformed body measured per unit undeformed area. In an equilibrium deformed state, all forces must balance, and it can be shown that this leads to,

$$\frac{\partial}{\partial X_m}\left(T_{mn}\frac{\partial x_i}{\partial X_n}\right) + f_i = 0, \quad (i = 1, 2, 3) \tag{5}$$

where f_i is volume external force component per unit volume. To relate stress to strain, a strain energy function $W(E_{ij})$ is assumed to exist. The principle of virtual works allows the equilibrium problem (5) to be reformulated as an energy minimization problem. We have made the assumption that the tissue is isotropic. If a material is isotropic, the strain-energy density function W can be in general expressed as a function of the strain invariants I_1, I_2, I_3 where $I_1 = tr(F_{ij}^T F_{ij})$ and ^{T} is for transposed. $I_3 = J^2$, with J volume ratio. $J = 1$ for a perfectly incompressible material. Practically, tissues have a Poisson's ratio that ranges from 0.49 to 0.5. The Poisson's ratio for the tissue used in this study is 0.498. We assumed an exponential constitutive law [18],

$$W = a(e^{b(I_1-3)} - 1) - \frac{p}{2}(I_3 - 1) \qquad (6)$$

where a and b are average fit parameters between fat and glandular tissue calculated from uniaxial stress-strain experiments using a tissue sample [25], p is the internal pressure that represents a Lagrangian multiplier introduced to impose the constraint $I_3 - 1 = 0$.

Finally, the mechanical boundary conditions must be specified to obtain the solution. We admit that the radiometric antenna is frontally pressed against the breast, which is squeezed between the planar antenna and the thorax plane, coincident with the pectoral muscle wall. The two planes are parallel. The muscle wall is fixed. Zero displacement on the muscle wall in contact with the breast and zero pressure on the free skin surface are suitable boundary conditions. The antenna itself has been modeled as a compression plate with the mechanical coefficients of aluminum. At the interface between antenna and breast a non-penetration condition holds [18]. Owing to this condition the breast modeling under compression is not a standard elasticity problem. Let D be the distance of the antenna plate from the chest wall. The compression plate is supposed to move in the direction of the z-axis, towards the chest. D equals the hemisphere radius R in the undeformed configuration, when the plane is contacting the breast at a single point (Fig. 2(a)). During compression D is reduced while the plate/breast contact area increases (Fig. 2(b)). If the total displacement of the plate is C, then the relative net deformation is $C/R=(R-D)/R$. The following numerical analysis will be performed for a net deformation of 35%, which is between the limit values of mammography (20-50%). In order to model such a large deformation we divided C into N small displacements. Then we solved N linear deformation problems as a sequence of steps. At the end of each step, we know the flattened breast surface in contact with the antenna. However, we don't know 'a priori' which additional surface the antenna will contact as a consequence of the deformation at the next step. The problem of determining the additional contact surface of a deformable body under compression is known as a contact analysis problem. It has been formulated and solved as an Augmented Lagrangian optimization [26].

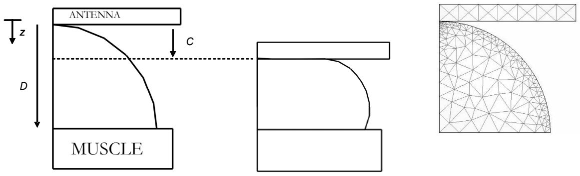

(a) (b) (c)

Fig. 2. a) Geometry of the undeformed breast, sagittal view. b) Geometry of the deformed breast. c) Undeformed breast. Partition into triangular elements.

Due to axial symmetry a quarter of the structure has been modeled, therefore the further condition of zero displacement normally to the symmetry walls has been introduced. The finite-element mesh consists of 15150 tetrahedral elements, 14620 for the breast and 530 for the compression plate. A view of the partition into elements is shown in Fig. 2(c). Mesh density is higher near the initial point of contact between the breast and the antenna while an element size of 2.5 mm is specified on the breast external surface. To solve for the non-linear mechanical behavior, after a small displacement increment of the compression plate, the internal pressure is computed together with the displacement at each point.

In mammography breast deformation studies, the relative reduction of a breast diameter is imposed, while the net force between the plates is computed from the resulting stress. The diagram in Fig. 2(b) refers to a breast deformation of about 35% for frontal compression. The compression force results in about 1750 *N*. As expected, this value is larger than the net force experienced in X-ray mammography, which ranges between 49 and 186 *N* [24]. In Fig. 3 the displacement is shown versus particle depth in the undeformed state on a sagittal plane. The displacement is practically linear with depth, with 35% slope.

We modeled a tumor as a sphere. In this preliminary work the sphere is located on the symmetry axis (z-axis) perpendicular to the chest wall. Tumor-center distance from the antenna contact point in the undeformed state is referred to as tumor depth. For simplicity the mechanical properties of the tumor have been taken coincident with those of the host tissue. After frontal compression the sphere is deformed into an ellipsoid whose axes can be estimated using the diagram in Fig. 3 for the displacements of the tumor-diameter end-points along the *z*-axis, while the two other axes are found by tumor volume conservation.

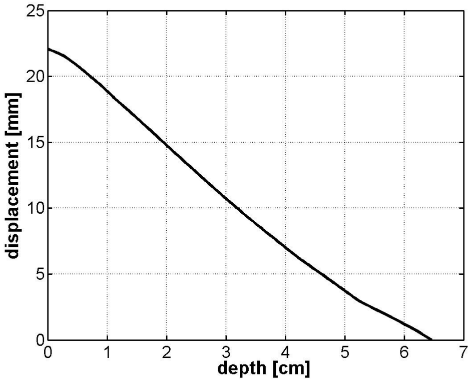

Fig. 3. Particle displacement vs. depth on *z*-axis.

III. THERMALAND ELECTROMAGNETIC MODELS

We assume the temperature satisfies the steady-state bio-heat equation,

$$\nabla\cdot\kappa\nabla T + q_m - \rho_b c_b w_b (T - T_b) = 0 \qquad (7)$$

where κ is the effective thermal conductivity which includes the enhancement in conductivity due to blood perfusion, qm is the metabolic heat generation rate, c_b is the specific heat, ρbwb is the blood perfusion rate per unit mass of tissue and T_b is the arterial blood temperature. The boundary condition at the interface S_a between breast and air is,

$$\kappa\nabla T\cdot\hat{n}_a + h_a (T - T_a) = 0 \qquad (8)$$

with $\hat{n}_a$ the unit vector normal to the boundary, h_a a heat transfer coefficient, and T_a the air temperature. T is continuous at the interface between breast and pectoral muscle. We assume an adiabatic condition $\partial T/\partial n=0$ at the boundary S_b with the main body. The solution $T(\underline{r})$ to equations (7) and (8) is diagrammed in Fig. 4(a) on a sagittal plane for the geometry of Fig. 2.

In previous work [11,12] the contact between antenna and breast was ideally confined to a small area and to a very short time interval, in such a way to neglect temperature variations in the breast due to the soft contact with the antenna. Two limiting cases can be envisaged in the presence of large deformations. In a first case the antenna is instantaneously compressed against the breast, while the radiometer takes the data in that instant. No heat exchanges are allowed, so that the temperature of a particle at a point $\underline{\boldsymbol{x}}$ in the compressed state coincides with its temperature at the initial location $\underline{\boldsymbol{X}}$ in the undeformed state (Fig. 4(b)). We shall refer to this temperature as adiabatic temperature. In a second case, the radiometric data acquisition takes enough time (about 15 minutes as shown in Fig. 5) to let the temperature reach the steady state within the deformed breast in the presence of a larger contact surface between antenna and breast (Fig. 4(c)). We shall refer to this temperature as steady-state temperature. We expect that the temperature that is sensed by the antenna during a realistic measurement be between these limiting cases. The heat transfer coefficient is assumed h_a=13.5 W/(m^2·K) [27], at the breast/air interface. At the boundary between antenna and breast, equation (8) still holds, with a heat transfer coefficient h_a=135 W/(m^2·K), i.e., ten times the coefficient for the air/breast interface. The antenna is supposed to be kept at a reference temperature T_a, by circulating de-ionized water.

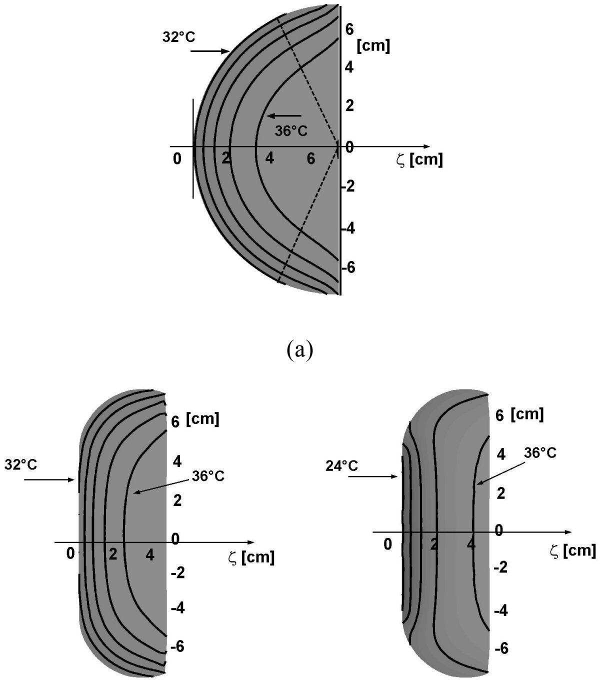

(a)

(b) (c)

Fig. 4. a) Isotherms (step 1°C) on a sagittal plane for undeformed normal breast. b) Isotherms (step 1°C) for deformed normal breast in the adiabatic case. c) Isotherms (step 3°C) for deformed normal breast in the steady-state case. For normal breast: κ=0.48W/m·°C, q_m=700 W/m^3, ρ_b=1060 Kg/m^3, c_b=2600 J/Kg·°C, w_b=0.00054 s^{-1}. For muscle: κ=0.48 W/m·°C, q_m=700 W/m^3, w_b=0.0008 s^{-1}. T_a=20°C, T_A=20°C, T_b=37°C.

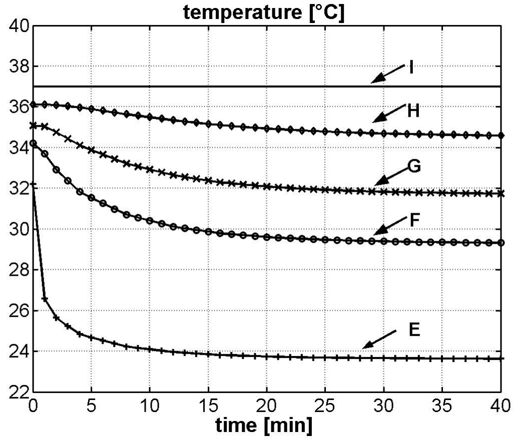

Fig. 5. Temperature T vs. time at the points labeled as in Fig. 2(b). The curves start for t=0 from the adiabatic values.

A tumor may change *T(r)* into a new temperature *T'(r)* differing by *ΔT(r)* from the normal breast temperature mainly in the tumor volume and in the surrounding tissue. Thermogenesis and angiogenesis are considered responsible for this change [28]. Thermogenesis is accounted for by a value qm that is related to the tumor doubling time by a hyperbolic law, while the tumor size is exponentially related to the doubling time [29]. Diagrams of *ΔT* vs. lesion depth are shown in Fig. 6 along a line through the lesion center, for a 10 mm tumor centered at 1cm, 2cm, 3cm and 4cm from the surface, in the adiabatic and steady-state cases. The tumor depth is the tumor-center distance from the surface before compression.

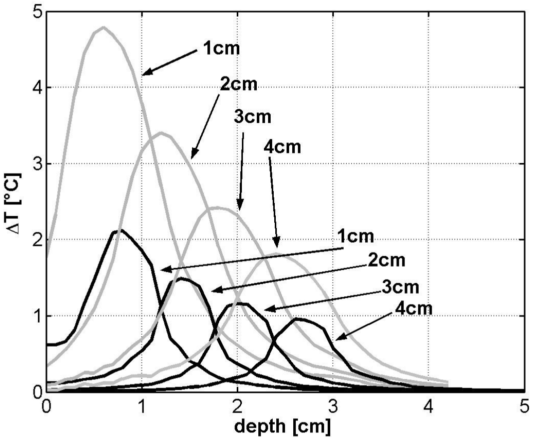

Fig. 6. Temperature difference (unhealthy-normal) *ΔT* for a 10mm lesion and compressed breast. Steady-state (gray line) and adiabatic (bold line) temperatures. Tumor parameters: κ_t=0.511 W/m·°C, q_{mt}=65400 W/m^3, w_{tb}=0.01 s^{-1} [27].

From the diagrams in Fig. 4 we observe that the breast peripheral temperature is lower for steady-state because of the more effective superficial cooling forced by the contacting antenna. Therefore the tumor steady-state over temperature *ΔT* is higher than the adiabatic one as shown in Fig. 6.

For the sake of generality we shall not specify any particular radiometric antenna letting the size be its only characteristic feature. The electromagnetic model consists of a circular aperture of diameter *2a*, center at $z = 0$, in an infinite conducting plane. We assume the half-space in front of the aperture is filled by breast tissue. Accounting for the heterogeneity of breast tissue is a difficult task since the adipose tissue is inseparably intermixed with fibroglandular parenchyma (except in the subcutaneous region) [30,31]. For simplicity we assume a homogeneous medium with dielectric properties as in [11,32]. We refer to [33] for tumor dielectric properties. Recently, the dielectric properties of normal and malignant breast tissues have been experimentally characterized in the microwave frequency range by Lazebnik *et al.* [34,35]. Basing on the percentage of adipose tissue content, they classified samples of normal breast into three groups. The dielectric properties we adopted for normal breast are similar to those in the third group in [34] (85-100% adipose tissue content).

The field is radiated by a uniform linearly-polarized electric field $\underline{E}_a$ on the aperture. The center-band frequency is 2.6 GHz, which is close to widely used frequencies in medical application of microwave radiometry [4], [36-39]. Electromagnetic field computations have been performed by a proprietary FDTD code using Mur absorbing boundary conditions at the walls. The FDTD computation has been repeated in the presence of the spherical lesion with its center at various depths. Contour-level plots of P_d are shown on two orthogonal principal planes in Fig. 7.

IV. RESULTS

The radiometric signal *S* has been computed by equation (1) after the temperature and power $\boldsymbol{P}_d$ delivered to tissue have been determined within both normal and unhealthy breast. Denote the difference between unhealthy and normal breast signals by *ΔS*,

$$\Delta S = \int_{\Omega} W'(\underline{r})T'(\underline{r})dV - \int_{\Omega} W(\underline{r})T(\underline{r})dV \qquad (9)$$

where the prime is used for the unhealthy breast. Therefore *ΔS* is a useful parameter in breast tumor detection by microwave radiometry. Diagrams of *ΔS* are shown in Fig. 8 as a function of tumor depth and refer to non-compressed breast. The two curves have been obtained from two different sets of dielectric parameters for comparison. Significant differences cannot be appreciated between the two diagrams. This is due to the fact that *ΔS* is slightly dependent on the dielectric contrast between malignant and normal tissue, which is lower for the second group of dielectric properties, while it mainly depends on the over-temperature localized in the tumor volume [11].

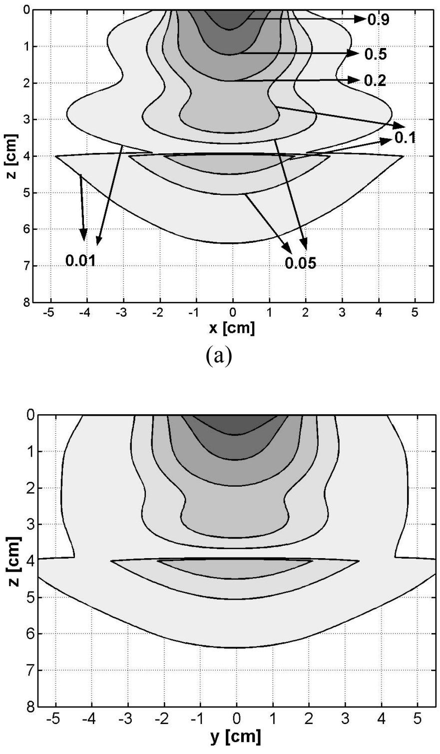

(a)

(b)

Fig. 7. Contour-level diagrams of $P_d=1/2\ \sigma\ |E|^2$ on the principal plane perpendicular a) and parallel b) to the aperture field, respectively. For normal breast: $\varepsilon_{rb}=10$, $\sigma_b=0.2$ *S/m*, for muscle : $\varepsilon_{rm}=50$, $\sigma_m=1.5$ *S/m* [32].

The diagrams in Fig. 9(a) refer to the compressed breast and to the adiabatic (bold line) and steady-state (gray line) temperatures. A realistic curve for *ΔS* lies between these diagrams. A tumor is radiometrically visible if the difference signal overcomes the resolution, i.e. $\Delta S>\delta S$ is the condition for a tumor to be visible. A reference value can be $\delta S=0.1$°C with 1s integration time. We conclude that the visibility of a 10mm tumor increases passing from about 25mm (Fig. 8) in the undeformed breast to a value between 30mm and 38mm in the deformed breast and 35% net deformation if the dielectric parameters are chosen as in [11] (between 30 and 45mm with parameters in [34, 35], Fig. 9(b)). *ΔS* is greater when the second group of parameters is considered due to the shift of the maximum of P_d, as shown in Fig. 10.

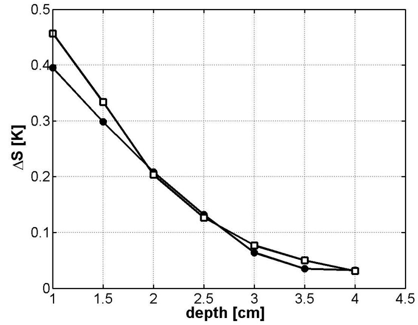

Fig. 8. Difference radiometric signal (unhealthy-normal) of a 10mm lesion vs. depth and a 3cm aperture antenna for non-compressed breast. The line with circles refers to $\varepsilon_{rb}=10$, $\sigma_b=0.2$ *S/m* for normal breast and $\varepsilon_{rb}=50$, $\sigma_b=1.5$ *S/m* for malignant breast, as in [11], while the line with diamonds refers to $\varepsilon_{rb}=39$, $\sigma_b=1.18$ *S/m* for normal breast [34] and $\varepsilon_{rb}=55$, $\sigma_b=2$ *S/m* for malignant breast [35].

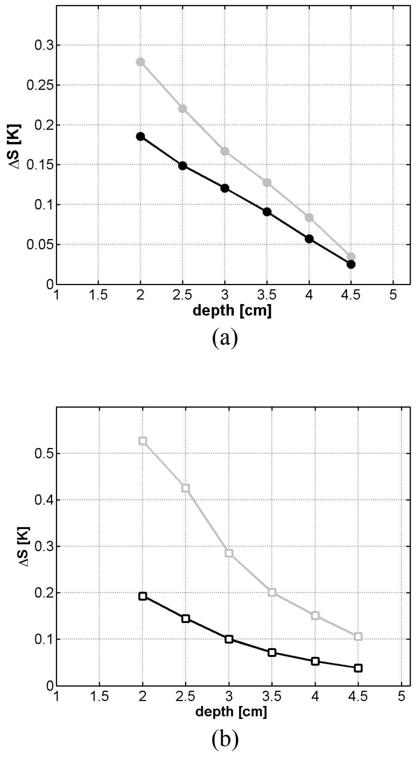

(a)

(b)

Fig. 9. Difference radiometric signal *ΔS* (unhealthy-normal) of a 10mm lesion vs. depth and a 3cm aperture antenna for compressed breast: adiabatic temperature (bold line), steady-state temperature (gray line). Dielectric parameters a) as in [11], b) as in [34,35]. 35% net deformation.

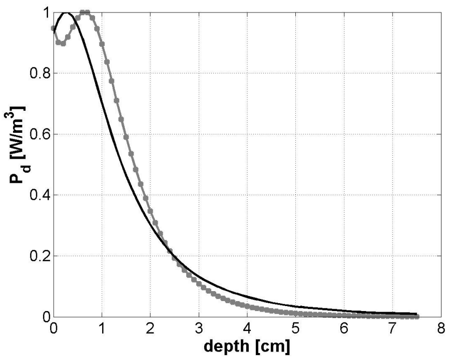

Fig. 10. Normalized P_d along the z-axis passing through the center of a 3cm aperture for undeformed breast. Dielectric parameters (bold line) as in [11], (gray line) as in [34].

V. CONCLUSION

The problem of estimating the visibility of a breast tumor by a passive radiometric device has been addressed when the sensing antenna is pressed against the breast. A mechanical and thermal model of the breast under compression by the contacting antenna has been developed, based on the data available in the literature. The mechanical behavior has been modeled by a non-linear constitutive equation, while the temperature satisfies the classical bio-heat equation. Both problems have been solved in a finite-element frame. The thermal radiation that is received by an ideal radiation-balance radiometer has been estimated solving the electromagnetic problem of antenna radiation onto the breast. According to the results of the numerical analysis, the excess in radiometric signal due to a 10mm tumor overcomes a typical radiometric resolution to a depth between 3 and 4 cm in the case of 35% compression. The above analysis has assumed that the tissue mechanical, thermal and electric properties are uniform within the normal breast.

REFERENCES

[1] F. Bardati and D. Solimini, "Radiometric sensing of biological layered media," *Radio Sci.*, vol. 18, no. 6, pp. 1393-1401, 1983.

[2] F. Sterzer, P. Paglione, F. Wozniak, J. Mendecki, E. Friedenthal, and C. Botstein, "Self-balancing microwave radiometer for non-invasively measuring the temperature of subcutaneous tissue during localized hyperthermia treatments of cancer," *IEEE MTT-S Int Microwave Symp Digest*, vol. 82, no. 1, pp. 438-440, 1982.

[3] M. Chivè, M. Plancot, Y. Leroy, G. Giaux, and B. Prevost, "Microwave (1 and 2.45 GHz) and radiofrequency (13.56 MHz) hyperthermia monitored by microwave thermography," *12th European Microwave Conf*, Helsinki (Finland), Sept. 1982.

[4] S. Jacobsen, P. Stauffer, and D. Neuman, "Dual-mode antenna design for microwave heating and non-invasive thermometry of superficial tissue disease," *IEEE Trans Biomed. Eng.*, vol. 47, no. 11, pp. 1500-1509, 2000.

[5] C. Gros, M. Gautherie, and P. Bourjat, "Prognosis and post-therapeutic follow-up of breast cancers by thermography," *IEEE Trans Biomed Eng*, vol. 6, pp.77-90, 1975.

[6] J. Edrich, "A millimeter-wave thermography for human breast and spine scans," *6th European Microwave Conf*, Rome, pp. 137-140, Sept. 1976.

[7] A. H. Barret, P. C. Myers, and M. L. Sadowsky, "Detection of breast cancer by microwave radiometry," *Radio Sci.*, vol. 12, no. 6(S), pp. 167, 1977.

[8] K. L. Carr, A. M. El-Mahdi, and J. Shaffer, "Dual-mode microwave system to enhance early detection of cancer," *IEEE Trans Microwave Theory Tech*, vol. 29, no.3, pp. 256-260, 1981.

[9] J. W. Lee, S. M. Lee, K. S. Kim, W. T. Han, G. Yoon, L. A. Pasmanik, I. A. Ulyanichev, and A. V. Troitsky, "Experimental investigation of the mammary gland tumor phantom for multifrequency microwave radio-thermometers," *Med Biol Eng Comput*, vol. 42, no.5, pp. 581-590, 2004.

[10] K. M. Ludeke, J. Kohler, and J. Kanzenbach, "A new radiation balance microwave thermograph for simultaneous and indipendent temperature and emissivity measurements," *J Microwave Power*, vol. 14, pp. 117-121, 1979.

[11] F. Bardati and S. Iudicello, "Modeling the visibility of breast malignancy by a microwave radiometer," to be published on *IEEE Trans. Biomed. Eng.*

[12] F. Bardati and S. Iudicello, "Modeling functional imaging of breast by microwave radiometry," *ACES Conference*, Verona, Italy, pp. 871-875, 19-23 Mar. 2007.

[13] "The European Protocol for the Quality Control of the Physical and Thecnical Aspects of Mammography Screening." CEC Report EUR 14821, 3rd edn 1999. http://ikrweb.uni-uenster.de/aqs/Richtlinien /qualitaet_mammo/qualitaet_mammo.html

[14] G . M. J. Van Leeuwen, J. W. Hand, J. B. Van de Kamer, and S. Mizushina, "Temperature retrieval algorithm fro brain temperature monitoring using microwave brightness temperatures," *Electronics Letters*, vol. 37, no. 6, pp. 341-2, 2001.

[15] COMSOL, www.comsol.com, Version 3.3a.

[16] A. Samani, J. Bishop, M. J. Yaffe, and B. Plewes, "Biomechanical 3-D finite element modeling of the human breast using MRI data," *IEEE Transactions on Medical Imaging*, vol. 20, no. 4, pp. 271-279, 2001.

[17] N. V. Rviter, T. O. Muller, R. Stotzka, H. Gemmeke, J. R. Reichenba, and W. A. Kaiser, "Automatic image matching for breast cancer diagnostics by a 3D deformation model of the Mamma," *Biomed. Tech.* (Berl), 47 Suppl1 Pt2, pp. 644-7, 2002.

[18] P. Pathmanathan, D. Gavaghan, J. Whiteley, S. M. Bredy, M. Nash, P. Nielsen, and V. Rajagopal, "Predicting tumor location by simulating large deformations of the breast using a 3D finite element model and nonlinear elasticity," *Proc. MICCAI2004, LNCS3217, Springer-Verlag,* pp. 217-224, 2004.

[19] V. Rajagopal, P. M. F. Nielsen, and M. P. Nash, "Development of a three dimensional finite element model of breast mechanics," *Proceedings of the 26th Annual*

International Conference of the IEEE EMBS, San Francisco, CA, USA, 1-5 Sept. 2004.

[20] N. V. Ruiter, R. Stotzka, T. O. Muller, H. Gemmeke, J. R. Reichenbach, and W. A. Kaiser, "Model-Based registration of X-Ray Mammograms and MR images of the female breast," *IEEE Transactions on Nuclear Science*, vol. 53, no. 1, pp. 204-211, Feb. 2006.

[21] V. Vuskovic and M. Kauer, "In vivo-measurement of elasto mechanical properties of soft biological tissue," in *European Medical and Biological Engineering Conference*, Vienna, Austria, 1999.

[22] R. D. Howe, "Identification of constitutive nonlinear constitutive law parameters of breast tissue," in *Summer Bioengineering Conference*, Vail, Colorado, 22-26 June 2005.

[23] N. Ruiter, "Registration of X-Ray Mammograms and MR-volumes of the female breast based on simulated Mammographic deformation." *PhD thesis*, pp. 55-74, University of Mannehim, 2003.

[24] D. C. Sullivan, C. A. Beam, S. M. Goodman, and D. L. Watt, "Measurement of force applied during Mammography," *Radiology*, vol. 181, no. 2, pp. 355-357, 1991.

[25] P. Wellman, R. D. Howe, E. Dalton, and K. A. Kern, "Breast tissue stiffness in compression is correlated to histological diagnosis," *Tech. Rep.*, Harward BioRobotics Laboratory, Harward University, Cambridge, Mass, USA, 1999.

[26] A. R. Mijar, J. S. Arora, "An Augmented Lagrangian optimization method for conact analysis problem, 1: formulation and algorithm," Struct Multidisc Optim, vol. 28, pp. 99-112, 2004.

[27] E. Y. K. Ng and N. M. Sudharsan, "An improved three dimensional direct numerical modeling and thermal analysis of a female breast with tumor," *Proc. Instn Mech Engrs*, vol. 215, no. 1, pp. 25-37, 2001.

[28] T. Yahara, T. Koga, S. Yoshida, S. Nakagawa, H. Deguchi, and K. Shirouzu, "Relationship between microvessel density and thermographic hot areas in breast cancer," *Surg Today*, vol. 33, pp. 243–248, 2003.

[29] M. Gautherie, Y. Quenneville, and C. M. Gros, "Metabolic heat production growth rate and prognosis of early breast carcinomas," *Biomedicine*, vol. 22, pp. 328–336, 1975.

[30] W. B. Nickell, J. Skelton, "Breast fat and fallacies: more than 100 years of anatomical fantasy," *J of Hum Lact*, vol. 21, no. 2, pp. 126-130, 2005.

[31] N. A. Lee, H. Rusinek, J. Weinreb, R. Chandra, H. Toth, C. Singer, and G. Newstead, "Fatty and Fibroglandular tissue volumes in the breast of women 20-83 years old: comparison of X-Ray Mammography and computer-assisted MR imaging," *AJR*, vol. 168, no. 2, pp. 501-6, 1997.

[32] S. Gabriel, R. W. Lau, and C. Gabriel, "The dielectric properties of biological tissues: II. Measurements in the frequency range 10 Hz to 20 GHz ," *Phys. Med. Biol.*, vol.41, no. 41, pp. 2251-2269, 1996.

[33] X. Li and S. C. Hagness, "A confocal microwave imaging algorithm for breast cancer detection," *IEEE Microwave Wireless Compon. Lett.*, vol. 11, no. 3, pp. 130–132, Mar. 2001.

[34] M. Lazebnik, L. McCarteney, D. Popovic, C. B. Watkins, M. J. Lindstrom, J. Harter, S. Sewall, A. Magliocco, J. H. Booske, M. Okoniewsky, and S. C. Hagness, "A large-scale study of the ultrawideband microwave dielectric properties of normal breast tissue obtained from reduction surgeries," *Phys. Med. Biol.*, vol. 52, pp. 2637-2656, 2007.

[35] M. Lazebnik, L. McCarteney, D. Popovic, L. McCarteney, C. B. Watkins, M. J. Lindstrom, J. Harter, S. Sewall, T. Ogilvie, A. Magliocco, T. M. Breslin, W. Temple, D. Mew, J. H. Booske, M. Okoniewsky, and S. C. Hagness, "A large-scale study of the ultrawideband microwave dielectric properties of normal, benign and malignant breast tissues obtained from cancer surgeries," *Phys. Med. Biol.*, vol. 52, pp. 6093-6115, 2007.

[36] B. Bocquet, A. Mamouni, M. Hochedez, J. C. Van de Velde, and Y. Leroy, "Visibility of local thermal structures and temperature retrieval by microwave radiometry," *Elettronics Letters*, vol. 22, no. 3, pp. 120–121, 1986.

[37] P. C. Myers, N. L. Sadowsky, and A. H. Barrett "Microwave Thermography: Principles, Methods, and Clinical Applications," *J. Microwave Power*, vol. 14, no. 2, pp. 105-115, 1979.

[38] D. V. Land, S. M. Fraser, and R. D. Shaw "A review of clinical experience of microwave Thermography," *J. Med. Eng. Tech.*, pp. 109-113, 1986.

[39] S. Mizushina, Y. Hamamura, and T. Sugiura "A three-band microwave radiometer system for noninvasive measurement of the temperature at various depths," *IEEE MTT-S Digest.*, vol. 86, no. 1, pp. 759-762, 1986.

Santina Iudicello received the M.S. degree in medical engineering from the Universita di Roma Tor Vergata, Italy, in 2005. She currently is a PhD student with interests in the microwave and radiofrequency techniques for diagnosis and therapy of breast cancer.

Fernando Bardati was born in Rome, Italy, in 1941. He received the Laurea in Electronic Engineering (in 1965) and the Libera Docenza in Microwaves from the University of Rome in 1971. He was Assistant/Associate Professor of Electronics and of Electrical Measurement at the Universities of L'Aquila and Rome from 1973 to 1985. He currently is Full Professor of Electromagnetic Fields at the University of Rome Tor Vergata. In 1995 he was a visiting professor at the Oncological Department of the University of Arizona in Tucson. From 1980 he worked in medical applications of microwaves, such as antitumoral hyperthermia and the inverse problem of microwave radiometry. He has been involved with research in electromagnetic field propagation modeling in complex environments. His current research is focused on the development of a new generation clinical radiometer for temperature monitoring during thermal treatments and for early cancer diagnosis.

Analysis and Estimation of Surge Impedance of Tower

[1] M. O. Goni and [2] A. Ametani

[1]Dept. of Electronics and Communication Engineering, Khulna University of Engineering and Technology, Khulna-9203, Bangladesh. E-mail:osman@ieee.org
[2]Faculty of Engineering, Doshisha University, Kyoto, Japan. E-mail: aametani@mail.doshisha.ac.jp

Abstract **–** Different mathematical formulas and analytical values of surge impedance of communication tower including high voltage transmission and distribution tower are presented. Those values and formulas have been utilized since 1934. Recently, the surge impedance of communication tower under the influence of direct and indirect lightning hit has drawn a lot of attention. Such value of lightning surge impedance and its associated parameters are becoming important factors for the protection system design in substation as well as low voltage communication equipments including home appliances.

I. INTRODUCTION

Several models have been proposed to estimate the surge impedance of vertical structures (tower), following either a transmission line [1-6], a numerical electromagnetic [7, 8], or an experimental approach [9-12], though in some cases, more than one approach is used [13-16]. Jordan, in 1934, published one of the precursor works in this field [1]. Jordan's formula to calculate the surge impedance of vertical conductors remained as the main reference to estimate the transient behavior of transmission towers subjected to lightning currents until the proposition of new theories in the 1960s (e.g.,[2,3]). It was later found that Jordan's derivation contained a mistake and a correction was proposed [17].

Recently, the interaction of lightning with elevated strike objects has been attracting a lot of attention in the scientific community (e.g.,[18-24]). As a consequence, the development of simplified models to simulate transients in vertical metallic structures has gained importance. In this context, the equations and values of surge impedance derived theoretically or measured experimentally appear to be very promising, because they give insightful information for the designing and installing protection system against lightning surge.

This paper presents investigation on surge impedance of an elevated structure with simple approximation to the shape of structure. Different expressions for the time-domain surge impedance that are usually adopted for characterization of the transient behavior of towers are dependent on the excitation waveshape. This paper also summarizes the methods of excitation that have been considering in a lightning surge analysis by the technical community.

II. JORDAN'S ORIGINAL FORMULA FOR TOWER SURGE IMPEDANCE

The surge impedance of a tower can be approximated by considering the tower as a vertical cylinder having a length equal to the height above the ground plane of the actual tower, and a radius equal to the mean equivalent radius of the actual tower [1]. This equivalent cylinder should also be regarded as having its base located at the same elevation above the true ground plane as the ground-line base of the actual tower. In accordance with the theory of images, there should be conceived as associated with the equivalent cylinder an identical image cylinder located symmetrically with respect to the true ground plane. For such a system, it can be shown that the inductance of an element *dy* of the tower equivalent cylinder as shown in Fig. 1(b), at an elevation *y* above the true ground plane is,

$$dL = [\ \log_e \frac{\sqrt{(h+a-y)^2 + r^2} + (h+a-y)}{\sqrt{(h+a+y)^2 + r^2} + (h+a+y)} + \log_e \frac{\sqrt{(a+y)^2 + r^2} + (a+y)}{\sqrt{(a-y)^2 + r^2} + (a-y)}\ ]\ dy, \qquad (1)$$

where h = length of tower equivalent cylinder (height of tower above ground plane).
r = radius of tower equivalent cylinder (mean equivalent radius of tower).
a = depth of true ground plane below earth's surface.

Integrating equation (1) between the limits $y = h + a$ and $y = a$, dividing by *h*, multiplying by the speed of light to convert from inductance to impedance (as $Z = Lc\ \ \Omega$, $c = 1/\sqrt{LC}$ = speed of light), and finally simplifying, the mean value of surge impedance over the cylinder equivalent to tower is, [1]

1054-4887 © 2009 ACES

$$Z_s = 138.2\ \left[\ \log_{10}\frac{h(h+2a)}{r(h+a)} + \frac{a}{h}\log_{10}\frac{(h+2a)^2}{(h+a)(2a+\sqrt{4a^2+r^2})}\right] + \frac{30}{h}\left[\sqrt{4a^2+r^2} - 2(h+a-r)\ \right]\ \ \Omega. \tag{2}$$

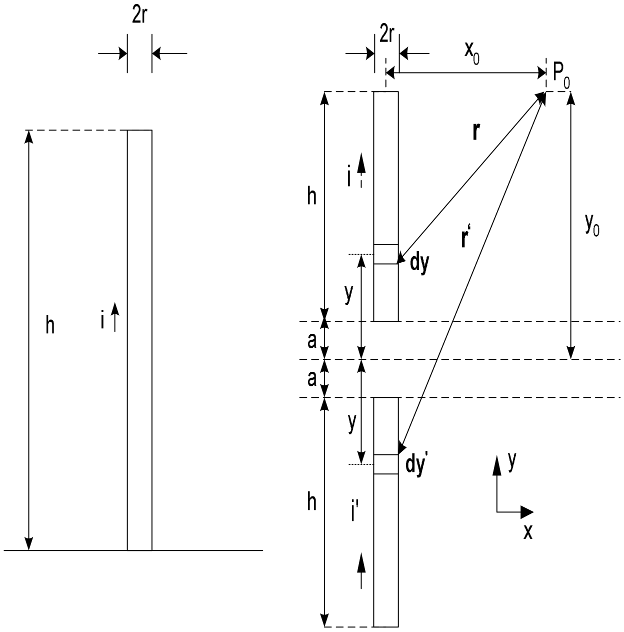

(a) (b)

Fig. 1. Vertical conductor system. (a) Original system. (b) Equivalent representation.

For the special case where the depth of true ground plane below the earth's surface (e.g. *a* as in Fig. 1(b)) is close to zero, then equation (2) reduces to the comparatively simple expression, [1]

$$\begin{aligned} Z_s &= 138.2\ \log_{10}\frac{h}{r} + 90\frac{r}{h} - 60\ \ \Omega \\ &= 60\ \ln\frac{h}{r} + 90\frac{r}{h} - 60\ \ \Omega. \end{aligned} \tag{3}$$

The equivalent radius for a complex structure such as GSM tower, high voltage transmission tower etc. is difficult to compute precisely. At the outset, it is necessary to disregard the cross arms, and confine attention to the tower mast and hence, the expression, $r = \text{perimeter of section}/2\pi$ offers one method of approximating the equivalent radius [1]. Thus for square tower sections having a face width *A*, the equivalent radius would be $r = 4A/2\pi = 0.637A$; for triangular sections with face width A, the equivalent radius would be $r = 3A/2\pi = 0.478A$; and for rectangular sections with face widths A and B, the equivalent radius of the structure would be $r = 2(A+B)/2\pi = 0.318(A+B)$.

III. IEEE/CIGRE FORMULA OF TOWER SURGE IMPEDANCE

A number of tower models have been proposed, but most of them are not general, i.e., a tower model shows a good agreement with a specific case explained in the paper where the model is proposed.

The following IEEE/CIGRE formula of the tower surge impedance is well known and is widely adopted in a lightning surge simulation [25-26] (Fig. 2),

$$Z_t = 60\ \ln\left[\cot\left\{0.5\tan^{-1}\left(\frac{R}{h}\right)\right\}\right]\ \ \Omega, \tag{4}$$

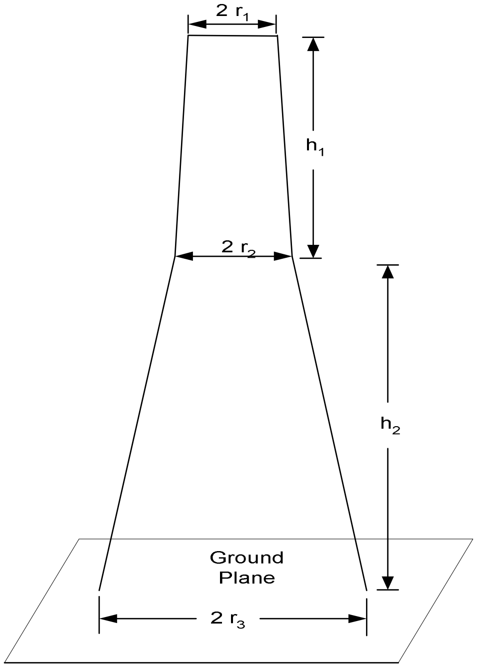

Fig. 2. Tower model proposed by IEEE/CIGRE.

where $R = (r_1h_1 + r_2h + r_3h_2)/h$ is the equivalent radius of the tower represented by a truncated cone, $h = h_1 + h_2$, and

r_1, r_2, r_3 tower top, midsection and base radii [m],

h_1 height from the midsection to top [m],

h_2 height from base to midsection [m].

When the tower is not a cone but a cylinder, then the above equation is rewritten by,

$$Z_t = 60\ \ln\left(\frac{h}{r}\right)\ \ \Omega, \tag{5}$$

where *r* is the radius of a cylinder representing a tower.

IV. JORDAN'S REVISED FORMULA

In [1], Jordan introduced the expression given by equation (3) to represent the surge impedance of a vertical conductor. Although the derivation of equation (3) is not entirely available in [1], one can suppose that Jordan applied the magnetic vector potential to calculate the inductance of a vertical cylinder. The system of Fig. 1(a) was equivalently represented as that in Fig. 1(b), where i is the current in the real conductor, i' is the current in the image conductor, and P_0 is a generic point with coordinates (x_0, y_0) where one wish to calculate magnetic vector potential $\vec{A}$. The parameter a is defined by Jordan [1] as the depth of true ground below the earth's surface, which is assumed to be, as in [5], conceptually equivalent to the complex skin depth p introduced by Deri *et al.* [27] to represent losses due to finite ground conductivity.

According to the method of images, i and i' must have the same direction and sign, as illustrated in Fig. 1(b) [28]. Consequently, $\vec{A}=\vec{A_r}+\vec{A_i}$, where $\vec{A_r}$ is the magnetic vector potential associated with the real conductor, and $\vec{A_i}$ is the magnetic vector potential associated with the image conductor. Nevertheless, in the derivation of equation (3), Jordan considered the opposite sign for the current in the image conductor, and therefore, its contribution to the total magnetic vector potential became subtractive and not additive, as it should be. Consequently, the surge impedance given by equation (3) is underestimated. To evaluate the correct value of surge impedance of a vertical conductor following Jordan's approach, a new expression is then required.

Based on the system of coordinates of Fig. 1(b) and disregarding propagation effects, one can write the total magnetic vector potential at the generic point P_0 as,

$$\vec{A}=\frac{\mu_0 i}{4\pi}\left[\int_a^{a+h}\frac{dy}{\sqrt{(y_0-y)^2+x_0^{\,2}}}+\int_a^{a+h}\frac{dy}{\sqrt{(y_0+y)^2+x_0^{\,2}}}\right]\hat{y} \qquad (6)$$

where the first integral in the right-hand side term corresponds to $\vec{A_r}$, the second integral corresponds to $\vec{A_i}$, and $\hat{y}$ is the unit vector in the y-axis direction. After solving the integrals in equation (6) and knowing that $dL = A\ dy/i$, one can write,

$$dL=\frac{\mu_0}{4\pi}\Big[\ \log_e\frac{\sqrt{(h+a-y_0)^2+x_0^{\,2}}+(h+a-y_0)}{\sqrt{(a-y_0)^2+x_0^{\,2}}+(a-y_0)} +\log_e\frac{\sqrt{(h+a+y_0)^2+x_0^{\,2}}+(h+a+y_0)}{\sqrt{(a+y_0)^2+x_0^{\,2}}+(a+y_0)}\ \Big]\ dy_0, \qquad (7)$$

where dL is the differential inductance element. Note that if $\vec{A}=\vec{A_r}-\vec{A_i}$ is incorrectly assumed, equation (7) becomes equal to the expression obtained by Jordan to represent dL [1].

To calculate the external inductance L per unit length of the vertical conductor, it is necessary to integrate equation (7) in the interval $a \le y_0 \le a+h$, at $x_0 = r$, and then to divide the result by h. To simplify, as in [1], an infinite ground conductivity is now assumed, making $a=0$ in equation (7). As a result,

$$L=\frac{\mu_0}{4\pi}\left\{2\log_e\frac{2h+\sqrt{4h^2+r^2}}{r}+\frac{r}{h}-\frac{\sqrt{4h^2+r^2}}{h}\right\}. \qquad (8)$$

Equation (8) can be further simplified if $h \gg r$. Also if losses are neglected and a transverse electromagnetic (TEM) field structure is assumed, the surge impedance Z_s of the vertical conductor can be obtained by multiplying equation (8) by the speed of light, resulting in,

$$Z_s = 60\ \ln\frac{4h}{r} - 60\ \Omega \qquad (9)$$

which is the same expression obtained by Takahashi [17] but in a slightly different derivation. The theoretical formula of surge impedance with vertical wave incidence derived from Takahashi [17] and validated by Goni *et al.* [29] is,

$$\begin{aligned} Z_s &= 60\left(\ln\sqrt{2}\,\frac{2h}{r}\right) - 92.4\ \Omega \\ &= 60\cdot\left\{\left(\ln\sqrt{2}\,\frac{2h}{r}\right)-1.54\right\}\Omega. \end{aligned} \qquad (10)$$

And with horizontal wave incidence,

$$Z_s = 60\cdot\left\{\left(\ln\sqrt{2}\,\frac{2h}{r}\right)-1.832\right\}\Omega \qquad (11)$$

which is very close to the empirical formula of Hara *et al.* [9],

$$Z_s = 60\cdot\left\{\left(\ln\sqrt{2}\,\frac{2h}{r}\right)-2\right\}\Omega. \qquad (12)$$

Also, equation (9) is similar to the expression independently derived by Wagner and Hileman [2] to calculate the average surge impedance of a vertical cylinder that was later modified by Sargent and Darveniza [3], reaching the final form,

$$Z_{WH} = 60\ \ln\left(\sqrt{2}\,\frac{2h}{r}\right) - 60\ \Omega = 60\ \ln\left(\sqrt{2}\,\frac{ct}{r}\right) - 60\,\Omega\ \cdot$$

In the derivation of Wagner and Hileman [2], a step or rectangular current was assumed to be injected at the top of vertical cylinder, and as a consequence, only the first term in the right-hand side of the above equation was obtained.

V. APPROXIMATION OF LATTICE TOWER

As an alternative to the frequently used cylindrical approximation of a steel tower, a conical representation has also been used. The use of a cone as a simplification of the tower element is not an unrealistic approximation as is shown in Fig. 3, where the cylindrical and conical representations are compared with the actual tower structure. Analyses of the response of these structures were performed using field theory concepts and will be mentioned in the succeeding sections.

VI. ANALYSIS OF THE SURGE RESPONSE OF A CYLINDRICAL TOWER TO A RECTANGULAR WAVE OF CURRENT

If $\boldsymbol{E_i}$ is the electric field due to currents at a point at any instant, and $\boldsymbol{s}$ is the distance along a curve through the point, then,

$$\oint \overline{E}_i \cdot \overline{ds} = -\oint \frac{\partial \overline{A}}{\partial t} \cdot \overline{ds}$$

where $\boldsymbol{A}$ is the vector magnetic potential at the point.

Consider an isolated cylindrical tower of height h and radius r normal to a perfectly conducting horizontal earth plane as shown in Fig. 4. Consider a rectangular wave of current I impressed on the tower at $x = 0$ at time $t = 0$. Then the surface current density is,

$$J_s = \frac{I}{2\pi r} \cdot$$

Consider an element dx of the tower as shown in Fig. 4, then the vector magnetic potential at a point (d, r) is,

$$\overline{A} = \frac{\mu_0}{4\pi} \oint\oint \frac{\overline{J_s(x, \beta, t - r'/c)}}{r'} dS$$

where dS is the element of surface $(dx \cdot r \cdot d\beta)$ and r' is the distance from dS to the point (d, r).
Hence,

$$\overrightarrow{A} = \frac{\mu_0}{4\pi} \int_0^{2\pi} \int_0^{y} \frac{I}{2\pi r} \cdot \frac{r dx \cdot d\beta}{\sqrt{(x-d)^2 + r^2}} \widehat{a}_d \cdot$$

Therefore,

$$\int_{d=0}^{d=p} \vec{E}_i \cdot d\vec{s} = -\frac{\mu_0 I c}{4\pi} \ln \frac{ct}{ct - p} = -I \cdot \left[60 \cdot \ln\left(\sqrt{2} \frac{ct}{r} \right) \right] \cdot$$

Note that the expression in brackets is of the form of a surge impedance, for $ct >> r$. Thus, following Wagner and Hileman, the transient surge impedance,

$$Z = 60 \ln\left(\sqrt{2} \frac{ct}{r} \right) = 60 \ln\left(\sqrt{2} \frac{2h}{r} \right) \cdot \tag{13}$$

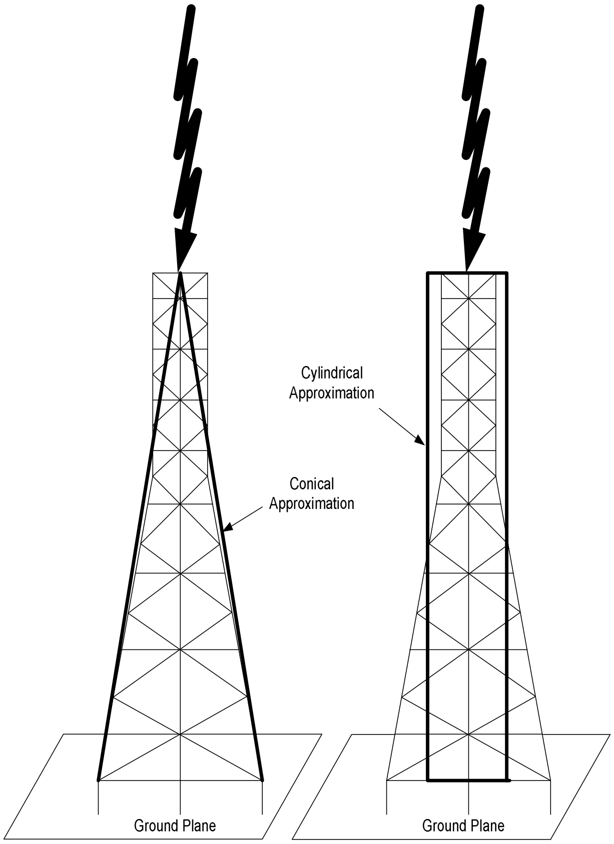

Fig. 3. Comparison of conical and cylindrical approximations of steel lattice communication tower.

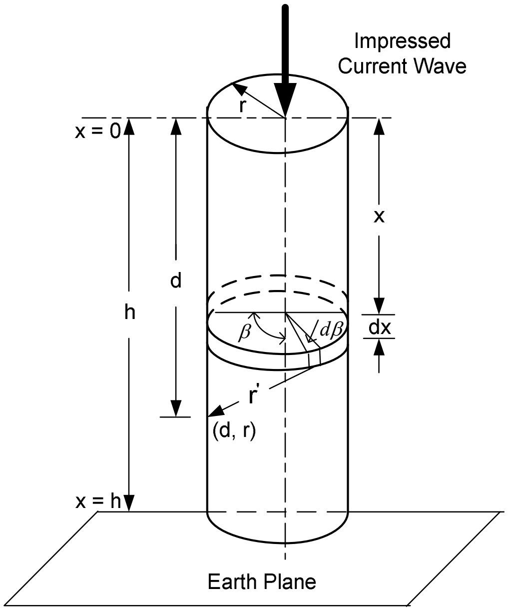

Fig. 4. Cylindrical tower used in field theory analyses.

VII. ANALYSIS OF THE SURGE RESPONSE OF A CYLINDRICAL TOWER TO A RAMP WAVE OF CURRENT, *I = KT*

Consider the cylindrical tower of Fig. 4, with a ramp current wave impressed at x = 0 at time t = 0. Then the time retarded, surface current density is,

$$J_s\left(x,\ t-\frac{r'}{c}\right)=\frac{K}{2\pi r}\left(t-\frac{x}{c}-\frac{r'}{c}\right)\cdot$$

Using the nomenclature defined in Fig. 4 the vector magnetic potential at a point (d, r) is,

$$\vec{A}=\frac{\mu_0}{4\pi}\int_0^{2\pi}\int_0^{y}\frac{K}{2\pi r}\left(t-\frac{x}{c}-\frac{r'}{c}\right)\cdot\frac{r\cdot dx\cdot d\beta}{r'}\,\widehat{a}_d\cdot$$

Integrating the electric field due to currents over the height of the cylinder, and for $ct >> r$

$$\int_0^p \vec{E}_i\cdot d\vec{s}=-Kt\left[60\cdot\left\{\ln\left(\sqrt{2}\,\frac{ct}{r}\right)-1+\frac{r}{2ct}+\left(\frac{r}{2ct}\right)^2\right\}\right]$$

Again the term in brackets is of the form of a surge impedance. Hence the transient surge impedance of a cylindrical tower, derived by Sargent and Darveniza for a ramp current wave impressed, may be defined as,

$$\begin{aligned}Z&=60\ \ln\left(\sqrt{2}\,\frac{ct}{r}\right)-60=60\ \ln\left(\sqrt{2}\,\frac{2h}{r}\right)-60\\&=60\cdot\left\{\ln\left(\sqrt{2}\,\frac{2h}{r}\right)-1\right\}.\end{aligned}\tag{14}$$

VIII. ANALYSIS OF THE SURGE RESPONSE OF A CONICAL TOWER

The conventional double-circuit steel lattice tower can be conveniently approximated by a right cone of appropriate half-angle.

Consider a conical tower of height h and half-angle θ, as shown in Fig. 5. A rectangular wave of current is impressed at the tower top (x = 0) at time t = 0, and consider an element of the tower at x (measured in a vertical direction) from the tower top. It is necessary to determine the vector magnetic potential at a general point (d, r) on the cone.

Consider the contribution $|\delta A|$ to the vector magnetic potential at (d, r) of an element (du, $d\beta$) as shown in Fig. 5. Then,

$$\begin{aligned}|\delta A|&=\frac{\mu_0}{4\pi}\frac{|J[x,t-(r/c)]|}{r'}du\cdot\alpha\cdot d\beta\\&=\frac{\mu_0}{4\pi}\cdot\frac{I}{2\pi}\cdot\frac{du\cdot d\beta}{r'}.\end{aligned}$$

Therefore the vector magnetic potential at (d, r), in the direction of the unit vector $\hat{\boldsymbol{u}}$ is,

$$\overrightarrow{A_u}=\frac{\mu_0}{4\pi}\cdot\frac{I}{2\pi}\int_0^{2\pi}\int_0^{y}\cdot\frac{K\cdot b\cdot du\cdot d\beta}{\sqrt{x^2+d^2-2b\cdot d\cdot x}}\,\widehat{u}\ .$$

Hence, $\dfrac{\partial\overrightarrow{A_u}}{\partial t}=-\vec{E}_{iu}=\dfrac{\mu_0}{4\pi}\cdot\dfrac{I}{2\pi}\displaystyle\int_0^{2\pi}\frac{Kcb}{Kct-bd}d\beta\,.$

Therefore

$$\begin{aligned}\int_{u=0}^{u=ct}\vec{E}_{iu}\cdot du&=-\frac{\mu_0}{4\pi}\cdot\frac{I}{2\pi}\int_0^{2\pi}\int_0^{ct}\frac{cb}{ct-bu}\,du\cdot d\beta\\&=-\frac{30\,I}{2\pi}\int_0^{2\pi}\ln\left(\frac{1}{[2S^2\sin^2(\beta/2)]}\right)d\beta\\&=-I\cdot\{60\cdot\ln(\sqrt{2}/S)\}.\end{aligned}$$

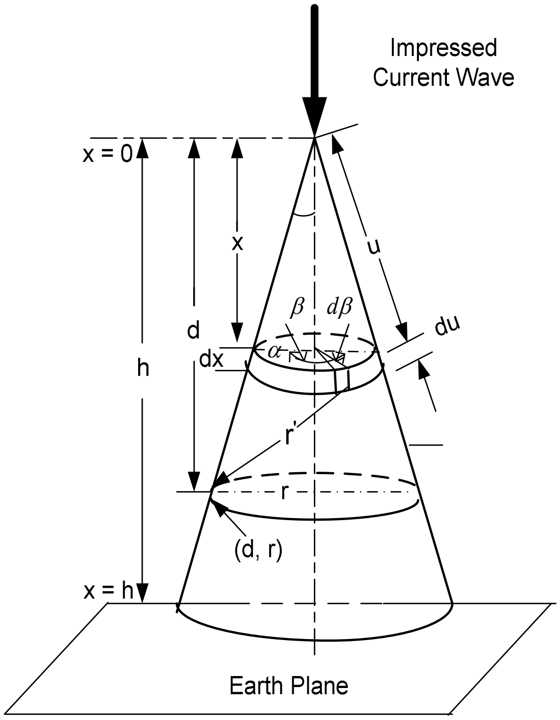

Fig. 5. Conical tower used in field theory analyses.

The expression in above braces is of the form of a surge impedance. Hence the transient surge impedance of a cone is defined as,

$$Z=60\ \ln\left(\sqrt{2}/S\right).\tag{15}$$

where $\boldsymbol{S}$ is the sine of the half-angle of the cone. This equation provides realistic estimates of the surge impedance of a steel lattice tower because it is in excellent agreement, both in magnitude and time-invariance characteristics, with values measured experimentally using geometric model technique [3].

IX. CONCLUSION

Different equations to calculate the surge impedance of vertical conductors including lattice tower are analyzed starting with Jordan's original formula. The performed analyses indicate that Jordan's revised formula is more than adequate to simulate electromagnetic transients in vertical conductors than the Jordan's original formula. Furthermore, the value of surge impedance depends on the shape of triggered lightning current pulse. The validity of the Jordan's equation has been tested by the well-known recent experimental and other analytical results mentioned in Table 1.

The investigation reported here several ways to evaluate and compare the surge impedance of complex structure which is of greater interests for practical applications and future developments for insulation coordination and protection system designing.

Table 1. Comparison of analytical values of surge impedance of steel lattice communication tower.

Source	**Technique or Equation**	**Tower Representation**	**Current Waveshape**	**Surge Impedance**
Jordan	equation (3)	cylinder	any	125
IEEE/CIGRE	equation (5)	cylinder	ramp	179
Revised Jordan's Formula	equation (9)	cylinder	step	201
Takahashi	equation (10)	cylinder	step(vertical injection)	148
Takahashi	equation (11)	cylinder	Step (horizontal injection)	122
Hara et al.	equation (12)	cylinder	Step(horizontal injection)	121
Wagner and Hileman	equation (13)	cylinder	Step	240
Sargent and Darveniza	equation (14)	cylinder	ramp and double exponential	180
Sargent and Darveniza	equation (15)	cone	any	130—150

REFERENCES

[1] C. A. Jordan "Lightning computations for transmission lines with overhead ground wires, Part II," *Gen. Electr. Rev*, vol,37,no pp.180-186,1934.

[2] C. F. Wagner and A. R. Hileman, "A new approach to the calculation of the lightning performance of transmission line III-A simplified method: Stroke to tower, ''*AIEEE Trans.* Part III*,* vol. 79, pp. 589-603, Oct. 1990.

[3] M. A. Sargent and M. Darveniza, "Tower surge impedance" *IEEE Trans. Power App. Syst.*, vol. PAS-88, no. 5, pp. 680-687, May 1969.

[4] W. A. Chisolm, Y. L. Chow, and K. D. Srivastava, "Lightning surge response of transmission towers," *IEEE Trans. Power App. Syst.*, vol. PAS- 102, no. 9, pp. 3232–3242, Sep. 1983.

[5] A. Ametani, Y. Kasai, J. Sawada, A. Mochizuki, and T. Yamada, "Frequency-dependent impedance of vertical conductors and a multiconductor tower model," in *Proc.Inst. Elect. Eng. Gener. Transmiss. Distrib.*, vol. 141, no. 4, pp. 339–345, Jul. 1994.

[6] J. A. Gutierrez, R. P. Moreno, J. L. Naredo, J. L. Bermudez, M. Paolone, C. A. Nucci, and F. Rachidi, "Nonuniform transmission tower model for lightning transient studies," *IEEE Trans.Power Del.*, vol. 19, no. 2, pp. 490–496, Apr. 2004.

[7] M. Ishii and Y. Baba, "Numerical electromagnetic field analysis of tower surge response," *IEEE Trans. Power Del.*, vol. 12, no. 1, pp. 483-488, Jan. 1997.

[8] T. Noda and S. Yokoyama, "Thin wire representation in finite time domain surge simulation," *IEEE Trans. Power Del.*, vol. 17, no. 3, pp. 840-847, Jul. 2002.

[9] T. Hara, O. Yamamoto, M. Hayashi, and C. Uenosono, "Empirical formulas of surge impedance for single and multiple vertical cylinder," *Trans. Inst. Elect. Eng. Jpn.*, vol. 110-B, no. 2, pp. 129–137, 1990 (in Japanese).

[10] T. Hara and O. Yamamoto, "Modelling of a transmission tower for lightning surge analysis," *Proc. Inst. Elect. Eng. Gener. Transmiss. Distrib.*, vol. 143, no. 3, pp. 283–289, May 1996.

[11] M. Ishii, T. Kawamura, T. Kouno, E. Ohsaki, K. Shiokawa, K. Murotani, and T. Higuchi, "Multistory transmission tower model for lightning surge analysis," *IEEE Trans. Power Del.*, vol. 6, no. 3, pp. 1327-1335, Jul.1993.

[12] T. Yamada, A. Mochizuki, J. Sawada, T. Kawamura, A. Ametani, M. Ishii, and S. Kato, "Experimental evaluation of a UHV tower model for lightning surge analysis," *IEEE Trans. Power Del.*, vol. 10, no. 1, pp. 393-402, Jan. 1995.

[13] J. L. Bermudez, F. Rachidi, W. A. Chisholm, M. Rubinstein, W. Janischewskyj, A. M. Hussein, V. Shostak, and J. S. Chang, "On the use of transmission line theory to represent a nonuniform vertically-extended object struck by lightning," presented at the *IEEE Int. Symp. EMC*, Boston, MA, Aug. 2003.

[14] H. Motoyama and H. Matsubara, "Analytical and experimental study on surge response of transmission tower," *IEEE Trans. Power Del.*, vol. 15, no. 2, pp. 812–819, Apr. 2000.

[15] Y. Baba and M. Ishii, "Numerical electromagnetic field analysis on lightning surge response of tower with shield wire," *IEEE Trans. Power Del.*, vol. 15, no. 3, pp. 1010–1015, Jul. 2000.

[16] A. Soares, Jr. and S. Visacro, "Simplified expressions for tower surge impedance based on application of a field-circuit modeling approach," in *Proc. 27th ICLP*, Avignon, France, pp. 487-491, 2004.

[17] H. Takahashi, "Confirmation of the error of Jordan's formula on tower surge impedance," *Trans. Inst. Elect. Eng. Jpn.*, vol. 114-B, pp. 112-113, 1994 (in Japanese).

[18] V. A. Rakov, "Transient response of a tall object to lightning," *IEEE Trans. Electromagn. Compat.*, vol. 43, no. 4, pp. 654-661, Nov. 2001.

[19] F. Rachidi, V. A. Rakov, C. A. Nucci, and J. L. Bermudez, "Effect of vertically extended strike object on the distribution of current along the lightning channel," *J. Geophys. Res.*, vol. 107, no. D23, pp. 16-1--16-6, 2002.

[20] D. Pavanello, F. Rachidi, M. Rubinstein, J. L. Bermudez, and C. A. Nucci, "Electromagnetic field radiated by lightning to tall towers: Treatment of the discontinuity at the return-stroke wave front," *J. Geophys. Res.*, vol. 109, no. D6, D06114, 2004.

[21] L. Grcev and F. Rachidi, "On tower impedances for transient analysis," *IEEE Trans. Power Del.*, vol. 19, no. 3, pp. 1238–1244, Jul. 2005.

[22] Y. Baba and V. A. Rakov, "On the mechanism of attenuation of current waves propagating along a vertical perfectly conducting wire above ground: Application to lightning," *IEEE Trans. Electromagn. Compat.*, vol. 47, no. 3, pp. 521–532, Aug. 2005.

[23] Y. Baba and V. A. Rakov, "On the interpretation of ground reflections observed in small scale experiments simulating lightning strikes to towers," *IEEE Trans. Electromagn. Compat.*, vol. 47, no. 3, pp. 533–542, Aug. 2005.

[24] S. Visacro and F. H. Silveira, "Lightning current waves measured at short instrumented towers: The influence of sensor position," *Geophys. Res. Lett.*, vol. 32, no. 18, L18804, Sep. 2005.

[25] S. Visacro and F. H. Silveira, "Estimating lightning performance of transmission lines, II—update to analytical models," *IEEE Trans. Power Del.*, vol. 8, pp. 1254, 1993.

[26] S. Visacro and F. H. Silveira, "Guide to procedures for estimating lightning performance of transmission lines," CIGRE SC33-WG01, Tech. Brochure, Oct. 1991.

[27] A. Deri, G. Tevan, A. Semlyen, and A. Castanheira, "The complex ground return plane:Asimplified model for homogeneous andmulti-layer return," *IEEE Trans. Power App. Syst.*, vol. PAS-100, no. 8, pp. 3686–3693, Aug. 1981.

[28] E. C. Jordan and K. G. Balmain, *Electromagnetic Waves and Radiating Systems*, 2nd ed. Englewood Cliffs, NJ: Prentice-Hall, 1968.

[29] M. O. Goni, M. F. Hossain, M. M. Rahman, M. S.Yusuf, E. Kaneko, and H. Takahashi, " Simulation and experimental analyses of electromagnetic transient behaviors of lightning surge on vertical conductors," *IEEE Trans. on Power Delivery*, Vol. 21, No. 4, October 2006.

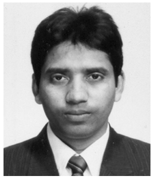

Md. Osman Goni was born in Bangladesh in February 1971. He received the B.S. degree in electrical and electronic engineering from the Bangladesh Institute of Technology, Khulna, Bangladesh, in 1993, and the M.S. and D.Eng. degrees from the University of the Ryukyus, Okinawa, Japan, in 2001 and 2004, respectively. Currently, he is an Associate Professor and Head of the Department of Electronics and Communication Engineering, Khulna University of Engineering and Technology. He has been engaged in teaching and research in digital signal and image processing, electric power and energy system engineering, electromagnetic energy engineering, electromagnetic theory, the FDTD method, MoM, NEC-2, lightning surge analysis, vertical conductor problems, and EMTP. Dr. Goni is a member of IEEE, the Institute of Electrical Engineering(IEE) of Japan, and IEB.

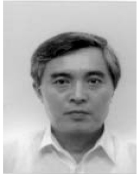

Akihiro Ametani was born on February 14, 1944. He received Ph.D. degree from UMIST, Manchester in 1973. He was with the UMIST from 1971 to 1974 and Bonneville Power Administration for summers from 1976 to 1981. He has been a professor at Doshisha University since 1985 and was a professor at the Chatholic University of Leaven, Belgium in 1988. He was the Director of the Institute of Science and Engineering and Dean of Library and computer/Information Center in Doshisha University from 1996 to 2001. Dr. Ametani is a Chartered Engineer in U.K., a Distinguished member of CIGRE, a Fellow of IEE and IEEE. He has been a Vice President of the IEE of Japan since 2004.

2009 INSTITUTIONAL MEMBERS

AUSTRALIAN DEFENCE LIBRARY
Northcott Drive
Canberra, A.C.T. 2600 Australia

BAE SYSTEMS
W423A Warton Aerodome
Preston, Lancashire
United Kingdom PR4 1AX

DARTMOUTH COLLEGE
6193 Murdough Center
Hanover, NH 03755-3560

DSTO-DSTORL EDINBURGH
Jets AU/33851-99, PO Box 562
Milsons Point, NSW
Australia 1565

DTIC-OCP/LIBRARY
8725 John J. Kingman Rd. Ste 0944
Ft. Belvoir, VA 22060-6218

ELSEVIER
Bibliographic Databases
PO Box 2227
Amsterdam, Netherlands 1000 CE

ENGINEERING INFORMATION, INC
PO Box 543
Amsterdam, Netherlands 1000 Am

ETSE TELECOMUNICACION
Biblioteca, Campus Lagoas
Vigo, 36200 Spain

FLORIDA INTERNATIONAL UNIV
10555 W. Flagler Street
Miami, FL 33174

GEORGIA TECH LIBRARY
225 North Avenue, NW
Atlanta, GA 30332-0001

HANYANG UNIVERSITY
Paiknam Academic Info. Ctr Library
17 Haengdang-Dong
Seongdong-Ku
Seoul, South Korea 133-791

HRL LABS, RESEARCH LIBRARY
3011 Malibu Canyon
Malibu, CA 90265

IEE INSPEC/Acquisitions Section
Michael Faraday House
6 Hills Way
Stevenage, Herts UK SG1 2AY

IND CANTABRIA
PO Box 830470
Birmingham, AL 35283

INSTITUTE FOR SCIENTIFIC INFO.
Publication Processing Dept.
3501 Market St.
Philadelphia, PA 19104-3302

LIBRARY – DRDC OTTAWA
3701 Carling Avenue
Ottawa, Ontario, Canada K1A OZ4

LIBRARY of CONGRESS
Reg. Of Copyrights
Attn: 40T Deposits
Washington DC, 20559

LINDA HALL LIBRARY
5109 Cherry Street
Kansas City, MO 64110-2498

LULEA UNIV. OF TECHNOLOGY
Porson
Lulea, Sweden 97187

MISSISSIPPI STATE UNIV LIBRARY
PO Box 9570
Mississippi State, MS 39762

MISSOURI S&T
400 W 14th Street
Rolla, MO 56409

MIT LINCOLN LABORATORY
Periodicals Library
244 Wood Street
Lexington, MA 02420

NATIONAL DEFENSE ACADEMY
1-10-20 Hashirimizu
Yokosuka, Kanagawa
239-8686 Japan

NAVAL POSTGRADUATE SCHOOL
Attn:J. Rozdal/411 Dyer Rd./ Rm 111
Monterey, CA 93943-5101

NDL KAGAKU
C/0 KWE-ACCESS
PO Box 300613 (JFK A/P)
Jamaica, NY 11430-0613

OHIO STATE UNIVERSITY
1320 Kinnear Road
Columbus, OH 43212

OVIEDO LIBRARY
PO BOX 830679
Birmingham, AL 35283

PENN STATE UNIVERSITY
126 Paterno Library
University Park, PA 16802-1808

DAVID J. PINION
1122 E PIKE STREET #1217
SEATTLE, WA 98122

SOUTHWEST RESEARCH
INSTITUTE
6220 Culebra Road
San Antonio, TX 78238

SWETS INFORMATION SERVICES
160 Ninth Avenue, Suite A
Runnemede, NJ 08078

TELSTRA
13/242 Exhibition Street
Melbourne, Victoria
3000 Australia

TIB & UNIV. BIB. HANNOVER
DE/5100/G1/0001
Welfengarten 1B
Hannover, Germany 30167

TU DARMSTADT
Schlossgartenstrasse 8
Darmstadt, Hessen
Germany D-64289

UNIV OF CENTRAL FLORIDA LIB.
4000 Central Florida Boulevard
Orlando, FL 32816-8005

UNIVERSITY OF KANSAS –
WATSON
1425 Jayhawk Blvd 210S
Lawrence, KS 66045-7594

UNIVERSITY OF MISSISSIPPI
JD Williams Library
University, MS 38677-1848

UNIVERSITY OF PALERMO
PO Box 69- Poste S. Silvestr
Rome, 00187, Italy

VIRTUAL EM INC.
2019 Georgetown Blvd.
Ann Arbor, MI 48105

ACES COPYRIGHT FORM

This form is intended for original, previously unpublished manuscripts submitted to ACES periodicals and conference publications. The signed form, appropriately completed, MUST ACCOMPANY any paper in order to be published by ACES. PLEASE READ REVERSE SIDE OF THIS FORM FOR FURTHER DETAILS.

TITLE OF PAPER:

AUTHORS(S)
PUBLICATION TITLE/DATE:

RETURN FORM TO:
Dr. Atef Z. Elsherbeni
University of Mississippi
Dept. of Electrical Engineering
Anderson Hall Box 13
University, MS 38677 USA

PART A - COPYRIGHT TRANSFER FORM

(NOTE: Company or other forms may not be substituted for this form. U.S. Government employees whose work is not subject to copyright may so certify by signing Part B below. Authors whose work is subject to Crown Copyright may sign Part C overleaf).

The undersigned, desiring to publish the above paper in a publication of ACES, hereby transfer their copyrights in the above paper to The Applied Computational Electromagnetics Society (ACES). The undersigned hereby represents and warrants that the paper is original and that he/she is the author of the paper or otherwise has the power and authority to make and execute this assignment.

Returned Rights: In return for these rights, ACES hereby grants to the above authors, and the employers for whom the work was performed, royalty-free permission to:

1. Retain all proprietary rights other than copyright, such as patent rights.
2. Reuse all or portions of the above paper in other works.
3. Reproduce, or have reproduced, the above paper for the author's personal use or for internal company use provided that (a) the source and ACES copyright are indicated, (b) the copies are not used in a way that implies ACES endorsement of a product or service of an employer, and (c) the copies per se are not offered for sale.
4. Make limited distribution of all or portions of the above paper prior to publication.
5. In the case of work performed under U.S. Government contract, ACES grants the U.S. Government royalty-free permission to reproduce all or portions of the above paper, and to authorize others to do so, for U.S. Government purposes only.

ACES Obligations: In exercising its rights under copyright, ACES will make all reasonable efforts to act in the interests of the authors and employers as well as in its own interest. In particular, ACES REQUIRES that:

1. The consent of the first-named author be sought as a condition in granting re-publication permission to others.
2. The consent of the undersigned employer be obtained as a condition in granting permission to others to reuse all or portions of the paper for promotion or marketing purposes.

In the event the above paper is not accepted and published by ACES or is withdrawn by the author(s) before acceptance by ACES, this agreement becomes null and void.

AUTHORIZED SIGNATURE — TITLE (IF NOT AUTHOR)

EMPLOYER FOR WHOM WORK WAS PERFORMED — DATE FORM SIGNED

Part B - U.S. GOVERNMENT EMPLOYEE CERTIFICATION

(NOTE: if your work was performed under Government contract but you are not a Government employee, sign transfer form above and see item 5 under Returned Rights).

This certifies that all authors of the above paper are employees of the U.S. Government and performed this work as part of their employment and that the paper is therefor not subject to U.S. copyright protection.

AUTHORIZED SIGNATURE — TITLE (IF NOT AUTHOR)

NAME OF GOVERNMENT ORGANIZATION — DATE FORM SIGNED

PART C - CROWN COPYRIGHT

(NOTE: ACES recognizes and will honor Crown Copyright as it does U.S. Copyright. It is understood that, in asserting Crown Copyright, ACES in no way diminishes its rights as publisher. Sign only if *ALL* authors are subject to Crown Copyright).

This certifies that all authors of the above Paper are subject to Crown Copyright. (Appropriate documentation and instructions regarding form of Crown Copyright notice may be attached).

AUTHORIZED SIGNATURE TITLE OF SIGNEE

NAME OF GOVERNMENT BRANCH DATE FORM SIGNED

Information to Authors

ACES POLICY

ACES distributes its technical publications throughout the world, and it may be necessary to translate and abstract its publications, and articles contained therein, for inclusion in various compendiums and similar publications, etc. When an article is submitted for publication by ACES, acceptance of the article implies that ACES has the rights to do all of the things it normally does with such an article.

In connection with its publishing activities, it is the policy of ACES to own the copyrights in its technical publications, and to the contributions contained therein, in order to protect the interests of ACES, its authors and their employers, and at the same time to facilitate the appropriate re-use of this material by others.

The new United States copyright law requires that the transfer of copyrights in each contribution from the author to ACES be confirmed in writing. It is therefore necessary that you execute either Part A-Copyright Transfer Form or Part B-U.S. Government Employee Certification or Part C-Crown Copyright on this sheet and return it to the Managing Editor (or person who supplied this sheet) as promptly as possible.

CLEARANCE OF PAPERS

ACES must of necessity assume that materials presented at its meetings or submitted to its publications is properly available for general dissemination to the audiences these activities are organized to serve. It is the responsibility of the authors, not ACES, to determine whether disclosure of their material requires the prior consent of other parties and if so, to obtain it. Furthermore, ACES must assume that, if an author uses within his/her article previously published and/or copyrighted material that permission has been obtained for such use and that any required credit lines, copyright notices, etc. are duly noted.

AUTHOR/COMPANY RIGHTS

If you are employed and you prepared your paper as a part of your job, the rights to your paper initially rest with your employer. In that case, when you sign the copyright form, we assume you are authorized to do so by your employer and that your employer has consented to all of the terms and conditions of this form. If not, it should be signed by someone so authorized.

NOTE RE RETURNED RIGHTS: Just as ACES now requires a signed copyright transfer form in order to do “business as usual”, it is the intent of this form to return rights to the author and employer so that they too may do “business as usual”. If further clarification is required, please contact: The Managing Editor, R. W. Adler, Naval Postgraduate School, Code EC/AB, Monterey, CA, 93943, USA (408)656-2352.

Please note that, although authors are permitted to re-use all or portions of their ACES copyrighted material in other works, this does not include granting third party requests for reprinting, republishing, or other types of re-use.

JOINT AUTHORSHIP

For jointly authored papers, only one signature is required, but we assume all authors have been advised and have consented to the terms of this form.

U.S. GOVERNMENT EMPLOYEES

Authors who are U.S. Government employees are not required to sign the Copyright Transfer Form (Part A), but any co-authors outside the Government are.

Part B of the form is to be used instead of Part A only if all authors are U.S. Government employees and prepared the paper as part of their job.

NOTE RE GOVERNMENT CONTRACT WORK: Authors whose work was performed under a U.S. Government contract but who are not Government employees are required so sign Part A-Copyright Transfer Form. However, item 5 of the form returns reproduction rights to the U. S. Government when required, even though ACES copyright policy is in effect with respect to the reuse of material by the general public.

APPLIED COMPUTATIONAL ELECTROMAGNETICS SOCIETY JOURNAL
http://aces.ee.olemiss.edu

INFORMATION FOR AUTHORS

PUBLICATION CRITERIA

Each paper is required to manifest some relation to applied computational electromagnetics. **Papers may address general issues in applied computational electromagnetics, or they may focus on specific applications, techniques, codes, or computational issues.** While the following list is not exhaustive, each paper will generally relate to at least one of these areas:

1. **Code validation.** This is done using internal checks or experimental, analytical or other computational data. Measured data of potential utility to code validation efforts will also be considered for publication.

2. **Code performance analysis.** This usually involves identification of numerical accuracy or other limitations, solution convergence, numerical and physical modeling error, and parameter tradeoffs. However, it is also permissible to address issues such as ease-of-use, set-up time, run time, special outputs, or other special features.

3. **Computational studies of basic physics.** This involves using a code, algorithm, or computational technique to simulate reality in such a way that better, or new physical insight or understanding, is achieved.

4. **New computational techniques** or new applications for existing computational techniques or codes.

5. **"Tricks of the trade"** in selecting and applying codes and techniques.

6. **New codes, algorithms, code enhancement, and code fixes.** This category is self-explanatory, but includes significant changes to existing codes, such as applicability extensions, algorithm optimization, problem correction, limitation removal, or other performance improvement. **Note: Code (or algorithm) capability descriptions are not acceptable, unless they contain sufficient technical material to justify consideration.**

7. **Code input/output issues.** This normally involves innovations in input (such as input geometry standardization, automatic mesh generation, or computer-aided design) or in output (whether it be tabular, graphical, statistical, Fourier-transformed, or otherwise signal-processed). Material dealing with input/output database management, output interpretation, or other input/output issues will also be considered for publication.

8. **Computer hardware issues.** This is the category for analysis of hardware capabilities and limitations of various types of electromagnetics computational requirements. Vector and parallel computational techniques and implementation are of particular interest.

Applications of interest include, but are not limited to, antennas (and their electromagnetic environments), networks, static fields, radar cross section, inverse scattering, shielding, radiation hazards, biological effects, biomedical applications, electromagnetic pulse (EMP), electromagnetic interference (EMI), electromagnetic compatibility (EMC), power transmission, charge transport, dielectric, magnetic and nonlinear materials, microwave components, MEMS, RFID, and MMIC technologies, remote sensing and geometrical and physical optics, radar and communications systems, sensors, fiber optics, plasmas, particle accelerators, generators and motors, electromagnetic wave propagation, non-destructive evaluation, eddy currents, and inverse scattering.

Techniques of interest include but not limited to frequency-domain and time-domain techniques, integral equation and differential equation techniques, diffraction theories, physical and geometrical optics, method of moments, finite differences and finite element techniques, transmission line method, modal expansions, perturbation methods, and hybrid methods.

Where possible and appropriate, authors are required to provide statements of quantitative accuracy for measured and/or computed data. This issue is discussed in "Accuracy & Publication: Requiring, quantitative accuracy statements to accompany data," by E. K. Miller, *ACES Newsletter,* Vol. 9, No. 3, pp. 23-29, 1994, ISBN 1056-9170.

SUBMITTAL PROCEDURE

All submissions should be uploaded to ACES server through ACES web site (http://aces.ee.olemiss.edu) by using the upload button, journal section. Only pdf files are accepted for submission. The file size should not be larger than 5MB, otherwise permission from the Editor-in-Chief should be obtained first. Automated acknowledgment of the electronic submission, after the upload process is successfully completed, will be sent to the corresponding author only. It is the responsibility of the corresponding author to keep the remaining authors, if applicable, informed. Email submission is not accepted and will not be processed.

PAPER FORMAT (INITIAL SUBMISSION)

The preferred format for initial submission manuscripts is 12 point Times Roman font, single line spacing and single column format, with 1 inch for top, bottom, left, and right margins. Manuscripts should be prepared for standard 8.5x11 inch paper.

EDITORIAL REVIEW

In order to ensure an appropriate level of quality control, papers are peer reviewed. They are reviewed both for technical correctness and for adherence to the listed guidelines regarding information content and format.

PAPER FORMAT (FINAL SUBMISSION)

Only camera-ready electronic files are accepted for publication. The term **"camera-ready" means that the material is neat, legible, reproducible, and in accordance with the final version format listed below.**

The following requirements are in effect for the final version of an ACES Journal paper:

1. The paper title should not be placed on a separate page. The title, author(s), abstract, and (space permitting) beginning of the paper itself should all be on the first page. The title, author(s), and author affiliations should be centered (center-justified) on the first page. The title should be of font size 16 and bolded, the author names should be of font size 12 and bolded, and the author affiliation should be of font size 12 (regular font, neither italic nor bolded).

2. An abstract is required. The abstract should be a brief summary of the work described in the paper. It should state the computer codes, computational techniques, and applications discussed in the paper (as applicable) and should otherwise be usable by technical abstracting and indexing services. The word "Abstract" has to be placed at the left margin of the paper, and should be bolded and italic. It also should be followed by a hyphen (—) with the main text of the abstract starting on the same line.

3. All section titles have to be centered and all the title letters should be written in caps. The section titles need to be numbered using roman numbering (I. II. ….)

4. Either British English or American English spellings may be used, provided that each word is spelled consistently throughout the paper.

5. Internal consistency of references format should be maintained. As a guideline for authors, we recommend that references be given using numerical numbering in the body of the paper (with numerical listing of all references at the end of the paper). The first letter of the authors' first name should be listed followed by a period, which in turn, followed by the authors' complete last name. Use a coma (,) to separate between the authors' names. Titles of papers or articles should be in quotation marks (" "), followed by the title of journal, which should be in italic font. The journal volume (vol.), issue number (no.), page numbering (pp.), month and year of publication should come after the journal title in the sequence listed here.

6. Internal consistency shall also be maintained for other elements of style, such as equation numbering. As a guideline for authors who have no other preference, we suggest that equation numbers be placed in parentheses at the right column margin.

7. The intent and meaning of all text must be clear. For authors who are not masters of the English language, the ACES Editorial Staff will provide assistance with grammar (subject to clarity of intent and meaning). However, this may delay the scheduled publication date.

8. Unused space should be minimized. Sections and subsections should not normally begin on a new page.

ACES reserves the right to edit any uploaded material, however, this is not generally done. It is the author(s) responsibility to provide acceptable camera-ready pdf files. Incompatible or incomplete pdf files will not be processed for publication, and authors will be requested to re-upload a revised acceptable version.

COPYRIGHTS AND RELEASES

Each primary author must sign a copyright form and obtain a release from his/her organization vesting the copyright with ACES. Copyright forms are available at ACES, web site (http://aces.ee.olemiss.edu). To shorten the review process time, the executed copyright form should be forwarded to the Editor-in-Chief immediately after the completion of the upload (electronic submission) process. Both the author and his/her organization are allowed to use the copyrighted material freely for their own private purposes.

Permission is granted to quote short passages and reproduce figures and tables from and ACES Journal issue provided the source is cited. Copies of ACES Journal articles may be made in accordance with usage permitted by Sections 107 or 108 of the U.S. Copyright Law. This consent does not extend to other kinds of copying, such as for general distribution, for advertising or promotional purposes, for creating new collective works, or for resale. The reproduction of multiple copies and the use of articles or extracts for commercial purposes require the consent of the author and specific permission from ACES. Institutional members are allowed to copy any ACES Journal issue for their internal distribution only.

PUBLICATION CHARGES

All authors are allowed for 8 printed pages per paper without charge. Mandatory page charges of $75 a page apply to all pages in excess of 8 printed pages. Authors are entitled to one, free of charge, copy of the journal issue in which their paper was published. Additional reprints are available for a nominal fee by submitting a request to the managing editor or ACES Secretary.

Authors are subject to fill out a one page over-page charge form and submit it online along with the copyright form before publication of their manuscript.

ACES Journal is abstracted in INSPEC, in Engineering Index, DTIC, Science Citation Index Expanded, the Research Alert, and to Current Contents/Engineering, Computing & Technology.